

Binary neutron-star mergers: a review of Einstein's richest laboratory

Luca Baiotti

Graduate School of Science, Osaka University, Toyonaka, 560-0043, Japan

Luciano Rezzolla

*Institute for Theoretical Physics, Max-von-Laue-Str. 1, 60438 Frankfurt, Germany and
Frankfurt Institute for Advanced Studies, Ruth-Moufang-Str. 1, 60438 Frankfurt, Germany*

The merger of binary neutron-stars systems combines in a single process: extreme gravity, copious emission of gravitational waves, complex microphysics, and electromagnetic processes that can lead to astrophysical signatures observable at the largest redshifts. We review here the recent progress in understanding what could be considered Einstein's richest laboratory, highlighting in particular the numerous significant advances of the last decade. Although special attention is paid to the status of models, techniques, and results for fully general-relativistic dynamical simulations, a review is also offered on initial data and advanced simulations with approximate treatments of gravity. Finally, we review the considerable amount of work carried out on the post-merger phase, including: black-hole formation, torus accretion onto the merged compact object, connection with gamma-ray burst engines, ejected material, and its nucleosynthesis.

CONTENTS

I. Introduction	3
II. Broadbrush Picture	7
III. Mathematical Setup	10
A. Spacetime evolution: BSSNOK formulation	10
B. Spacetime evolution: CCZ4 and Z4c formulations	12
C. Spacetime evolution: generalized harmonic formulation	13
D. Spacetime evolution: conformally flat approximation	14
E. Matter evolution: relativistic hydrodynamics	14
F. Matter evolution: relativistic magnetohydrodynamics	15
IV. Initial data	18
A. Irrotational binaries	18
B. Spinning binaries	20
V. Pure-hydrodynamic simulations	23
A. Inspiral and merger dynamics	26
B. Post-merger dynamics	30
1. Influence of the equation of state	32
2. Spectral properties of the gravitational-wave signal	33
3. Black-hole–torus system	41
4. Spectral properties and the mass-redshift degeneracy	41
C. Unequal-mass binaries	44
D. Dynamically captured binaries	45
VI. Beyond pure hydrodynamic simulations	49
A. Ideal and resistive magnetohydrodynamics simulations	49
1. Inspiral and merger dynamics	51
2. Post-merger dynamics: short-lived merger product and black-hole–torus system	55
3. Post-merger dynamics: long-lived merger product and extended X-ray emission	59
B. Inclusion of radiative losses	63
C. Non-bulk dynamics: ejecta, nucleosynthesis and afterglows	66
1. Ejected matter and nucleosynthesis	67
2. Macronovae and other afterglows	71
VII. Advanced Techniques and Alternative Scenarios	76
A. The zoology of binary neutron-star codes	76
B. High-order numerical methods	77
C. Advanced Numerical Techniques	79
D. Alternative theories of gravity	81
E. Relativistic collisions	84
VIII. Summary and outlook	87
Acknowledgements	89
References	90

I. INTRODUCTION

Neutron stars are believed to be born in supernova explosions triggered by the collapse of the iron core in massive stars. Many astronomical observations have revealed that binary neutron stars¹ (BNSs) indeed exist [1] and the most important physical properties of all known such systems are collected in Table I. Despite this observational evidence of existence, the formation mechanisms of BNS systems are not known in detail. The general picture is that in a binary system made of two massive main-sequence stars of masses between approximately 8 and 25 M_{\odot} , the more massive one undergoes a supernova explosion and becomes a neutron star. This is followed by a very uncertain phase in which the neutron star and the main-sequence star evolve in a “common envelope”, that is, with the neutron star orbiting in the extended outer layers of the secondary star [2–4]. At the end of this stage, also the second main-sequence star undergoes a supernova explosion and, if the stars are still bound after the explosions, a BNS system is formed. The common-envelope phase, though brief, is crucial because in that phase the distance between the stars becomes much smaller as a result of drag, and this allows the birth of BNS systems that are compact enough to merge within a Hubble time, following the dissipation of their angular momentum through the emission of gravitational radiation. It is also possible that during the common-envelope phase the neutron star collapses to a black hole, thus preventing the formation of a BNS. Another possible channel for the formation of BNS systems may be the interaction of two isolated neutron stars in dense stellar regions, such as globular clusters, in a process called “dynamical capture” [5–7]. Dynamically formed binary systems are different from the others because they have higher ellipticities (see Sect. VD). It is presently not known what fraction of BNS systems would originate from dynamical capture, but it is expected that these binaries are only a small part of the whole population.

This is undoubtedly an exciting and dynamical time for research on BNS mergers, when many accomplishments have been achieved (especially since 2008), while many more need to be achieved in order to describe such fascinating objects and the related physical phenomena. The first direct detection through the advanced interferometric LIGO detectors [22] of the gravitational-wave signal from what has been interpreted as the inspiral, merger and ringdown of a binary system of black holes [23] marks, in many respects, the beginning of gravitational-wave astronomy; a second detection was made a few months later [24]. Additional advanced detectors, such as Virgo [25], KAGRA [26] and LIGO India (see e.g., [27]), are going to become operational in the next few years, and we are likely to witness soon also signals from the inspiral and post-merger of neutron-star binaries or neutron-star–black-hole binaries, with a detection rate that has an uncertainty of three orders of magnitude, but is expected to be of several events per year [28].

BNS mergers are rather unique objects in the landscape of relativistic astrophysics as they are expected to be at the origin of several and diverse physical processes, namely: (i) to be significant sources of gravitational radiation, not only during the inspiral, but also during and after the merger; (ii) to be possible progenitors for short-gamma-ray bursts (SGRBs); (iii) to be the possible sources of other electromagnetic and neutrino emission; (iv) to be responsible for the production of a good portion of the very heavy elements in the Universe. When viewed in this light, BNS mergers naturally appear as Einstein’s richest laboratory, where highly nonlinear gravitational effects blend with complex microphysical processes and yield astonishing astrophysical phenomena.

As we will discuss in more detail in the following Section, the typical scenario leading to SGRBs assumes that a system composed of a rotating black hole and a surrounding massive torus is formed after the merger [29, 30]. A large number of numerical simulations [31–35] have confirmed that this

¹ With “*binary neutron-star*” systems we here refer to binary systems composed of two neutron stars; in astronomy, such systems are often called “*double neutron-star*” systems in order to distinguish them from binary systems in which one star is a neutron star and the other a white dwarf.

TABLE I. Observational data of neutron stars in binary neutron-star systems containing a pulsar. Reported in the various columns are: the name of the binary, the total (gravitational) mass M_{tot} , the (gravitational) masses of the pulsar and that of its neutron-star companion M_A, M_B , the mass ratio $q \leq 1$, the orbital period T_{orb} , the projected semi-major axis of the orbit R (i.e., the projection of the semi-major axis onto the line of sight), the orbital eccentricity e_{orb} , the distance from the Earth, the barycentric rotation frequency f_s , and the inferred surface magnetic dipole field B_{surf} . The data are taken from the respective references and truncated to four significant digits for the masses and to two significant digits for the rest. Note that in the case of the “double pulsar” system J0737-3039 (the only double system where both neutron stars are detectable as pulsars), the magnetic field of the second-formed pulsar (not reported in this table) is estimated to be $1.59\text{E}+12$ G.

Name	M_{tot} [M_{\odot}]	M_A [M_{\odot}]	M_B [M_{\odot}]	q	T_{orb} [days]	R [light s]	e_{orb}	D [kpc]	f_s [Hz]	B_{surf} [G]
J0453+1559 [8]	2.734	1.559	1.174	0.75	4.1	14	0.11	1.8	22	9.3E+09
J0737-3039 [9]	2.587	1.338	1.249	0.93	0.10	1.4	0.088	1.1	44	6.4E+09
J1518+4904 [10]	2.718	<1.766	>0.951	>0.54	8.6	20	0.25	0.7	24	9.6E+08
B1534+12 [11]	2.678	1.333	1.345	0.99	0.42	3.7	0.27	1.0	26	9.6E+09
J1753-2240 [12]	–	–	–	–	14	18	0.30	3.5	10	9.7E+09
J1756-2251 [13]	2.577	1.341	1.23	0.92	0.32	2.8	0.18	0.73	35	5.4E+09
J1807-2500B [14]	2.571	1.366	1.21	0.89	1.0	29	0.75	–	239	$\leq 9.8\text{E}+08$
J1811-1736 [15]	2.571	<1.478	>1.002	>0.68	19	35	0.83	5.9	9.6	9.8E+09
J1829+2456 [16]	2.59	<1.298	>1.273	>0.98	1.2	7.2	0.14	0.74	24	1.5E+09
J1906+0746 [17]	2.613	1.291	1.322	0.98	0.17	1.4	0.085	7.4	6.9	1.7E+12
J1913+1102 [18]	2.875	<1.84	>1.04	>0.56	0.21	1.8	0.090	13	1.1	2.1E+09
B1913+16 [19]	2.828	1.449	1.389	0.96	0.32	2.3	0.62	7.1	17	2.3E+10
J1930-1852 [20]	2.59	<1.199	>1.363	>0.88	45	87	0.40	2.3	5.4	6.0E+10
B2127+11C [21]	2.713	1.358	1.354	1.0	0.34	2.5	0.68	13	33	1.2E+10

scenario can be attained through BNS mergers unless the progenitor stars have very small masses [smaller than half of the maximum allowed mass for neutron stars with a given equation of state (EOS)], or when the merged object collapses to a black hole as a uniformly rotating neutron star in vacuum [36]. Furthermore, if sufficiently massive, the torus could provide the large amount of energy observed in SGRBs, either through neutrino processes or by extracting the rotational energy of the black hole via magnetic fields [30, 37]. Furthermore, if the neutron stars in the binary have relatively large magnetic fields and extended magnetospheres, the inspiral could also be accompanied by a precursor electromagnetic signal [38], while after the merger magnetically confined jet structures may form once a torus is present around the black hole [39–42].

Possible evidence that a BNS merger can be behind the phenomenology associated with SGRBs has emerged recently from the infrared excess in the afterglow curve of Swift’s short gamma-ray burst SGRB 130603B [43, 44], which has been interpreted as a “macronova” emission [45, 46] (sometimes also referred to as “kilonova” [47]), i.e., as due to the radioactive decay of by-products of the r -processed matter from the material ejected in the merger². Other macronova candidates,

² We will discuss this further in Section VI, but we briefly recall here that r (or rapid) processes are nucleosynthetic processes

e.g., GRB 060614 and GRB 050709 [48, 49], are presently being considered. For instance, strong evidence for a macronova component has been found recently in the peculiar long-short event GRB 060614 [48] and in its afterglow [50], while a careful re-examination of the afterglow of SGRB 050709, the first short event with an identified optical afterglow, has highlighted a macronova component [49].

The observations of the infrared transient in these afterglows are important not only because they provide a potential observational link between two distinct phenomena (i.e., a SGRB explosion and a radioactive decay), but also because they suggest that BNSs can be the site of active and intense nucleosynthesis. Additional evidence in this direction is offered by the Solar system abundance of ^{244}Pu [51, 52] and recent observations of r -process enriched stars in a metal-poor ultra-faint dwarf galaxy [53]. Both of these observations suggest that r -process elements might be preferentially produced in rare/high-yield events such as mergers instead of common/low-yield occurrences such as core-collapse supernovae.

Given the complex nonlinear nature of merging BNSs, it is inevitable that fully three-dimensional numerical simulations are the only tool available for studying these processes accurately and with a sufficient degree of realism. At present, there are about a dozen numerical codes in groups across the world that are able to produce meaningful results about BNS mergers. Most of these codes solve the full Einstein equations without approximations, together with the equations of relativistic hydrodynamics and/or (resistive) magnetohydrodynamics (MHD) equations. However, there are also codes that treat matter with smoothed-particle-hydrodynamics (SPH) methods and with some approximate treatment of gravity, which is however balanced by more advanced treatments in the microphysical processes.

Each of these codes represents a complex computational infrastructure built over the last decade (if not more) and that in most cases already provides, together with an accurate description of the bulk motion of matter (before and after the merger), also an approximate representation of the microphysical aspects related to the EOS, to the neutrino radiation transport, to the nuclear reactions taking place in the ejected matter, and, ultimately, to the electromagnetic signal from merging BNSs. Such computational infrastructures are being continuously updated and improved, either through the use of more advanced numerical methods, through the development of novel formulations of the equations, or through the introduction of new and more refined levels of microphysical description. Finally, all of these codes also share common scientific goals: a faithful representation of the gravitational-wave signal produced before and after the merger, as well as an interpretative and predictive description of the phenomenology behind SGRBs. This Report is meant to provide a general but possibly detailed description of the progress achieved in the numerous areas touched up by investigations of BNS mergers and hence to provide a snapshot of the status of the field and of the challenges and goals that lay ahead.

The Report is organised as follows: we start in Section II with a brief overview of the basic features of the inspiral, merger and post-merger of binary systems of neutron stars. This is then followed in Section III by a succinct reminder of the most common formulation of the set of equations needed to simulate the dynamics of BNSs, while the problem of computing initial data is reviewed in Section IV. With Section V we will start our review of the progress in simulations in pure hydrodynamics, leaving treatments that include magnetic fields and neutrino transport to Section VI. There, special attention is given to the ejecta, which are thought to produce heavy elements and electromagnetic emission in terms of a macronova signal. Finally, Section VII is dedicated to the discussion of more advanced techniques and scenarios, which include: high-order numerical methods, the dynamics of

involving the rapid capture of neutrons.

BNSs in alternative theories of gravity, as well as the dynamics of binary neutron stars in relativistic collisions. A concluding Section VIII will summarise the status of research and its future prospects.

We here use a spacelike signature $(-, +, +, +)$ and a system of units in which $c = G = M_{\odot} = 1$ (unless explicitly shown otherwise for convenience). Greek indices are taken to run from 0 to 3, Latin indices from 1 to 3 and we adopt the standard convention for the summation over repeated indices. Finally, reported below is also a quick list of the acronyms adopted in the paper:

ADM:	Arnowitt, Deser, Misner
AMR:	adaptive mesh refinement
BNS:	binary neutron stars
BSSNOK:	Baumgarte, Shapiro, Shibata, Nakamura, Oohara, Kojima
CCZ4:	conformal and covariant Z4
EOB:	effective one body
EOS:	equation of state
ET:	Einstein Telescope
HMNS:	hypermassive neutron star
HRSC:	high resolution shock capturing
IMHD:	ideal magnetohydrodynamics
KHI:	Kelvin-Helmholtz instability
LIGO:	Laser Interferometer Gravitational-Wave Observatory
MHD:	magnetohydrodynamics
MRI:	magnetorotational instability
PSD:	power spectral density
RMHD:	resistive magnetohydrodynamics
SGRB:	short gamma-ray burst
SMNS:	supramassive neutron star
SNR:	signal-to-noise ratio
TOV:	Tolman, Oppenheimer, Volkoff

II. BROADBRUSH PICTURE

Possibly the best way to summarise the complex sequence of events that is expected to accompany the evolution of a binary system of neutron stars is by using a broadbrush picture such as the one illustrated schematically in Fig. 1. More specifically, the diagram shows on the horizontal axis the progress of time during the evolution of the system (the intervals in square brackets indicate the expected duration range of each stage), while on the vertical axis it displays the ratio of the total (gravitational) mass of the binary (i.e., the sum of the gravitational masses of the stars composing the system), M , to the maximum mass of an isolated nonrotating star,³ M_{TOV} . Because the EOS describing neutron stars is still unknown, the precise value of M_{TOV} cannot be determined. However, astronomical observations indicate that it should be larger than about two solar masses, since there are two different systems that have been measured to have masses in this range: PSR J0348+0432 with $M = 2.01 \pm 0.04 M_{\odot}$ [56], and PSR J1614-2230 with $M = 1.97 \pm 0.04 M_{\odot}$ [57].

Also indicated in the various snapshots of Fig. 1 are the typical frequencies at which the corresponding gravitational waves are expected to be emitted. Note that in all cases, the binary system evolves on the radiation-reaction timescale, i.e., on the timescale set by the loss of energy and angular momentum via gravitational radiation; this stage lasts for millions of years at the separations at which BNSs are presently observed (cf., Table I). As can be deduced from Table I, the total gravitational masses of the known galactic neutron-star binaries are in the narrow range $2.57 - 2.88 M_{\odot}$; in addition the masses of the two stars are nearly equal, with differences that are 10% in general and of 30% at most. Under these conditions, the stars will inspiral down to very small distances (i.e., few tens of kilometres) without suffering tidal disruptions and hence with a rest-mass prior to the merger which is essentially the same as the initial one (the amount of matter lost during the inspiral has been estimated to be $\ll 10^{-4} M_{\odot}$ [58]).

As the binary reaches a separation small enough that the changes in the orbits take place on a timescale of a few seconds only, finite-size effects such as the tidal deformability of the stars become important and produce non-negligible changes in the orbits. Numerical-relativity simulations are the only effective tools to describe the dynamics of the system in detail from this point onward.

The simplest scenario to illustrate is the one of “very high-mass” systems, that is, binaries in which the two component neutron stars have very large masses, i.e., $M/M_{\text{TOV}} \sim 1.5 - 2.0$ (top row of Fig. 1). In this case, which is not expected to be statistically very frequent, the merger will be accompanied by the “prompt” collapse of the binary-merger product⁴ to a rotating black hole of dimensionless spin $J/M^2 \simeq 0.7 - 0.8$, surrounded by a hot accretion torus with mass $M_{\text{torus}} \sim 0.01 - 0.1 M_{\odot}$, depending on the mass ratio and EOS. The torus will ultimately accrete onto the black hole on a timescale set by the most efficient process removing angular momentum, i.e., gravitational radiation, magnetic fields or viscous processes, ultimately leading to an isolated rotating black hole in vacuum. For any of the mentioned processes, the timescale can be roughly estimated to be of the order of $1 - 10$ s.

A second scenario to be considered is the one in which the two component neutron stars have masses that are not very large, but above the maximum mass of nonrotating stars, i.e., $M/M_{\text{TOV}} \sim 1.3 - 1.5$ (middle row of Fig. 1). In this case, which is expected to be statistically rather frequent if $M_{\text{TOV}} \sim 2.0 - 2.1 M_{\odot}$, the binary-merger product is expected to be initially a *hypermassive neutron star (HMNS)*, i.e., a neutron star with a mass above the limit for uniformly rotating neutron

³ An isolated nonrotating neutron star is the solution of the Tolman-Oppenheimer-Volkoff (TOV) equation [54, 55] and so it is often called a “TOV” star.

⁴ We define as “binary-merger product” the generic object produced after the merger, which can actually change its nature over time. This definition is intentionally vague since we want to include a multiplicity of possibilities. In fact, depending on the total mass and mass ratio of the binary, the EOS, and the time after the merger under consideration, the binary-merger product can either be a *stable* object, i.e., a black hole or a neutron star, or an *metastable* one, i.e., an object that will eventually reach one of the two stable states mentioned above on timescales that can be much larger than the dynamical timescale.

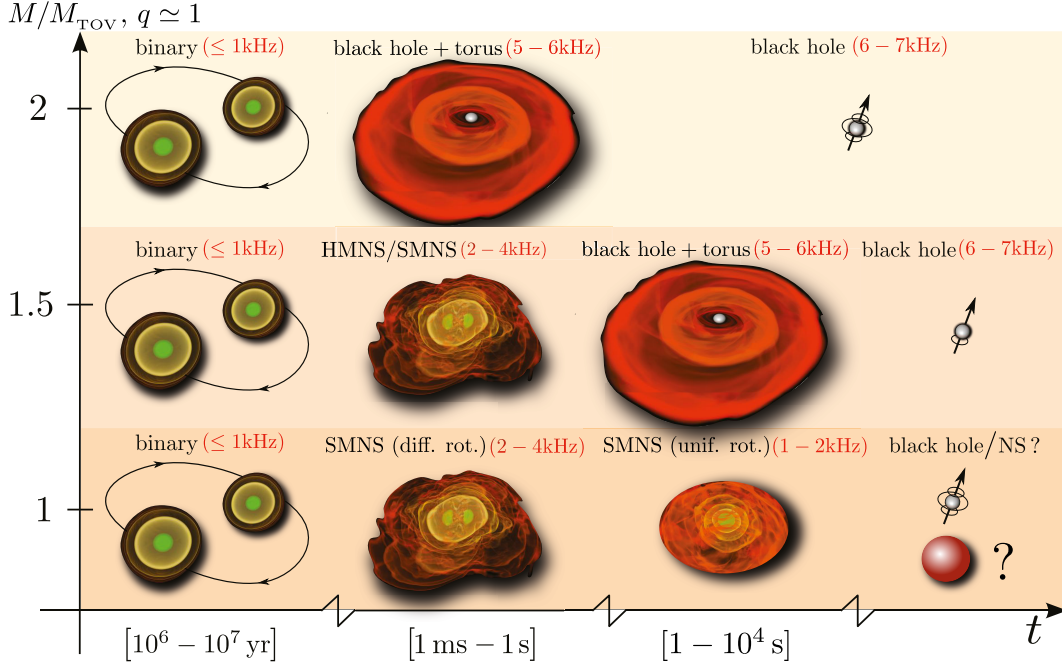


FIG. 1. Schematic diagram illustrating the various stages in the evolution of an equal-mass binary system of neutron stars as a function of the initial mass of the binary. Depending on the initial total mass of the binary M , and on how it relates to the maximum mass of a nonrotating neutron star M_{TOV} , the binary can either collapse promptly to a black hole surrounded by a torus (top row), or give rise to an HMNS (or an SMNS) that ultimately collapses to a black hole and torus (middle row), or even lead to a SMNS (first differentially and subsequently uniformly rotating) neutron star that eventually yields a black hole or a nonrotating neutron star (bottom row). Also indicated in red are the typical frequencies at which gravitational waves are expected to be emitted [Adapted from Ref. [59] by permission of Oxford University Press www.oup.com].

stars M_{max} ⁵. Because of its large angular momentum and shear, the HMNS is dynamically unstable to nonlinear instabilities leading to a bar-mode deformation [61–65], and it could even be subject to an $m = 1$ shear instability⁶ [67–73], if a corotation frequency develops within the HMNS.

Indeed, the collapse of the HMNS to a rotating black hole is temporarily prevented by its differential rotation, but a number of dissipative effects, such as magnetic fields, viscosity, or gravitational-wave emission, will act so as to remove the differential rotation. This will bring the HMNS towards a configuration that is either still differentially rotating but unstable to gravitational collapse, or to a configuration that is uniformly rotating but spinning down because of angular-momentum loss via, say, electromagnetic emission or neutrino losses. In the first case, the HMNS will collapse on a dynamical timescale producing a black-hole–torus configuration as the one discussed above for the “prompt” collapse. In the second case, instead, the HMNS, by losing its differential rotation⁷ will

⁵ We recall that a recent investigation exploiting universal relations has shown that for any EOS it is possible to relate M_{TOV} to the maximum mass that can be supported by uniform rotation M_{max} simply as $M_{\text{max}} \simeq (1.203 \pm 0.022) M_{\text{TOV}}$ [60].

⁶ As widely known, stellar deformations can be described decomposing the linear perturbations of the energy or rest-mass density as a sum of quasi-normal modes that are characterized by the indices (ℓ, m) of the spherical harmonic functions. Then the m mentioned in the text is the dominant term of such expansion. $m = 0$ is a spherical spherical perturbation, $m = 1$ is a one-lobed perturbation, $m = 2$ is a bar-shaped perturbation. See Ref. [66] for a review.

⁷ This process will reduce the gravitational mass of the HMNS, even though its rest mass remains essentially constant, apart from the small losses due to the emission of winds and that should not remove more than a few percent in rest mass.

evolve into a so-called *supramassive neutron star* (SMNS), i.e., an axisymmetric rotating (either differentially or uniformly) neutron star with mass exceeding the limit for nonrotating neutron stars, i.e., with mass $M_{\text{TOV}} \leq M \leq M_{\text{max}}$. Eventually, when slowed down sufficiently, the SMNS will reach the stability line to gravitational collapse, producing, again, a rotating black hole and an accretion torus. Because an SMNS can also be differentially rotating, depending on the actual value of M_{max} it is possible that the merger will never lead to an HMNS but directly to an SMNS, which then follows the evolution described above (see also the bottom row of Fig. 1). We should also mention that it has been pointed out recently by Margalit et al. [36] that the collapse of an SMNS is unlikely to yield a torus as the specific angular momentum of the SMNS matter is below the one corresponding to stable circular orbits for the newly produced black hole. While this is correct, present simulations reveal that the SMNS is also surrounded by a certain amount of matter with essentially Keplerian angular velocities and which effectively behaves like a “disk” around the central core [74]. It is therefore reasonable, although it has not been proven, that this material will remain on stable orbits when the SMNS collapses, hence leading again to an accretion torus around a rotating black hole [75].

The final scenario that can take place arises for “very low-mass” systems, that is, binaries in which the two component neutron stars have rather small masses, i.e., $M/M_{\text{TOV}} \sim 0.9 - 1.2$ (bottom row of Fig. 1). In this case, which is also expected to be statistically rather rare, the binary-merger product is unlikely to be a black hole from the beginning. It will instead be a differentially SMNS, which will lose its angular momentum and differential rotation to produce a uniformly rotating star, either supramassive or not. In the first case, the SMNS will follow the evolutionary track described above, i.e., eventually collapsing to produce a black-hole–torus system. In the second case, however, the binary-merger product will finally evolve into a stable, nonrotating neutron star.

Although the broadbrush picture described above is now well established and supported by a number of numerical simulations carried out by several groups, the details of the picture are still far from being clear. In particular, the “delay” between the merger and the collapse to black hole of the HMNS/SMNS (which we refer to as the “lifetime” of the binary-merger product), depends nonlinearly on a number of factors (i.e., EOS, mass ratio, strength of the magnetic field, efficiency of radiative losses) and is in general rather difficult to estimate (see Sects. VB, VIA, and VIB for a discussion). Ravi and Lasky [76], combining in a simplified model a number of channels in which either the mass or the angular momentum can be lost by the binary-merger product, have roughly estimated the upper limit of the lifetime of the binary-merger product to be $\sim 10^4$ s. Clearly, ranging between a few milliseconds and a few hours, the lifetime of the binary-merger product represents one of the largest uncertainties in the post-merger dynamics of BNSs and is likely to remain as such in view of the difficulties of performing accurate numerical simulations over such long timescales.

What is clear, however, is that the highly nonlinear regimes encountered during the merger and after the merger leave numerical solutions as the only option to investigate these scenarios with sufficient precision. As a result, several groups worldwide have developed numerical codes able to solve the equations of relativistic hydrodynamics and magnetohydrodynamics, together with the Einstein equations, to model the coalescence and merger of neutron-star binaries. We will describe the most commonly used numerical methods in the following Section.

III. MATHEMATICAL SETUP

The science of solving equations numerically often has to start from the formulation of the equations themselves, since different systems of equations that are mathematically equivalent normally possess different stability and accuracy properties. In addition, also the numerical techniques employed to solve the equations obviously have a fundamental importance in the accuracy and physical consistency of the solutions. Therefore, we start with a brief review of the mathematical formulation of the equations. For additional details we refer to a series of textbooks, where these issues are presented in much greater care and length [59, 77–81].

A. Spacetime evolution: BSSNOK formulation

One common way to numerically solve the Einstein equations consists in evolving a conformal-traceless “3 + 1” formulation⁸ of the Einstein equations called BSSNOK [84–87], in which the spacetime is decomposed into three-dimensional spacelike slices, described by a metric γ_{ij} , its embedding in the full spacetime, specified by the extrinsic curvature K_{ij} , and the gauge functions α (lapse) and β^i (shift) that specify a coordinate frame. The three-metric γ_{ij} is conformally transformed via

$$\tilde{\gamma}_{ij} = \phi^2 \gamma_{ij}, \quad (1)$$

and the conformal factor⁹ ϕ is evolved as an independent variable, whereas $\tilde{\gamma}_{ij}$ is subject to the constraint $\det(\tilde{\gamma}_{ij}) = 1$ in Cartesian coordinates. The extrinsic curvature also undergoes the same conformal transformation and its trace K is evolved as an independent variable. That is, in place of K_{ij} , the following quantities are evolved

$$K := \text{tr} K_{ij} = g^{ij} K_{ij}, \quad \tilde{A}_{ij} = \phi^2 (K_{ij} - \frac{1}{3} \gamma_{ij} K), \quad (2)$$

with \tilde{A}_{ij} being the traceless conformal extrinsic curvature, i.e., $\text{tr} \tilde{A}_{ij} = 0$. Finally, new evolution variables are introduced, defined in terms of the Christoffel symbols $\tilde{\Gamma}_{jk}^i$ of the conformal three-metric

$$\tilde{\Gamma}^i := \tilde{\gamma}^{jk} \tilde{\Gamma}_{jk}^i. \quad (3)$$

The Einstein equations are then written as a set of evolution equations for the listed variables and

⁸ The “3 + 1” formulation, which assumes that spacetime is foliated into a family of three-dimensional spacelike hypersurfaces, labelled by their time coordinate and with a set of coordinates for each slice, was proposed by Arnowitt, Deser, and Misner [82, 83] and is known as the ADM formulation.

⁹ Note that the form of the conformal factor is arbitrary; for example, other authors, like in Refs. [77, 79], set the conformal transformation to be $\tilde{\gamma}_{ij} = e^{-4\phi} \gamma_{ij}$.

are given by

$$\partial_t \tilde{\gamma}_{ij} = -2\alpha \tilde{A}_{ij} + 2\tilde{\gamma}_{k(i} \partial_j) \beta^k - \frac{2}{3} \tilde{\gamma}_{ij} \partial_k \beta^k + \beta^k \partial_k \tilde{\gamma}_{ij}, \quad (4)$$

$$\begin{aligned} \partial_t \tilde{A}_{ij} = \phi^2 \left[-D_i D_j \alpha + \alpha \left({}^{(3)}R_{ij} - 8\pi S_{ij} \right) \right]^{\text{TF}} + \beta^k \partial_k \tilde{A}_{ij} + 2\tilde{A}_{k(i} \partial_j) \beta^k \\ + \alpha (\tilde{A}_{ij} K - 2\tilde{A}_{ik} \tilde{A}_j^k) - \frac{2}{3} \tilde{A}_{ij} \partial_k \beta^k, \end{aligned} \quad (5)$$

$$\partial_t \phi = \frac{1}{3} \phi \alpha K - \frac{1}{3} \phi \partial_i \beta^i + \beta^k \partial_k \phi, \quad (6)$$

$$\partial_t K = -D_i D^i \alpha + \alpha \left[\tilde{A}_{ij} \tilde{A}^{ij} + \frac{1}{3} K^2 + 4\pi(E + S) \right] + \beta^i \partial_i K, \quad (7)$$

$$\begin{aligned} \partial_t \tilde{\Gamma}^i = \tilde{\gamma}^{jk} \partial_j \partial_k \beta^i + \frac{1}{3} \tilde{\gamma}^{ik} \partial_k \partial_j \beta^j + \frac{2}{3} \tilde{\Gamma}^i \partial_j \beta^j - \tilde{\Gamma}^j \partial_j \beta^i - 2\tilde{A}^{ij} \partial_j \alpha + \beta^j \partial_j \tilde{\Gamma}^i \\ + 2\alpha \left(\tilde{\Gamma}_{jk}^i \tilde{A}^{jk} - 3\tilde{A}^{ij} \partial_j \ln \phi - \frac{2}{3} \tilde{\gamma}^{ij} \partial_j K \right) - 16\pi \alpha \tilde{\gamma}^{ij} S_j, \end{aligned} \quad (8)$$

where ${}^{(3)}R$ is the Ricci scalar on a three-dimensional timeslice, D_i is the covariant derivative with respect to the physical metric γ_{ij} , the index ‘‘TF’’ indicates that the trace-free part of the bracketed term is used, and E , S_j , and S_{ij} are the matter source terms defined as

$$E := n_\alpha n_\beta T^{\alpha\beta}, \quad (9)$$

$$S_i := -\gamma_{i\alpha} n_\beta T^{\alpha\beta}, \quad (10)$$

$$S_{ij} := \gamma_{i\alpha} \gamma_{j\beta} T^{\alpha\beta}, \quad (11)$$

where n_α is the future-pointing four-vector orthonormal to the spacelike hypersurface and $T^{\alpha\beta}$ is the energy-momentum tensor. The Einstein equations also lead to a set of time-independent constraint equations that are satisfied within each spacelike slice

$$\mathcal{H} := {}^{(3)}R + K^2 - K_{ij} K^{ij} - 16\pi E = 0, \quad (12)$$

$$\mathcal{M}^i := D_j (K^{ij} - \gamma^{ij} K) - 8\pi S^i = 0, \quad (13)$$

which are usually referred to as the Hamiltonian (\mathcal{H}) and momentum (\mathcal{M}^i) constraints, respectively.

The most commonly used gauges in the BSSNOK formulation (but valid also for the CCZ4 and Z4c formulation presented in the following Section) are the hyperbolic singularity-avoiding ‘‘1+log’’ slicing conditions of the form

$$(\partial_t - \beta^i \partial_i) \alpha = -f(\alpha) \alpha^2 (K - K_0), \quad (14)$$

with $f(\alpha) > 0$ and $K_0 := K(t=0)$ [87, 88], and the ‘‘Gamma-driver’’ shift conditions proposed in [88, 89], which essentially act so as to drive the $\tilde{\Gamma}^i$ to be constant

$$\partial_t^2 \beta^i = F \partial_t \tilde{\Gamma}^i - \eta \partial_t \beta^i, \quad (15)$$

where F and η are, in general, positive functions of space and time. Most often they are implemented in their first-order form:

$$\partial_t \beta^i - \beta^j \partial_j \beta^i = \frac{3}{4} \alpha B^i, \quad (16)$$

$$\partial_t B^i - \beta^j \partial_j B^i = \partial_t \tilde{\Gamma}^i - \beta^j \partial_j \tilde{\Gamma}^i - \eta B^i, \quad (17)$$

where B^i is simply an auxiliary variable. The parameter η acts as a damping coefficient and is crucial to avoid strong oscillations in the shift [88–91]. Overall, both the 1+log slicing condition and the Gamma-driver shift conditions satisfy the following basic requirements: (i) if singularities are present in the spacetime under considerations, these are avoided; (ii) if coordinate distortions take place on the spatial grid as a result of the development of large spatial curvatures, these are counteracted.

B. Spacetime evolution: CCZ4 and Z4c formulations

Another formulation that has been developed recently and is becoming increasingly popular is the so-called *CCZ4 formulation* [92]. It combines the advantages of a conformal decomposition, such as the one used in the BSSNOK formulation (i.e., well-tested hyperbolic gauges, no need for excision, robustness to imperfect boundary conditions), with the advantages of a constraint-damped formulation, such as the generalized harmonic one (i.e., exponential decay of constraint violations when these are produced). Another conformal formulation of the Z4 system, the so-called *Z4c formulation*, has also been proposed recently by [93]. This does not include all the non-principal terms coming from the covariant form of the Z4 equations, but aims at a system which is as close as possible to BSSNOK. The resulting set of equations has been applied with success to both spherically symmetric non-vacuum spacetimes, where it has shown its ability to damp and propagate away the violations of the constraints [93, 94], and to generic spacetimes [95, 96].

In essence, the CCZ4 formulation is the conformal and covariant representation of the original Z4 formulation of the Einstein equations [97], where the original elliptic constraints are converted into algebraic conditions for a new four-vector Z_μ . This formulation can be derived from the covariant Lagrangian

$$\mathcal{L} = g^{\mu\nu} [R_{\mu\nu} + 2\nabla_\mu Z_\nu], \quad (18)$$

by means of a Palatini-type variational principle [98]. The vector Z_μ measures the deviation from the Einstein field equations. The algebraic constraints $Z_\mu = 0$ amount therefore to the fulfilling of the standard Hamiltonian and momentum constraints. In order to control these constraints, the original system is supplemented with damping terms such that the true Einstein solutions (i.e., the ones satisfying the constraints) become an attractor of the enlarged set of solutions of the Z4 system [99]. The Z4 damped formulation can be written in covariant form as

$$R_{\mu\nu} + \nabla_\mu Z_\nu + \nabla_\nu Z_\mu + \kappa_1 [n_\mu Z_\nu + n_\nu Z_\mu - (1 + \kappa_2)g_{\mu\nu}n_\sigma Z^\sigma] = 8\pi(T_{\mu\nu} - \frac{1}{2}g_{\mu\nu}T), \quad (19)$$

where n_μ is the unit normal to the time slicing, $T_{\mu\nu}$ the energy-momentum tensor and T its trace.

In the CCZ4 formulation, the energy-momentum constraints become evolution equations for Z_μ , modifying the principal part of the ADM system and converting it from weakly to strongly hyperbolic [100]. The “3 + 1” decomposition of the Z4 formulation including the damping terms, i.e., the

CCZ4 formulation, reads

$$(\partial_t - \mathcal{L}_{\vec{\beta}})\gamma_{ij} = -2\alpha K_{ij}, \quad (20)$$

$$\begin{aligned} (\partial_t - \mathcal{L}_{\vec{\beta}})K_{ij} = & -\nabla_i \alpha_j + \alpha \left[R_{ij} + 2\nabla_{(i} Z_{j)} + -2K_i^l K_{lj} + (K - 2\Theta)K_{ij} - \kappa_1(1 + \kappa_2)\Theta\gamma_{ij} \right] \\ & - 8\pi\alpha \left[S_{ij} - \frac{1}{2}(S - E)\gamma_{ij} \right], \end{aligned} \quad (21)$$

$$(\partial_t - \mathcal{L}_{\vec{\beta}})\Theta = \frac{\alpha}{2} \left[R + 2\nabla_j Z^j + (K - 2\Theta)K - K^{ij}K_{ij} - 2\frac{Z^j \alpha_j}{\alpha} - 2\kappa_1(2 + \kappa_2)\Theta - 16\pi E \right], \quad (22)$$

$$(\partial_t - \mathcal{L}_{\vec{\beta}})Z_i = \alpha \left[\nabla_j (K_i^j - \delta_i^j K) + \partial_i \Theta - 2K_i^j Z_j - \Theta \frac{\alpha_i}{\alpha} - \kappa_1 Z_i - 8\pi S_i \right], \quad (23)$$

where $\mathcal{L}_{\vec{\beta}}$ is the Lie derivative along the shift vector $\vec{\beta}$, Θ is the projection of the Z4 four-vector along the normal direction, $\Theta := n_\mu Z^\mu = \alpha Z^0$, and the matter-related quantities E , S_i and S_{ij} are defined in equations (9)–(11).

Equations (20)–(23) must be complemented with suitable gauge conditions that determine the system of coordinates used during the evolution. Of all the possible options, the most interesting ones are those which preserve the hyperbolicity of the full evolution system, such as the 1 + log family and the Gamma-driver shift condition, which was introduced above [101, 102].

C. Spacetime evolution: generalized harmonic formulation

Although not widely used, another method of writing the field equations that has proven very useful and that has lead to the first evolutions of binary black-hole systems [103], is the so-called *generalized harmonic formulation* [104–109]. As the name suggests, the generalised harmonic formulation of the Einstein equations is derived by imposing the *harmonic coordinate condition*, where the four spacetime coordinates x^μ are chosen to individually satisfy wave equations: $\square x^\mu = 0$ [103, 104], where \square is the d’Alambertian operator. When imposing this condition, the Einstein equations take on a mathematically appealing form, where the principal part of the evolution equations for the four-metric is simply given by a wave equation. Furthermore, to avoid the inconvenient consequences of a strict harmonic set of coordinates (e.g., coordinate focussing and caustics), it is useful to introduce a set of four source functions H^μ

$$H^\mu := \square x^\mu = \frac{1}{\sqrt{-g}} \partial_\alpha (\sqrt{-g} g^{\alpha\beta} \partial_\beta x^\mu) = \frac{1}{\sqrt{-g}} \partial_\alpha (\sqrt{-g} g^{\alpha\mu}), \quad (24)$$

or, equivalently, $H_\mu := g_{\mu\nu} H^\nu$. In this way one obtains that

$$H_\mu = \partial_\mu (\ln \sqrt{-g}) - g^{\alpha\nu} \partial_\alpha g_{\nu\mu}. \quad (25)$$

and that the symmetric gradient of H_μ is given by

$$\partial_{(\nu} H_{\mu)} = \partial_\mu \partial_\nu (\ln \sqrt{-g}) - \frac{1}{2} (\partial_\nu g^{\alpha\beta} \partial_\alpha g_{\mu\beta} + \partial_\mu g^{\alpha\beta} \partial_\alpha g_{\nu\beta}) - \frac{1}{2} g^{\alpha\beta} (\partial_\nu \partial_\alpha g_{\beta\mu} + \partial_\mu \partial_\alpha g_{\beta\nu}). \quad (26)$$

The generalized harmonic decomposition involves replacing particular combinations of first and second derivatives of the metric in the Ricci tensor by the equivalent quantities in equations (25)–(26) and then promoting the source functions H_μ to the status of independent quantities. More

specifically, it is possible to rewrite the field equations as

$$g^{\delta\gamma}\partial_\gamma\partial_\delta g_{\alpha\beta} + \partial_\beta g^{\gamma\delta}\partial_\gamma g_{\alpha\delta} + \partial_\alpha g^{\gamma\delta}\partial_\gamma g_{\beta\delta} + 2\partial_{(\beta}H_{\alpha)} - 2H_\delta\Gamma_{\alpha\beta}^\delta + 2\Gamma_{\delta\beta}^\gamma\Gamma_{\gamma\alpha}^\delta = -8\pi(2T_{\alpha\beta} - g_{\alpha\beta}T). \quad (27)$$

As the H_μ are now four independent functions, it is necessary to specify four additional, independent differential equations for them. One can think of the functions H_μ as representing the four coordinate degrees of freedom available in general relativity. There are many conceivable ways of choosing H_μ (see, e.g., Refs. [103, 110], for some commonly used options) and ADM-style gauge conditions can also be used within the harmonic decomposition.

D. Spacetime evolution: conformally flat approximation

Some codes use an approximated formulation of the Einstein equations that assumes that the three-metric is conformal and flat:

$$\gamma_{ij} = \phi^4 \hat{\gamma}_{ij} \quad (28)$$

and

$$\hat{\gamma}_{ij} = \delta_{ij}, \quad (29)$$

where ϕ is the conformal factor and δ_{jk} is the Kronecker delta. This approximation is also referred to as the *conformally flat condition* (or Isenberg-Wilson-Mathews) [111, 112].

Apart from reducing the complexity of the hydrodynamics and metric equations, this approach also exhibits numerical stability for long evolution times, as it solves all constraint equations and thus cannot violate them by definition. In fact, the constraint equations reduce to effective flat-space elliptic equations, which are then solved with standard techniques. For example, the Hamiltonian constraint is combined with the maximal slicing condition $\text{tr} K_{ij} = 0$ and becomes

$$\nabla^2\phi = -\frac{\phi^5}{8} \left[16\pi E + K_{ij}K^{ij} \right], \quad (30)$$

where E is defined in equation (9). At each time slice, a static solution to the exact general-relativistic field equations is obtained and thus devoid of gravitational radiation. The modifications to the orbital dynamics from one time slice to the next are then obtained through some approximate prescription, e.g., post-Newtonian dynamics.

E. Matter evolution: relativistic hydrodynamics

The general-relativistic hydrodynamics equations, as given by the conservation equations for the energy-momentum tensor $T^{\mu\nu}$ and for the matter current density J^μ , are normally solved numerically after being recast into a *flux-conservative formulation* [59, 81, 113–115]. Indeed, a conservative formulation is a necessary condition to guarantee correct evolution in regions of sharp entropy generation (i.e., shocks). In essence, the conservation equations

$$\nabla_\mu J^\mu = 0, \quad \nabla_\mu T^{\mu\nu} = 0, \quad (31)$$

are written in a hyperbolic, first-order, flux-conservative form of the type

$$\partial_t \mathbf{U} + \partial_i \mathbf{F}^{(i)}(\mathbf{U}) = \mathbf{S}(\mathbf{U}), \quad (32)$$

where $\mathbf{F}^{(i)}(\mathbf{U})$ and $\mathbf{S}(\mathbf{U})$ are the flux vectors and source terms, respectively [116]. Note that the right-hand side (the source terms) does not depend on derivatives of the energy-momentum tensor.

The fluxes $\mathbf{F}^{(i)}$ and the relations between the *conserved* variables \mathbf{U} and the *primitive* (or physical) variables (i.e., the rest-mass density ρ , the Lorentz factor W , the specific enthalpy h , the three-velocity v_j) are¹⁰ [113–115]

$$\mathbf{U} = \begin{pmatrix} D \\ S_j \\ \tau \end{pmatrix} := \begin{pmatrix} \rho W \\ \rho h W^2 v_j \\ \rho h W^2 - p - D \end{pmatrix}, \quad \mathbf{F}^i = \begin{pmatrix} \alpha v^i D - \beta^i D \\ \alpha S_j^i - \beta^i S_j \\ \alpha(S^i - D v^i) - \beta^i \tau \end{pmatrix}. \quad (33)$$

The source vector has instead components

$$\mathbf{S} := \sqrt{\gamma} \begin{pmatrix} 0 \\ \frac{1}{2} \alpha S^{ik} \partial_j \gamma_{ik} + S_i \partial_j \beta^i - E \partial_j \alpha \\ \alpha S^{ij} K_{ij} - S^j \partial_j \alpha \end{pmatrix}, \quad (34)$$

where γ is the determinant of γ_{ij} . Note that in order to close the system of equations for the hydrodynamics an EOS must be specified to relate the pressure to the rest-mass density, the energy density and other properties of the fluid (e.g., the composition or the electron fraction).

The general-relativistic hydrodynamics equations are usually solved making use of high-resolution shock-capturing (HRSC) methods (see Chapter 8 of Ref. [59] or Chapter 4 of Ref. [81] for a brief overview). One of the most delicate procedures in solving the system (32) is the conversion of the conserved variables back to the primitive variables, because there is no analytical expression for it and regions of very low rest-mass density may incur into numerical failures. The treatment of vacuum or low-density regions is indeed one of the most delicate aspects of modelling numerically BNSs since regions of zero rest-mass density are not allowed within the HRSC methods normally employed to solve the system of equations (32). As a result, an artificial *atmosphere* is introduced in regions supposed to be vacuum. This creates inaccuracies, especially where the physical density is low, as in the material ejected from the BNS system; we will see in Sect. VII B how this issue has recently been addressed in an alternative way [117].

F. Matter evolution: relativistic magnetohydrodynamics

When the presence of electromagnetic fields cannot be ignored, the conservation equations (31) need to be coupled to the solution of the Maxwell equations. When simulating BNS mergers, the latter are normally solved in the so-called ideal magnetohydrodynamics (MHD) approximation, which

¹⁰ Because much of the development of this formulation has taken place at the University of Valencia, through the work of Ibáñez and of his collaborators [113–115], this formulation is also known as the “*Valencia formulation*” of the relativistic-hydrodynamics equations.

assumes that the fluid has zero resistivity and is therefore a perfect conductor. Since this assumption drastically simplifies the equations, ideal MHD (IMHD) was adopted in the first numerical-relativity simulations including magnetic fields and it is still widely used today, being considered a very good approximation at least before the actual merger. At the same time, there are several processes involving compact objects where resistive effects could play an important role and preliminary attempts to go beyond IMHD and towards resistive MHD (in particular for studying the region outside the compact objects) have been first developed in Ref. [118] and then applied in Refs. [41, 119, 120] (see the end of this Section for some more details). In what follows we summarise very briefly the basic equations employed in general-relativistic MHD simulations, focusing on the form they take in the IMHD approximation.

The two pairs of Maxwell equations can be written as [121, 122]

$$\nabla_\nu {}^*F^{\mu\nu} = 0, \quad (35)$$

$$\nabla_\nu F^{\mu\nu} = 4\pi \mathcal{J}^\mu, \quad (36)$$

where $F^{\mu\nu}$ is the Faraday (or electromagnetic) tensor, \mathcal{J} is the charge current four-vector and *F is the dual of the electromagnetic tensor defined as

$${}^*F^{\mu\nu} := \frac{1}{2} \eta^{\mu\nu\lambda\delta} F_{\lambda\delta}, \quad (37)$$

$\eta^{\mu\nu\lambda\delta}$ being the Levi-Civita pseudo-tensor. The charge current four-vector \mathcal{J} can be in general expressed as

$$\mathcal{J}^\mu = qu^\mu + \sigma F^{\mu\nu} u_\nu, \quad (38)$$

where u^μ is the fluid four-velocity, q is the proper charge density, and σ is the electric conductivity. The IMHD limit ($\sigma \rightarrow \infty$) requires that the electric field measured by the comoving observer is zero, i.e., $F^{\mu\nu} u_\nu = 0$. In this limit, the electromagnetic tensor and its dual is described completely by the magnetic field \mathbf{b} measured in the comoving frame

$$F^{\nu\sigma} = \eta^{\alpha\mu\nu\sigma} b_\alpha u_\mu, \quad {}^*F^{\mu\nu} = b^\mu u^\nu - b^\nu u^\mu, \quad (39)$$

and the Maxwell equations take the simple form

$$\nabla_\nu {}^*F^{\mu\nu} = \frac{1}{\sqrt{-g}} \partial_\nu [\sqrt{-g} (b^\mu u^\nu - b^\nu u^\mu)] = 0, \quad (40)$$

The relation between the magnetic field seen by the comoving observer, \mathbf{b} , and that seen by an Eulerian observer, \mathbf{B} , can be found by using the projection operator $P_{\mu\nu} := g_{\mu\nu} + u_\mu u_\nu$ orthogonal to u . Applying this operator to the definition of the magnetic field \mathbf{B} , one can derive the following relations

$$b^0 = \frac{WB^i v_i}{\alpha}, \quad b^i = \frac{B^i + \alpha b^0 u^i}{W}, \quad b^2 := b^\mu b_\mu = \frac{B^2 + \alpha^2 (b^0)^2}{W^2}, \quad (41)$$

where $B^2 := B^i B_i$. The time component of equations (40) provides the divergence-free condition

$$\partial_i \tilde{B}^i = 0, \quad (42)$$

where $\tilde{B}^i := \sqrt{\gamma} B^i$ (enforcing this condition in numerical simulations is a very active field of research and we will comment on this in Section VI). The spatial components of equations (40), on the other hand, yield the induction equations for the evolution of the magnetic field

$$\partial_t \tilde{B}^i = \partial_j (\tilde{v}^i \tilde{B}^j - \tilde{v}^j \tilde{B}^i), \quad (43)$$

where $\tilde{v}^i := \alpha v^i - \beta^i$. Also in the case of the solution of the IMHD equations, the large majority of research groups makes use of HRSC methods and recast the equations in a flux-conservative form as first proposed by Ref. [121], although other (small) variants have been developed and used [122, 123].

Finally, we briefly mention the challenges of resistive MHD (RMHD), which is important to describe realistic plasma instabilities and magnetic reconnection. In case of finite conductivity, in fact, a relation for the current as a function of the other fields is needed in order to close the system, and this is provided, at least in principle, by Ohm's law. In practice, however, the poor knowledge of the non-ideal microphysical properties of the matter at the merger of neutron-star binaries makes the implementation of Ohm's law very delicate, leaving ample room for phenomenological exploration. In addition to the microphysical uncertainties, including Ohm's law in the evolution equations changes their mathematical nature, introducing terms that can become stiff terms in regions of high (but finite) conductivity. Since such terms reduce considerably the timestep, making the evolution with explicit time integrators nearly impossible, successful codes [41, 118–120] have implemented schemes that apply an implicit discretization to the stiff terms and an explicit one to the non-stiff terms, i.e., implicit-explicit (IMEX) Runge-Kutta methods [59, 124].

IV. INITIAL DATA

Obviously, numerical simulations involving time evolution must start from given initial data representing essentially a snapshot of all independent evolved variables. In the case of general relativity, such initial data should be a solution of the general-relativistic (magneto)hydrodynamics equations and of the Einstein equations, in particular, of the Hamiltonian and momentum constraints, when the “3 + 1” ADM decomposition is used. Other constraints could also be present if additional fields (such as electromagnetic fields) are included.

We recall that the Hamiltonian and momentum constraints are four coupled second-order elliptic partial differential equations (PDEs) that are solved numerically through some iterative procedure that starts with an initial guess and finds successive solutions, correcting the fields until some pre-determined accuracy criteria are reached. The four constraint equations, however, are not enough to determine the ten independent components of the spacetime metric. Suggestions for determining the remaining degrees of freedom were made long ago, and a widely used approach is that of employing a conformally flat geometry, also known as the Isenberg-Wilson-Mathews approach [111, 112].

The popularity of this approach, which by construction suppresses any gravitational radiation content, stems from the fact that the restrictions of the conformal flatness of the three-metric and of maximal slicing simplify the set of equations. Furthermore, the condition of helical symmetry applied to the conservation of the stress energy tensor, that is, the requirement of the fluid fields to be time independent in the frame that corotates with the binary, is aimed at enforcing the circularity of the orbit of the BNS system. The existence of such a frame is mathematically equivalent to the existence of a “helical” Killing field, and several codes for the calculation of BNS initial data have been built adopting this assumption [125–143]¹¹.

A. Irrotational binaries

BNS systems that have evolved without close interaction with other stars are thought to be on quasi-circular orbits and with minute orbital eccentricities, i.e., $\lesssim 0.01$, having lost any initial eccentricity through the emission of gravitational radiation [145]. BNS formed by dynamical capture are expected to have higher eccentricities by the time they merge¹². While the helical symmetry condition demands exact circular orbits, configurations produced in this framework actually have eccentricities larger than those thought to be common in old BNS systems by a factor of several [151–153]. Reducing the orbital eccentricity is an important task in numerical relativity, especially in order to compute accurate gravitational waveforms during the inspiral. In fact, the presence of spurious eccentricity complicates comparisons between waveforms obtained from numerical simulations and those derived through analytical methods [154–156]. The eccentricity also affects the construction of the phenomenological hybrid templates, namely templates constructed from the matching of analytical and numerical waveforms [35, 157–159]. These are necessary because the extraction of neutron-star parameters and deformability properties, which will place constraints on the neutron-star EOS, from gravitational-wave observations relies on, and is sensitive to, the accuracy of the templates [160–163].

The spurious eccentricity originates from two main causes, the first of which being that quasi-equilibrium initial data for BNS assuming a helical Killing field ignores the radial component of the velocity of the orbiting stars. This error may be reduced by adding a radial velocity (determined

¹¹ Particular attention deserves the LORENE code [134, 144], because it is distributed publicly.

¹² Since their detection event rate is likely to be much smaller than the one corresponding to the binary evolution channel, only a few studies have been performed on these binaries [72, 146–150]. See also Sect. VD.

empirically from time evolutions or calculated from post-Newtonian expressions of inspiraling point masses) to minimise the oscillations around the inspiral orbit [164, 165]. The second cause of spurious eccentricity is in the assumption of conformal flatness for the three-geometry of the initial hypersurface, which obviously is only an approximation as it implies the lack of any gravitational-wave component in the spacetime, which cannot be correct for a binary that has since long been producing gravitational waves. The inaccuracy of the binary orbit arising from spatial conformal flatness can be removed to a high degree if one solves the full Einstein equations for all metric components, including the non-conformally-flat part of the spatial metric [111, 125, 129, 164–167]. For example, in what is called the “waveless formulation”, the field equations for the metric components become elliptic equations on an initial slice, and they yield an asymptotically flat metric. Waveless solutions may determine phase and frequency of the binary with significantly greater accuracy, particularly if one first calibrates to the frequencies of a set of quasi-equilibrium sequences in order to overcome errors in the radial motion, as seen above [164, 165].

Both the conformally flat and the waveless approximation do not constrain the dynamics of the fluid, which is instead specified by the solution of the equations of hydrostatic equilibrium. To obtain such a solution it is necessary to specify a condition on the velocity field of the matter in the star and this condition is, to a large extent, arbitrary. The simplest option is to consider the two stars as tidally locked or *corotating* [128, 168], so that the fluid in each star is static in the frame that rotates with the binary¹³. While this condition is easy to implement numerically as it leads to a number of mathematical simplifications, corotating BNSs are unlikely to exist in nature because neutron-star viscosities are thought to be insufficient to lead to locking [169], and therefore different prescriptions have been suggested. Another choice that simplifies the equations consists in considering the fluid motion inside the stars to have zero vorticity. The binaries in this case are referred to as *irrotational* [126, 170–172] and the neutron stars have a very small spin angular momentum which is counter-aligned with the orbital angular momentum. Irrotational binaries have represented, by far, the most common type of initial data for BNSs and are still widely used.

Building on the large bulk of work already carried with irrotational binaries [130–138, 141], a significant effort has been invested recently in the construction of initial data for BNS that focuses on reducing the eccentricity of the orbit. The basic approach for eccentricity reduction developed and employed by Kyutoku et al. [173] is similar to the method for eccentricity reduction for binary black holes of Pfeiffer et al. [174]. As a start, standard quasi-circular initial data are computed assuming helical symmetry, and these are evolved for about three orbits. Then, appropriate corrections to the orbital angular velocity and to the radial velocity are estimated through a fit of the time derivative of the coordinate orbital angular velocity to an analytic function. Such corrections are finally applied to the initial data, and this process is repeated until the eccentricity is reduced below the desired value. This eccentricity-reduction procedure was tested with simulations of BNSs and revealed that three successive iterations allowed for an eccentricity decrease from about 0.01 to about 0.001, which is below the threshold set for binary black-hole waveforms [175]. As expected, low-eccentricity initial data allow for smaller modulations in the evolution of the orbital separation, and the gravitational-wave amplitude and frequency. With these low-eccentricity initial data, the accuracy of gravitational waves is limited mostly by the truncation error of the numerical scheme adopted (which acts as an effective viscosity) and by the boundary conditions at the outer boundary [173], if the latter is causally connected with the location where the gravitational waves are extracted.

Still concentrating on eccentricity, but with a different goal in mind, Moldenhauer et al. [176] put forth a new method that extends the notion of helical symmetry to eccentric orbits, by approximating the elliptical orbit of each companion as instantaneously circular. This allows one to generate

¹³ The corotating configuration is the only rotation state that is fully compatible with the helical-symmetry condition and is quite common in binary systems, with the closest example being offered by the Earth-Moon system.

consistent initial data for BNS systems with high eccentricity, thought to form through dynamical capture (see Sect. VD). It was found that the spurious stellar oscillations seen in simulations of elliptic BNS with less accurate initial data are reduced by at least an order of magnitude.

B. Spinning binaries

As a way to increase the realism of the initial fluid configuration and move away from the irrotational condition, an effort has been invested recently in considering initial data for spinning neutron stars, i.e., *spinning* binaries. In principle, neutron stars in accreting binary systems could reach very high spin rates and hence it is possible that also in binary systems the neutron stars retain high spins up to the merger [177, 178]. Large spins are expected to have a noticeable effect on the inspiral and merger of the binary if the rotation period is within an order of magnitude of the orbital period [179]. However, finding ways to construct initial data for binaries with spinning neutron stars has been a difficult problem. There have been attempts to produce initial data for spinning BNSs with different methods. Some of them are also based on a conformally flat slice in the presence of a helical Killing vector and employ advanced computationally intensive iterative algorithms [179–182], while others introduce the spin in cruder manners [151, 183, 184].

Indeed, before constraint-satisfying solutions for spinning BNS systems were derived, a number of authors explored the effects of spin with less accurate initial data. In all cases, the guiding principle was that of starting from some sort of the constraint-satisfying solutions, e.g., of irrotational binaries or of isolated rotating neutron stars, and to “perturb” the system either by introducing some degree of rotation or by superposing the rotating solutions and suitably boosting them. The initial data constructed in this way is obviously constraint violating, but as long as the perturbations are small, the evolution would wash away the violations (especially if constraint-damping formulations of the equations are employed) yielding a consistent evolution. Following this spirit, Kastaun et al. [184] have explored the effect of the neutron-star spin on the black hole formed after the merger. Their initial data consisted of irrotational binaries to which various amounts of rotation in the direction orthogonal to the orbital plane were added a-posteriori on the irrotational solution to increase the total angular momentum. Although the initial data violated the constraint equations and caused oscillations in the initial stages of the evolution, the use of the constraint-damping CCZ4 formulation (see III B and Refs. [92, 93]) led to acceptable constraint violations during evolution, with on average L2 norms of the Hamiltonian constraint one order of magnitude smaller than those obtained with other methods.

Following an alternative route, Tsatsin and Marronetti [151] presented a more general method for producing initial data corresponding to spinning BNS that also allows for arbitrary orbital and radial velocities. This freedom gives more control also over the orbital eccentricity. In this work, they also avoid solving the Hamiltonian and momentum constraints and so sidestep the requirement of finding numerical solutions of elliptic equations, thus simplifying the implementation. Also in this study it was found that the constraint violations were reasonably small and comparable to those obtained with other methods after some orbits of evolution. They additionally showed that their method can produce initial-data sets that exhibit eccentricities smaller than those resulting from evolving helically symmetric initial-data sets and that possess less spurious radiation of numerical origin than that found in standard sets.

These heuristic, but overall effective approaches, were paralleled by the more rigorous work of Tichy [179, 182], who developed a formalism for the calculation of initial data of arbitrarily spinning neutron stars in binaries, once again adopting the conformally flat approximation. Tichy’s approach starts from the formulation of Shibata [172] and makes simplifying assumptions, like that the spins of each star are small and remain approximately constant, as expected from the fact that the viscosity

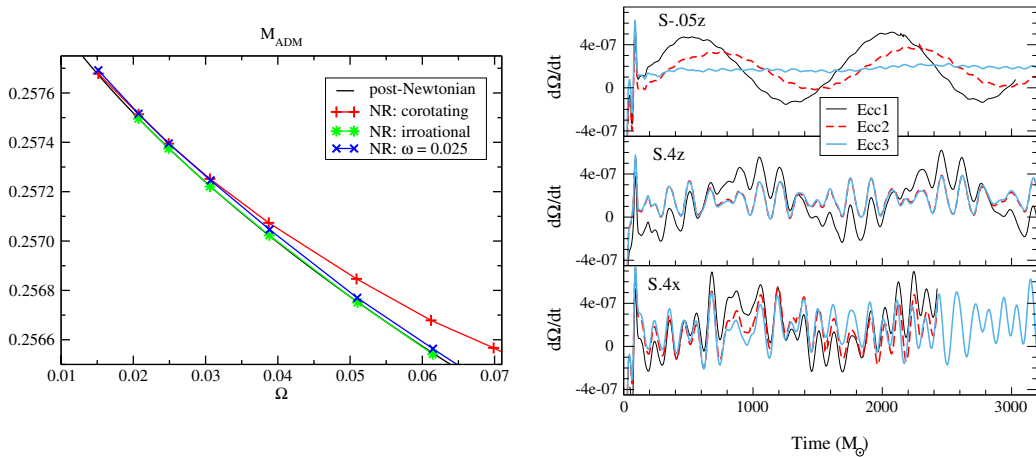


FIG. 2. *Left panel:* The gravitational mass for a binary as a function of orbital angular velocity. Shown are results for post-Newtonian point particles (solid black line), and three different numerical results (NR) for corotating stars (marked by pluses), irrotational stars (marked by stars), and a case where both stars have spin (crosses); note that the post-Newtonian results overlap closely those for irrotational stars [Reprinted with permission from Ref. [182]. © (2012) by the American Physical Society.] *Right panel:* The derivative of the binary orbital frequency as a function of time for different levels of eccentricity reduction. [Reprinted with permission from Ref. [185]. © (2015) by the American Physical Society.]

of the stars is insufficient for tidal coupling [169]. The result is a system of elliptic equations, which reduces to the known cases of irrotational and corotating binaries when appropriate parameters are chosen and has the correct Newtonian limit. By solving such a system, the neutron stars can be given arbitrary spin by choosing a (rigid or differential) rotational velocity for each star [182]. An example of the results of this formulation are shown in the left panel of Fig. 2, which displays the gravitational mass of the binary as a function of orbital angular velocity. Shown are results for post-Newtonian point particles (solid line), and three different numerical results (NR) for corotating stars (pluses), irrotational stars (marked by stars), and a case where both stars have spin (crosses)

Since its derivation, the formalism developed by Tichy [179, 182] has been adopted in a few works [143, 185]. More specifically, after adapting Tichy’s formulation [179] to a different numerical infrastructure, Tsokaros et al. [143] presented an extension of the COCAL code [167] to compute general-relativistic initial data for symmetric binary compact-star systems with a nuclear-physics EOS. The new code is able to describe also BNSs made of arbitrarily (slowly) spinning stars and was tested by comparing it to the open-source LORENE code [134, 144] in the case of irrotational and corotating binaries, finding full equivalence in the solution and in the overall error.

In a separate development, Tacik et al. [185] also followed the formalism introduced by Tichy [179, 182] and solved the initial-data equations for arbitrary spinning BNS systems with the multi-domain pseudospectral elliptic solver developed in Refs. [186, 187], where the iterative procedure of Ref. [188] is used. Tacik et al. [185] also showed how they reduce orbital eccentricity in the initial data, following an iterative procedure first introduced for binaries containing black holes [174, 187, 189, 190] and consisting in first evolving an initial-data set for a few orbits and then adjusting the initial-data parameters related to eccentricity according to the analysis of the orbital dynamics. This is summarised in the right panel of Fig. 2, which shows the evolution of the time derivative of the binary orbital frequency for different levels of eccentricity reduction.

Two remarks before concluding this Section on initial data. The first one is that recently consistent initial data were produced also for BNS systems in scalar-tensor theories of gravity [191] (see Sect. VII D for more details). The second, and alarming, remark is about the recent work of Tsokaros et al. [192], who presented a comparative analysis of the gravitational waveforms relative to essentially the same physical binary configuration when computed with two different initial-data codes and then evolved with the same evolution code. In particular, Tsokaros et al. [192] have considered the evolution of irrotational neutron-star binaries computed either with the pseudo-spectral code LORENE [134, 144] or with the newly developed finite-difference code COCAL [143]; both sets of initial data have been subsequently evolved with the high-order evolution code `WhiskyTHC` [117, 193, 194]. Despite the initial data showed global (local) differences that were $\lesssim 0.02\%$ (1%), the difference in the gravitational-wave phase at the merger time was rather large, reaching ~ 1.4 radians at the merger time, after about 3 orbits. These results are a warning signal about the highly nonlinear impact that errors in the initial data can have on the subsequent evolution and about the importance of using exactly the same initial data when comparative studies are done; at the same time, they call for the importance of sharing initial data as an effective way to quantify the error budget.

V. PURE-HYDRODYNAMIC SIMULATIONS

General-relativistic hydrodynamical simulations of BNSs started being performed in Japan almost 20 years ago [31, 195–199]. Even if nowadays many state-of-the-art codes are able to solve more complex sets of equations (e.g., for the evolution of magnetic fields, neutrino emission, etc.), simulations involving only general-relativistic hydrodynamics are still the benchmark for any new code and the necessary testbed for more advanced codes. Furthermore, in many cases, results obtained with pure hydrodynamics, most notably, gravitational waveforms, provide already a wealth of information on BNS systems, especially during the inspiral. In many respects, the inspiral may be considered the *easiest* part of the problem, in which the stars spiral towards each other as a result of gravitational-radiation losses, being scarcely or not at all affected by magnetic fields or neutrinos. Its simplicity notwithstanding, this problem is still the object of continuous efforts and improvements, which are often carried out through the synergy of numerical simulations and analytical calculations based on post-Newtonian expansions or other approximation schemes. We describe progress on this topic in Sect. V A. The inspiral has also recently attracted renewed attention with the first simulations of arbitrarily spinning BNS systems (see Sect. V A).

In what follows, we give a general description of the BNS dynamics using the figures of Ref. [32], which was one of the first to provide complete and accurate evolutions. Our description is here intentionally qualitative, as we focus on those aspects that are robust and independent of the EOS.

For millions of years a comparatively slow inspiral progressively speeds up until the two neutron stars become so close that tidal waves produced by the (tidal) interaction start appearing on the stellar surface (these are clearly visible in the second and third panels of Fig. 3). Such waves are accompanied by emission of matter stripped from the surface and by shocks that represent the evolution of small sound waves that propagate from the central regions of the stars, steepening as they move outwards in regions of smaller rest-mass density [200, 201].

At the merger, the two stars collide with a rather large impact parameter. A *vortex sheet* (or *shear interface*) develops, where the tangential component of the velocity exhibits a discontinuity. This condition is known to be unstable to very small perturbations and it can develop Kelvin-Helmholtz instability (KHI), which curls the interface forming a series of vortices at all wavelengths [202, 203]. Even if this instability is purely hydrodynamical and it is likely to be important only for binaries with very similar masses, it can have strong consequences if the stars possess magnetic fields (see Sect. VI A). It has in fact been shown that, in the presence of an initially poloidal magnetic field, this instability may lead to an exponential growth of the toroidal component [39, 65, 204–206]. Such a growth is the result of the exponentially rapid formation of vortices that curl magnetic-field lines that were initially purely poloidal. The exponential growth caused by the KHI leads to an overall amplification of the magnetic field of about three orders of magnitude [65]. At the same time, high-resolution simulations in core-collapse supernovae find that parasitic instabilities quench the MRI, with a magnetic-field amplification factor of 100 at most, independently of the initial magnetic field strength [207]. Of course, KHI and MRI are two different instabilities, but the lesson these simulations provide is that parasitic instabilities may also appear during the development of the KHI and limit the overall magnetic-field amplification; such parasitic instabilities are at present not yet apparent because of the comparatively small resolutions employed when modelling BNS mergers.

The HMNS produced from the merger may not collapse promptly to a black hole, but rather undergo large oscillations with variations such that the the maximum of the rest-mass density may grow to be twice as large (or more) as the value in the original stars (see the right panel of Fig. 4). These oscillations have a dominant $m = 2$ non-axisymmetric character [208] and will be discussed in detail in Sect. V B. As mentioned earlier, the formation and duration of the HMNS depends on the stellar masses, the EOS, the effects of radiative cooling, magnetic fields [76] and even on the development of gravitational-wave driven instabilities [209].

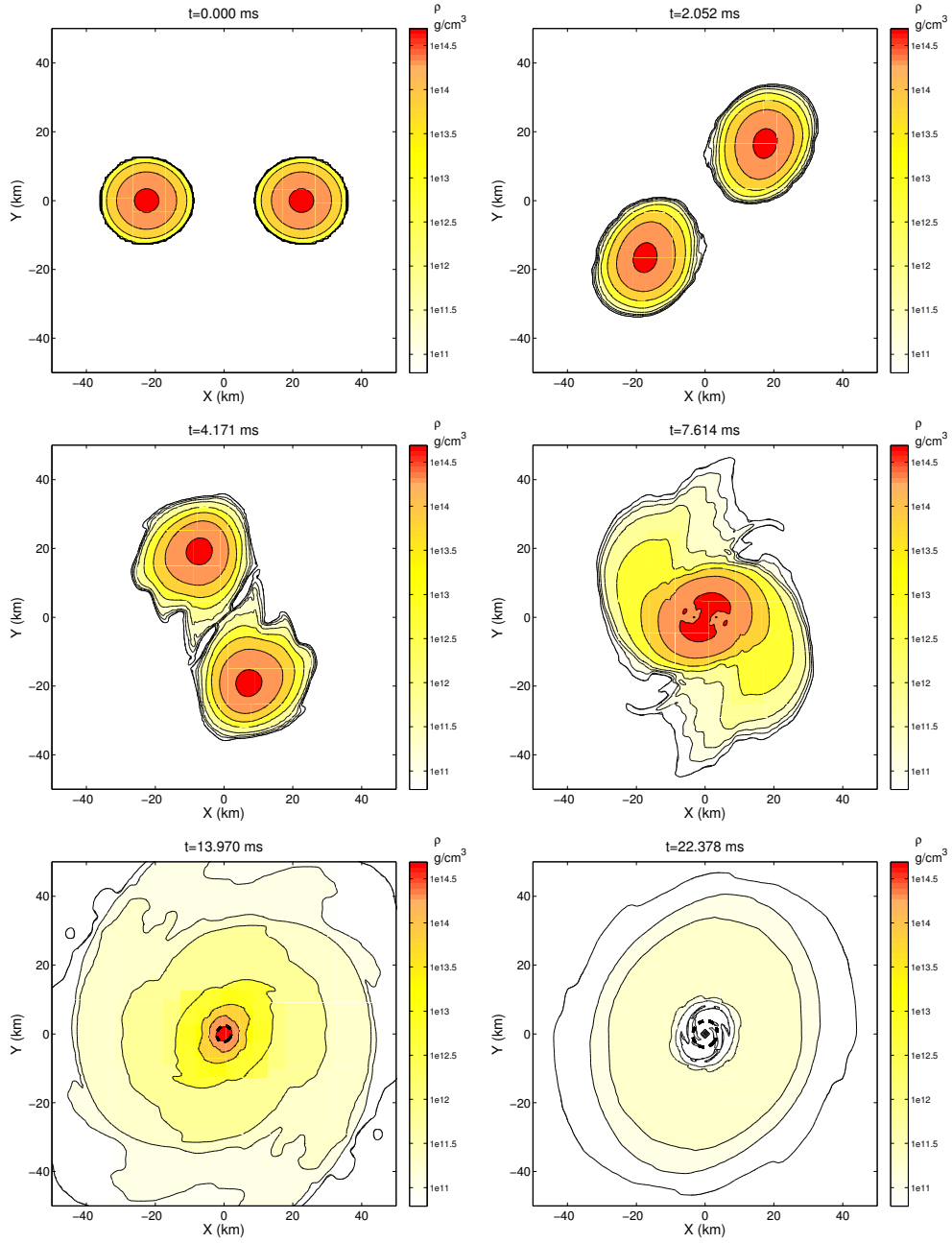


FIG. 3. Isodensity contours in the (x, y) plane for the evolution of a high-mass (individual stellar rest mass $1.625M_{\odot}$) binary with an ideal-fluid EOS. The thick dashed lines in the lower panels show the location of the apparent horizon. [Reprinted with permission from Ref. [32]. © (2008) by the American Physical Society.]

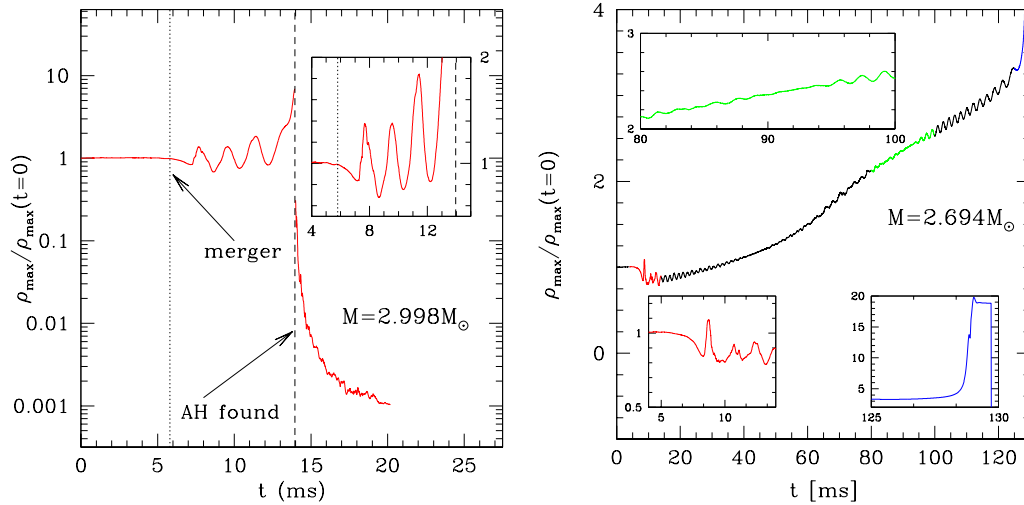


FIG. 4. *Left panel:* Evolution of the maximum rest-mass density normalized to its initial value for a high-mass (individual stellar rest mass $1.625M_{\odot}$; gravitational mass of the system $2.998M_{\odot}$) binary using an ideal-fluid EOS. Indicated with a dotted vertical line is the time at which the binary merges, while a vertical dashed line shows the time at which an apparent horizon is found. After this time, the maximum rest-mass density is computed in a region outside the apparent horizon [from Ref. [32]. © (2008) by the American Physical Society] *Right panel:* The same as in the left panel but for a low-mass binary (individual stellar rest mass $1.456M_{\odot}$; gravitational mass of the system $2.694M_{\odot}$). Note that the evolution is much longer in this case and that different colours are used to denote the different parts of the evolution (see insets). [Adapted from Ref. [58]. © IOP Publishing. Reproduced with permission. All rights reserved.]

In essentially all cases when a black hole is formed, some amount of matter remains outside of it, having sufficient angular momentum to stay orbiting around the black hole on stable orbits. In turn, this leads to the formation of an accretion torus that may be rather dense ($\rho \sim 10^{12} - 10^{13} \text{ g cm}^{-3}$) and extended horizontally for tens of kilometres and vertically for a few tens of kilometres. Also this point will be discussed in more detail in Sect. VB.

The dynamics of the inspiral and merger of a reference equal-mass binary system is summarised in Fig. 4, whose panels show the evolution of the maximum rest-mass density normalized to its initial value (after the formation of the apparent horizon, the curve shows the maximum rest-mass density in the region outside the apparent horizon). Note that together with the large oscillations, the rest-mass density also experiences a secular growth and the increased compactness eventually leads to the collapse to a rotating black hole. The differences in the two panels are essentially related to the initial mass of the system (i.e., $M = 2.998 M_{\odot}$ in the left panel and $M = 2.694 M_{\odot}$ in the right panel) and it can be seen that, for a given EOS (even a very simple one like the ideal-fluid EOS used in this case) smaller masses will yield systematically longer-lived HMNSs.

Of course, the matter dynamics described so far in the various stages of the evolution of a BNS system are imprinted in the gravitational-wave signal, which then can be used to extract important information on the properties of the neutron stars. Different parts of the evolution will provide distinct pieces of information and with different overall signal-to-noise (SNR) ratios. For example, the post-merger signal would provide rather clear signatures but at such high frequencies that it may be difficult to measure them with present detectors. On the other hand, as we will discuss in detail in

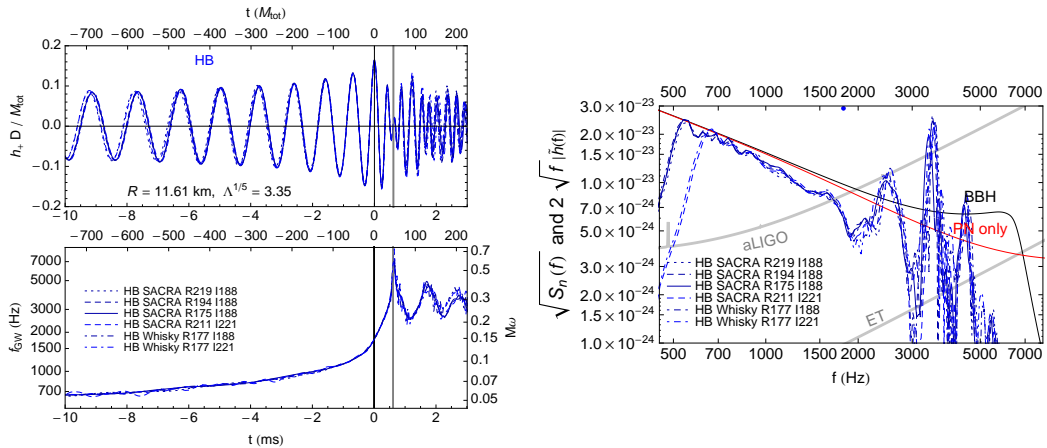


FIG. 5. *Left panel*: Waveforms and frequency evolution near merger, for model “HB” of the set of simulations of Read et al. [160]. The time of maximum amplitude is shown with a vertical black line and marks the “merger time” ($t = 0$), while a grey vertical line marks the time of maximum frequency. *Right panel*: Fourier spectra of the numerical waveforms of the left panel. Example noise spectra are indicated by thick grey lines for the Advanced LIGO high power noise [210] and the Einstein Telescope ET-D noise [211]. The starting frequency depends on the initial orbital separation in the simulation. The pre-merger waveform gives a roughly monotonically decreasing amplitude, while post-merger oscillations contribute spikes at high frequency (3000–5000 Hz). Black curves indicate the phenomenological black-hole–black-hole waveform model of Santamaría et al. [212] for the same mass parameters and red curves indicate the stationary phase approximation of a point-particle post-Newtonian inspiral [213] that includes known terms up to 3.5 post-Newtonian orders. The frequency of the first peak in the amplitude evolution is indicated by a coloured dot on the upper axis. [Reprinted with permission from Ref. [160]. © (2013) by the American Physical Society.]

the following section, the inspiral signal does depend on the EOS much more weakly, but in a way that is still measurable because it comes at frequencies where the detectors are more sensitive.

A. Inspiral and merger dynamics

In 2013, Read et al. [160] have conducted the first systematic investigation of the inspiral part of the signal making use of a number of waveforms from various groups and with the ultimate goal of improving data-analysis estimates of the measurability of matter effects in BNSs (see Fig. 5). It was estimated that with a single close-by source (at a distance of ~ 100 Mpc), the neutron star radius or the dimensionless quadrupole tidal deformability (also called polarizability coefficient)

$$\Lambda := \frac{2}{3} k_2 \left(\frac{R}{M} \right)^5, \quad (44)$$

where k_2 is the quadrupole Love number, could be constrained to about 10%. Later, it was confirmed with a more sophisticated statistical analysis that for neutron-star binaries with individual masses of $1.4 M_\odot$, the dimensionless tidal deformability Λ could be determined with about 10% accuracy by combining information from about 20–100 sources, depending on assumptions about BNS population parameters (in particular, assuming nonzero spins for the initial neutron stars shifts the necessary number of sources to higher values) [163, 214–216].

Read et al. [160] were also the first to find a universal relation between the frequency of the merger and the tidal deformability Λ of the neutron stars in an equal-mass binary (see Fig. 6). Here, the frequency of the merger is defined as the instantaneous gravitational-wave frequency at the time when the amplitude reaches its first peak. The relation is said to be universal because it is valid for all the EOSs tried, which were approximated by piecewise polytropes [217] and include a large range of compactnesses. In a later work, Bernuzzi et al. [218] proposed that the tidal polarizability parameter κ_2^T is a more general choice for the parameter to be related to the EOS, also because it is extensible to unequal-mass binaries. It is defined as (see, e.g., [218])

$$\kappa_2^T := 2 \left[q \left(\frac{X_A}{C_A} \right)^5 k_2^A + \frac{1}{q} \left(\frac{X_B}{C_B} \right)^5 k_2^B \right], \quad (45)$$

where A and B refer to the primary and secondary stars in the binary $q := M_B/M_A \leq 1$, $X_{A,B} := M_{A,B}/(M_A + M_B)$, while $k_2^{A,B}$ are the $\ell = 2$ dimensionless tidal Love numbers, and $C_{A,B} := M_{A,B}/R_{A,B}$ are the compactnesses. In the case of equal-mass binaries, $k_2^A = k_2^B = \bar{k}_2$, and expression (45) reduces to

$$\kappa_2^T := \frac{1}{8} \bar{k}_2 \left(\frac{\bar{R}}{\bar{M}} \right)^5 = \frac{3}{16} \Lambda = \frac{3}{16} \frac{\lambda}{\bar{M}^5}, \quad (46)$$

where the quantity $\lambda := \frac{2}{3} \bar{k}_2 \bar{R}^5$, is another commonly employed way of expressing the tidal Love number for equal-mass binaries [160], while $\Lambda := \lambda/\bar{M}^5$ is its dimensionless counterpart and was employed in [219] [all barred quantities reported above are meant as averages, i.e., $\bar{\Psi} := (\Psi_A + \Psi_B)/2$].

Read et al. [160] also investigated the magnitude of systematic errors arising from numerical uncertainties and hybrid construction and estimated the frequency at which such effects would interfere with template-based searches. After defining the *distinguishability* in terms of the power-spectrum-density-weighted inner product for waveforms differing in their parameter values (in this case deformability Λ), it was concluded that the dependence of the distinguishability on changes in Λ is very similar for post-Newtonian approximants and for hybridised numerical waveforms. Thus it was anticipated that post-Newtonian approximants will allow one to predict how well one will be able to infer the EOS from gravitational-wave measurements when sufficiently accurate waveforms will eventually become available.

Very recently, Hotokezaka et al. [220] have quantitatively improved the computations and estimations of Read et al. [160] in two principal directions. First, they employed new numerical-relativity simulations of irrotational binaries with longer inspirals (i.e., 14 – 16 orbits) and higher accuracy both in the initial-data setup (i.e., residual eccentricity of $\sim 10^{-3}$) and the evolution (see Ref. [221] for details)¹⁴. Second, they included in the analysis lower frequencies, down to 30 Hz, to which ground-based detectors like Advanced LIGO are more sensitive. They also adopted EOSs developed more recently [223–225]. With these improvements, Hotokezaka et al. [220] found results very similar to those of Read et al. [160], namely that deformability Λ and radius can be determined to about 10% accuracy for sources at 200 Mpc, and they explain that this is because their improvements drew the detectability in opposite directions: Increasing the frequency range increases detectability, while better numerical-relativity simulations apparently show smaller tidal effects and so decrease

¹⁴ In analogy with what presented in Ref. [156], also in Refs. [173, 220, 221] the time coordinate and phase of the waveforms are suitably adjusted to yield the desired convergence order, but the mathematical grounds for the necessity of this operation have not been investigated. Other codes can achieve convergence without such rescalings [193, 222].

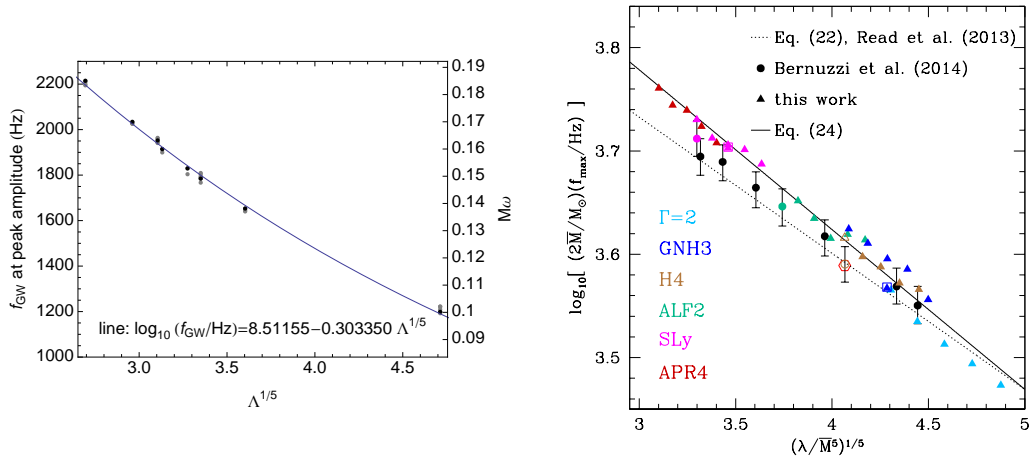


FIG. 6. *Left panel:* Instantaneous gravitational-wave frequency at the point of peak amplitude, as a function of the dimensionless tidal deformability $\Lambda^{1/5}$. For each model, the highest-resolution simulation for a given EOS is plotted in black, lower-resolution simulations in grey. An empirical fit using $\Lambda^{1/5}$ is shown. [Reprinted with permission from Ref. [160]. © (2013) by the American Physical Society.] *Right panel:* Like in the left panel, the mass-weighted frequencies at amplitude maximum f_{max} are shown as a function of the dimensionless tidal deformability $\lambda/M^5 = \Lambda$, where M is the average of the initial gravitational mass of the two stars. Filled circles refer to the data from Ref. [218], while coloured triangles indicate the data from Ref. [219], where triangles in boxes refer to the unequal-mass binaries. As in the left panel, the dotted line shows the relation suggested in Ref. [160], while the solid line represents the best fit to the data (i.e., Eq. (24) of Ref. [219]). Note that the systematic differences between circles and triangles are due to the small differences in the definition of the time of merger. [Reprinted with permission from Ref. [219]. © (2015) by the American Physical Society.]

the detectability. They conclude that if the EOS of neutron stars is stiff (radius around 13 km), it could be pinned down by measurements of the radii obtained with this method, but if the EOS of neutron stars is soft (smaller radii), a single EOS cannot be identified with this method (unless the signal is very strong, in case the source is very close).

A considerable portion of the recent research on the inspiral phase is currently conducted with post-Newtonian expansions of the Einstein equations (see, e.g., Refs. [226, 227]), coupled to the results of general-relativistic simulations. Another promising method based on an analytical approximation is the Effective-One-Body (EOB) formalism [228–231]. The high nonlinearity of the Einstein equations makes it impossible to have satisfactory analytical approximations during the most nonlinear phases of the merger, but the inspiral part can be very well approximated, even up to very close before the merger [159]. We recall that the EOB model is a relativistic generalisation of the Newtonian property that the relative motion of a two-body system is equivalent to the motion of a particle of mass $\mu := M_A M_B / (M_A + M_B)$ in the two-body potential $V(r)$ of star A and B . In the EOB formalism the effective relativistic radial potential is $W_{\text{eff}} = \sqrt{A(r)[\mu^2 + (P_\phi/r)^2]}$, where $A(r)$ is the main radial potential and P_ϕ is the centrifugal potential [159]. In the test-mass limit, $A(r)$ is equal to the Schwarzschild potential $A_{\text{Schw}} = 1 - 2M/r$ (where $M := M_A + M_B$). For extended bodies $A(r)$ changes because of two physical effects: (i) mass-ratio effects, parameterized by $\nu := \mu/M$; (ii) tidal effects, parameterized by the relativistic tidal polarizability parameters $\kappa_A^{(\ell)}$

[232–235], the most important of which is the quadrupolar (i.e., $\ell = 2$) combination $\kappa_2^T = \kappa_A^{(2)} + \kappa_B^{(2)}$ (see equation 45). More specifically, the tidal interactions are incorporated by a radial potential of the form $A = A^0(r; \nu) + A^T(r)\kappa_A^{(2)}$, where $A^0(r)$ is the EOB radial potential for binary black holes and $A^T(r)$ is an additional piece describing tidal interaction [159, 236, 237]. Recently, a further improvement of the EOB formalism has been proposed by Bernuzzi et al. [159]. It is based on a resummed version of the tidal EOB model that incorporates recent advances in the relativistic theory of tidal interactions [238–240]. Differently from previous works, no fitting parameters are introduced for the description of tidal interaction.

In Bernuzzi et al. [159], the new EOB description was compared with data from numerical simulations performed with the BAM code [222], which solves the Z4c formulation of the Einstein equations (see Sect. III B and Refs. [92, 93]). The comparison was done mainly through the gauge-invariant relation between the binding energy and the orbital angular momentum [155, 218], and an agreement within the uncertainty of the numerical data was found for all models. Previous results [154, 156, 221, 241], obtained with older versions of the EOB model not including resummation, had also found good agreement between the phases of gravitational waves simulated in numerical relativity and those predicted by EOB calculations for most of the inspiral stage except for the tidally dominated, final inspiral stage, in which the old EOB results underestimated the tidal effects. The accumulated phase difference was at most 1-3 radians in the last 15 cycles. The good performance of the EOB formalism has been recently shown for several cases also by Hotokezaka et al. [220], who compared the EOB inspiral waveform model to the ones obtained with the currently available versions of the Taylor-T4 and Taylor-F2 approximants (see, e.g., Ref. [163]). By computing the distinguishability between numerical-relativity waveforms and post-Newtonian waveforms, it appears that the Taylor approximants are worse by a factor of at most two. The authors suggested that the absence of higher-order post-Newtonian terms in the Taylor approximants is the likely source for inaccuracy, especially in the late inspiral.

In another recent development, Hinderer et al. [242] proposed further improvements of the EOB formalism that include a treatment of dynamical tides, in addition to the dominant adiabatic tides. The latter describe distorted neutron stars as remaining in hydrostatic equilibrium, namely, adjusting instantaneously to the companion’s tidal force which varies because of the orbital motion. The former, instead, arise only when the frequency of the tidal forcing becomes close to an eigenfrequency of the stellar normal modes of oscillation and result in an enhanced and more complex tidal response than in the adiabatic case. Hinderer et al. [242] validated their improved EOB gravitational waveforms by comparing with numerical simulations and found that in some cases the contribution of dynamical tides to the total deformation can be as large as 30%.

A post-Newtonian approach was also used for the determination of the redshift of gravitational-wave signals from BNSs. Messenger et al. [243], in particular, showed that the determination of the redshift of gravitational waves can be attained solely from gravitational-wave data, namely without assuming concurrent electromagnetic observations. The degeneracy in post-Newtonian waveforms between the mass parameters and the redshift was shown to be broken by tidal effects, computing which it was estimated that for a range of representative EOSs the redshift of BNS systems can be determined to an accuracy of 8% – 40% for $z < 1$ and of 9% – 65% for $1 < z < 4$. Other ways to estimate the redshift of BNS sources involve the post-merger signal [244] and will be treated in Sect. V B.

Several works are also using post-Newtonian approximation of waveforms to investigate what can reasonably be deduced about EOSs from multiple gravitational-wave observations of BNS inspirals with advanced detectors [160, 163, 214–216, 235, 236, 245]. Hinderer et al. [235] and Damour et al. [236] performed Fisher-matrix calculations (the latter using EOB waveforms) and found that it might be possible to gain information about the EOSs with advanced detectors. An important conclusion reached in Ref. [236] was that Λ can be measured at the 95% confidence level through EOB-based

merger templates in match filtered searches by the Advanced LIGO-Virgo-KAGRA detector network using gravitational-wave signals with a reasonable SNR (i.e., $\text{SNR}=16$) [236].

Recently, Barkett et al. [246] proposed a new method for computing inspiral waveforms for BNS systems by adding post-Newtonian tidal effects to full numerical simulations of binary black holes. Since black-hole vacuum simulations are faster than simulations containing matter, this method would allow to produce gravitational waveforms faster, but its accuracy is yet to be verified.

All of the results reviewed above referred to binaries that are initially irrotational. However, as mentioned in Sect. IV, progress has also been achieved recently in simulating the inspiral and merger of spinning binaries, either from constraint-violating or constraint-satisfying initial data. More precisely, the first simulations of spinning BNS mergers were performed by Kastaun et al. [184], who considered mergers of equal-mass binaries with spins of different amplitude and aligned with the orbital angular momentum. The ultimate goal of these simulations was to determine whether, as the initial spin of the two stars is increased, the black hole produced by the merger attains a maximum spin or it increases indefinitely, leading to a naked singularity. Indeed, the simulations indicated that it is the first of the two scenarios that takes place (see Sect. VB for more details) but also that the inspiral lasts longer as the two neutron stars need to shed the additional angular momentum in the system before merging. This “hang-up” effect has been observed in black-hole binaries [247–249] and is a basic prediction of the post-Newtonian equations. Nearly at the same time, also Tsatsin and Marronetti [151] simulated binaries with spins aligned and antialigned with the orbital angular momentum, using their own approach to the construction of spinning initial data (see Sect. IV). Also in this case, and in analogy with dynamics already studied in binary black holes, the merger of the binary with antialigned spins lead to a prompt collapse to a black hole, while the aligned-spin binary lead to the formation of a centrifugally supported HMNS that survived for several dynamical times before collapsing. Later, also Kastaun and Galeazzi [74] employed constraint-violating spinning initial data to investigate how the dynamical and gravitational-wave spectral properties are influenced by the presence of rotation.

However, it was not until the work of Bernuzzi et al. [250] that general-relativistic evolutions of constraint-satisfying initial data of spinning BNS with spins aligned and antialigned to the orbital angular momentum were performed. The initial data was produced with the constant-rotational-velocity approach of Tichy [179, 182], which provides a more precise measurements of the changes in the phase evolution during the inspiral due to spin. In particular, it was found that the orbital motion can be significantly affected by spin-orbit interactions which delay the merger, at least for high enough spins. During their three-orbit evolution, they observed accumulated phase differences of up to 0.7 gravitational-wave cycles between the irrotational configuration and the spinning ones. Hence they concluded that precise modelling of the late-inspiral-merger waveforms needs to include spin effects even for moderate magnitudes (see also Agathos et al. [216] for the gravitational-wave data-analysis results taking into account stellar spins). In addition, they studied the shift to higher frequencies in the main emission mode of the HMNS produced by spinning neutron stars and confirmed the results of Kastaun et al. [184] about the maximum spin attained by the black hole. While correct, all of the considerations above are hindered by the fact that a realistic estimate of the dimensionless spin parameter before the merger is not yet known and it is therefore difficult to assess whether spin effects are really going to be present in the gravitational-wave signal.

B. Post-merger dynamics

Research on the post-merger phase has been undergoing intense development over the last few years because of its importance for linking numerical simulations and astrophysical observations. The (early) post-merger is also the phase in which most of the energy in gravitational waves is emit-

ted, as pointed out in Ref. [251], even though the gravitational waves emitted in this stage are not those that give the largest signal-to-noise ratio, because their frequency range is not in the best sensitivity zone of current interferometric detectors. The numerical description of this stage is far more challenging than the inspiral one because of the highly nonlinear dynamics and of the development of strong, large-scale shocks that inevitably reduce the convergence order, thus requiring far higher resolutions than the ones normally employed. As a result, the accuracy of some quantities computed after the merger is sometimes only marginal. The most notable example of these quantities is the lifetime of the remnant (be it an HMNS or an SMNS) before its collapse to black hole; since this object is only in metastable equilibrium, even small differences in resolution or even grid setup are sufficient to change its dynamical behaviour, accelerating or slowing down its collapse to a black hole. Fortunately, other quantities, such as the spectral properties of the gravitational-wave post-merger emission appear far more robust and insensitive to the numerical details; we will discuss them later in this section.

Since the first general-relativistic simulations of BNS mergers, several works have studied the nature (neutron star or black hole) of the objects resulting from the mergers [31, 32, 69, 198, 205, 252–254]. It is of course important to establish whether a black hole forms promptly after the merger or instead an HMNS forms and lives for long times (more than 0.1 s), because the post-merger gravitational-wave signal in the two cases is clearly different. Anderson et al. [69] and Giacomazzo et al. [205] started investigating the dependence of the lifetime of the HMNS on the magnitude of the initial magnetic field in the case of magnetised binaries. However, as mentioned above, such investigations are extremely delicate since it is not straightforward to completely remove the influence of numerical artefacts on the lifetime of the remnant even in the absence of magnetic fields, at least with present resolutions.

In an alternative approach, Kaplan et al. [255] have investigated the role of thermal pressure support in hypermassive merger remnants by computing sequences of axisymmetric uniformly and differentially rotating equilibrium solutions to the general-relativistic stellar structure equations and found that this too is a subtle issue: the role of thermal effects on the stability and lifetime of a given configuration depends sensitively and in a complicated way on its details, like central or mean rest-mass density, temperature distribution, degree of differential rotation and rotation rate.

Clearly, the issue of the precise lifetime of the binary-merger product before it reaches its asymptotic state (cf., footnote 4), especially when its equilibrium is mediated by the generation of magnetic fields or radiative losses is far from being solved and will require computational resources and/or methods not yet available (cf., Sect VI A).

Recently, Paschalidis, East and collaborators [70, 71] pointed out that a one-arm spiral instability [62, 68, 256, 257] can develop in HMNSs formed by dynamical-capture and that the $m = 1$ mode associated with this instability may become the dominant oscillation mode if the HMNS persists for long enough¹⁵; this instability has been subsequently studied also in quasi-circular BNSs [73, 259]. The instability, is reminiscent of the shear instability that has been studied in detail for isolated stars [62, 68, 260–262] and seems to be correlated with the generation of vortices near the surface of the HMNS that form due to shearing at the stellar surface. These vortices then spiral in toward the center of the star, creating an underdense region near the center. The growth of the $m = 1$ mode and so of the instability, could be related to the fact that the maximum density does not reside at the center of mass of the star [263], or to the existence of a corotation band [257, 264, 265]. The instability has an imprint on the gravitational-wave signal, but the prospects of detection are not encouraging, because of the small emitted power [259].

¹⁵ The $m = 1$ mode had been studied previously together with the other modes, but it had never been found to become dominating (see, e.g., [258]).

1. Influence of the equation of state

Despite these difficulties, many researchers have taken up the challenge of studying the properties of the binary-merger product, because this may give indications on the ultra-high density EOS, the origin of SGRBs, and even the correct theory of gravity (see also Sects. [VIA](#), [VIID](#)). In what follows we will focus in particular on the determination of the EOS. While detectable differences between simulations that employed different EOSs already appear during the inspiral (see Sect. [VA](#)), the post-merger phase depends more markedly on the EOS [[159](#), [218](#), [219](#), [266–269](#)]. A note of caution is necessary here to say that post-merger waveforms are at rather high frequencies and thus probably only marginally measurable by detectors like Advanced LIGO. Third-generation detectors, such as ET [[211](#)], may provide the first realistic opportunity to use gravitational waves to decipher the stellar structure and EOS [[270](#)].

The first attempts to single out the influence of the EOS on the post-merger dynamics were done in Refs. [[32](#), [252–254](#)]. These works focused mostly on the dynamics of equal-mass binaries, as these are thought to be the most common [[177](#)] and are easier and faster to compute, since symmetries of the configuration can be exploited to save computational resources. The study of the effect of realistic EOSs in general-relativistic simulations has been subsequently brought forward by many groups. Kiuchi et al. [[140](#)] made use of the Akmal-Pandharipande-Ravenhall (APR) EOS [[271](#)]¹⁶. This nuclear-physics EOS describes matter at zero temperature and so during the simulation it needs to be combined with a “thermal” part that accounts for the energy increase due to shock heating (this is mostly done through the addition of an ideal-fluid part to the EOS; see Ref. [[59](#)] for a discussion). The resulting “*hybrid EOS*” appears to be appropriate for studying the inspiral and merger, but may not be satisfactory for studying the remnant formation and the evolution of the accretion disc around the formed black hole, because for such cases, effects associated with the thermal energy (finite temperature), neutrino cooling, and magnetic fields are likely to play an important role (see Sects. [VIA](#), [VIB](#)). In another work of the same group [[273](#)], the dependence of the dynamical behavior of BNS mergers on the EOS of the nuclear-density matter with piecewise-polytropic EOSs [[217](#)] was studied. Table I in Ref. [[273](#)] usefully summarizes the piecewise polytropic parameters of several realistic EOSs.

One family of EOSs that has received special attention in the past years is that describing strange matter, namely matter containing hyperons, which are nucleons containing strange quarks. The strange-matter hypothesis [[274](#)] considers the possibility that the absolute ground state of matter might not be formed by iron nuclei but by strange quark matter: a mixture of up, down, and strange quarks. This hypothesis introduced the possibility that compact stars could be stars made also of strange-quark matter, or strange stars [[275](#), [276](#)]. One of the astrophysical consequences of this is the possibility that collision events of two strange stars lead to the ejection of strangelets, namely small lumps of strange quark matter.

Although the occurrence of hyperons at very large nuclear densities is rather natural, hyperonic EOSs are generally very soft and currently disfavoured by the observation of a $2M_{\odot}$ star [[56](#), [57](#)], which they can hardly reproduce, except by fine tuning of the parameters (see, e.g., [[277–279](#)]). This basic inconsistency between the expectations of many nuclear physicists and the observational evidence of very massive neutron stars is normally referred to as the “hyperon puzzle”; those supporting the use of hyperonic EOSs also state that the existence of exotic phases in strange stars remains unconstrained and could lead to higher masses [[280](#)]. Additional work is needed to settle this “hyperon puzzle” and we will present results on strange-star simulations setting these doubts aside.

¹⁶ The APR EOS, and many of the proposed EOSs, were later found to violate the light-speed constraint at very high densities and phenomenological constraints [[272](#)], but no strong conclusions can be made to rule out such EOSs on this basis because the constraints themselves are affected by errors.

The first investigations of binary strange stars were those of Bauswein et al. [281, 282], who employed the MIT bag model [283]. Within this model, quarks are considered as a free or weakly interacting Fermi gas and the nonperturbative QCD interaction is simulated by a finite pressure of the vacuum, the *bag constant* B . Three-dimensional general-relativistic simulations with conformally flat gravity of the coalescence of strange stars were performed and the possibility to discriminate on the strange matter hypothesis by means of gravitational-wave measurements was explored. The dynamics of mergers of strange stars, which are usually more compact, is different from those of neutron-star mergers, most notably in the tidal disruption during the merger. Furthermore, instead of forming dilute halo-structures around the binary-merger product, as in the case of neutron-star mergers, the coalescence of strange stars results in a differentially rotating hypermassive object with a sharp surface layer surrounded by a geometrically thin, clumpy high-density strange-quark-matter disc. It was found that in some cases (some types of EOS and stellar properties) the analysis of the gravitational-wave signals emitted by strange-star mergers showed that it may be possible to discern whether strange-star or neutron-star mergers produced the emission. In particular, it was found that the maximal frequency during the inspiral and the frequency of the oscillations of the post-merger remnant are in general higher for strange-star mergers than for neutron-star mergers. In other cases, however, there remains a degeneracy among different models, and a conclusion about the strange-matter hypothesis could be reached only if other types of observations (e.g., of cosmic rays) were available.

Strange-matter EOSs were later studied with a fully general-relativistic code in a series of articles by Sekiguchi, Kiuchi and collaborators [284–287], who showed results of simulations performed by incorporating both nucleonic and hyperonic finite-temperature EOSs (and neutrino cooling as well, cf., Sect. VI B). It was found that also for the hyperonic EOS, an HMNS is first formed after the merger and subsequently collapses to a black hole. The radius of such an HMNS decreases in time because of the increase of the mass fraction of hyperons and the consequent decrease in pressure support. Such a shrinking is noticeably larger than the one simply due to angular-momentum loss through gravitational-wave emission that is present also in nucleonic EOSs. These differences in the dynamics are clearly visible in the gravitational-wave signal, whose characteristic peak frequency has an increase of 20% – 30% during the HMNS evolution. By contrast, for nucleonic EOSs, the peak gravitational-wave frequency in the HMNS phase is approximately constant on the timescales considered. It was also stressed that these results raise a warning about using the peak frequency of the gravitational-wave spectrum to extract information of the neutron-star matter (see below), because it may evolve and so make the relation of the peak frequency with the HMNS structure ambiguous. Finally, it was found that the torus mass for the hyperonic EOS is smaller than that for nucleonic EOSs, thus making hyperonic EOSs less favourable for the description of SGRBs.

2. Spectral properties of the gravitational-wave signal

In addition to simulating BNS mergers with various EOSs, it is important to find ways to connect future gravitational-wave observation with the EOS of the neutron stars. Recently there have been several suggestions on how to achieve this, based either on the signature represented by the tidal corrections to the orbital phase or on the power spectral density (PSD) of the post-merger gravitational waveforms or on the frequency evolution of the same. The first approach, described in Sect. V A, is reasonably well understood analytically [155, 160, 241, 268, 288] and can be tracked accurately with advanced high-order numerical codes [117, 193]. Here we describe works on the post-merger approach in some detail.

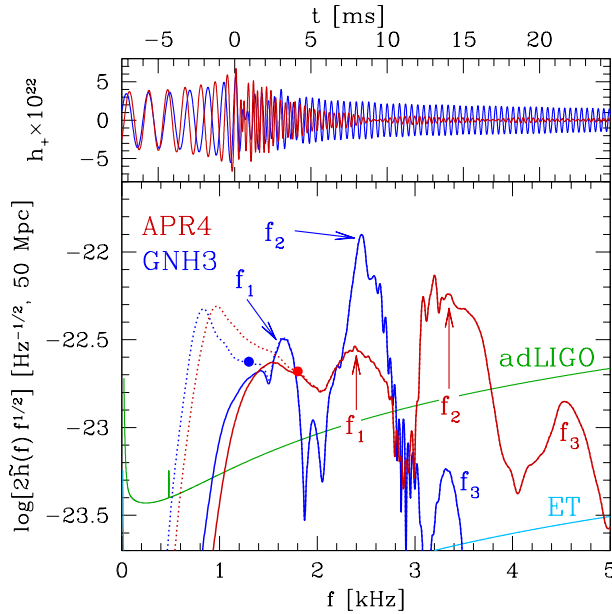


FIG. 7. Top sub-panel: evolution of h_+ for binaries with the APR4 and GNH3 EOSs (dark-red and blue lines, respectively) for sources at a polar distance of 50 Mpc. Bottom sub-panel: spectral density $2\dot{h}(f)f^{1/2}$ windowed after the merger for the two EOSs and sensitivity curves of Advanced LIGO (green line) and ET (light-blue line); the dotted lines show the power in the inspiral, while the circles mark the contact frequency [Reprinted with permission from Ref. [267]. © (2014) by the American Physical Society.]

Hotokezaka et al. [289] used their adaptive mesh-refinement (AMR) code¹⁷ SACRA [254] to perform a large number of simulations with a variety of mass ranges and EOSs (as done before, approximate finite-temperature effects were added to the cold EOSs through an additional ideal-fluid term), in order to find universal features of the frequency evolution of gravitational waves emitted by the HMNS formed after the merger. In their analysis they found it convenient to decompose the merger and post-merger gravitational-wave emission in four different parts: (i) a peak in frequency and amplitude soon after the merger starts; (ii) a decrease in amplitude during the merger and a new increase when the HMNS forms; (iii) a damped oscillation of the frequency during the HMNS phase lasting for several oscillation periods and eventually settling to an approximately constant value (although a long-term secular change associated with the change of the state of the HMNSs is always present); (iv) a final decrease in the amplitude during the HMNS phase, either monotonical or with modulations. Based on this, they find an optimal 13-parameters fitting function, using which it may be possible to constrain the neutron star radius with errors of about 1 km [289].

In contrast with this multi-stage, multi-parameter description of Hotokezaka et al. [289], other groups have concentrated on the analysis of the full PSD of the post-merger signal, isolating those spectral features (i.e., peaks) that could be used to constrain the properties of the nuclear-physics EOSs. As a reference, we show in Fig. 7 the PSDs of some representative gravitational waves

¹⁷ In previous works by this group, described above, a different code with a uniform grid had been used.

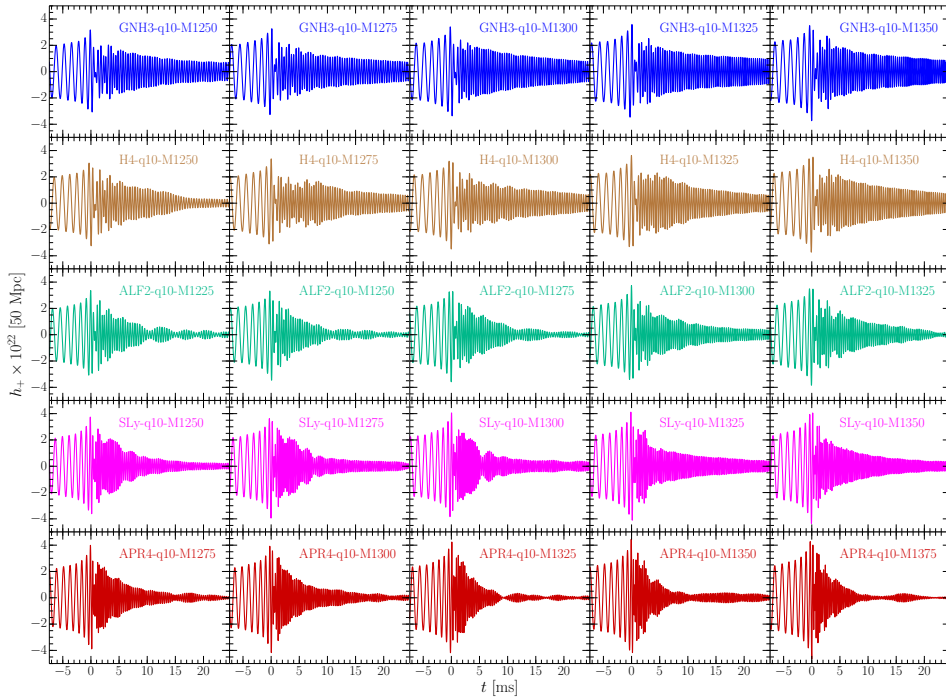


FIG. 8. Gravitational waveforms for equal-mass binaries with nucleonic EOSs, shown in different colours. Each column refers to a given initial gravitational mass. [Reprinted with permission from Ref. [219]. © (2015) by the American Physical Society.]

when compared with the sensitivity curves of current and future gravitational-wave detectors [267]. More specifically, two examples are presented in Fig. 7, which refers to two equal-mass binaries with APR4 and GNH3 EOSs, and with individual gravitational masses at infinite separation of $\bar{M}/M_\odot = 1.325$, where \bar{M} is the average of the initial gravitational mass of the two stars. The top sub-panel shows the evolution of the $\ell = m = 2$ plus polarization of the strain ($h_+ \sim h_+^{22}$), aligned at the merger for sources at a polar distance of 50 Mpc (dark-red and blue lines for the APR4 and GNH3 EOSs, respectively). The bottom panel, on the other hand, shows the spectral densities $2\tilde{h}(f)f^{1/2}$ windowed after the merger for the two EOSs, comparing them with the sensitivity curves of Advanced LIGO [290] (green line) and of the Einstein Telescope [291, 292] (ET; light-blue line). The dotted lines refer to the whole time series and hence, where visible, indicate the power during the last phase of the inspiral, while the circles mark the “contact frequency” $f_{\text{cont}} = \mathcal{C}^{3/2}/(2\pi\bar{M})$ [236], where $\mathcal{C} := \bar{M}/\bar{R}$ is the average compactness, $\bar{R} := (R_1 + R_2)/2$, and $R_{1,2}$ are the radii of the nonrotating stars associated with each binary.

Note that besides the peak at low frequencies corresponding to the inspiral (cf., dashed lines), there is one prominent peak and several other of lower amplitudes. These are related to the oscillations of the HMNS and would be absent or much smaller if a black hole forms promptly, in which case the gravitational-wave signal would terminate abruptly with a cutoff corresponding to the fundamental quasi-normal-mode frequency of the black hole [293]. The behaviour summarised in Fig. 7 is indeed quite robust and has been investigated by number of authors over the last decade [74, 208, 219, 266–269, 289, 294–303]. While some of the details of the picture that emerges from the analysis of the

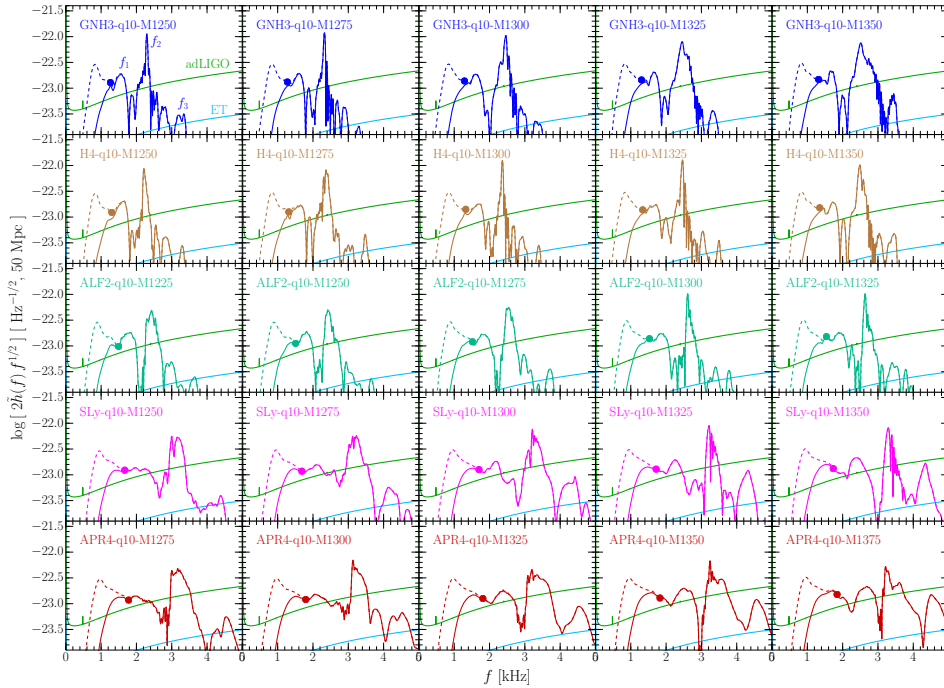


FIG. 9. PSDs $2\tilde{h}(f)f^{1/2}$ for the equal-mass binaries with nucleonic EOSs shown in Fig. 8. Solid lines of different colours refer to the high-passed waveforms, while the dashed lines refer to the full waveforms. Indicated with coloured circles are the various contact frequencies f_{cont} , while the curves of Advanced LIGO and ET are shown as green and light-blue lines, respectively [Reprinted with permission from Ref. [219]. © (2015) by the American Physical Society.]

PSDs are still fuzzy, there are also aspects that are commonly accepted. In particular, there is a widespread consensus that: (i) the post-merger gravitational-wave signal possesses spectral features that are robust and that emerge irrespective of the EOS or the mass ratio; (ii) the frequencies of the peaks in the post-merger PSD can be used to obtain important information on the stellar properties (i.e., mass and radius) and hence represent a very good proxy to deduce the EOS. This is summarised in Fig. 9, which shows the PSDs for the equal-mass binaries with nuclear-physics EOSs reported in Fig. 8. Solid lines of different colours refer to the high-passed waveforms, while the dashed lines refer to the full waveforms. Indicated with coloured circles are the various contact frequencies f_{cont} , while the curves of Advanced LIGO and ET are shown as green and light-blue lines, respectively [219].

The first detailed description of a method for extracting information about the EOS of nuclear matter by carefully investigating the spectral properties of the post-merger signal was provided by Bauswein et al. [295, 296]. After performing a large number of simulations using their conformally-flat SPH code, they pointed out that the largest peak in the PSD (whose frequency is dubbed there f_{peak}) correlates with the properties of the EOS, e.g., with the radius of the maximum-mass nonrotating star for the given EOS. The correlation found was rather tight, but this was partly due to the fact that their sample was restricted to binaries having all the same total mass (i.e., $2.7 M_{\odot}$ in the specific case). It was shown that such a correlation can be used to gain information on the high-density EOS

through gravitational-wave measurements, if the masses of the neutron stars forming the binaries are known. Additionally, it was recognized that f_{peak} corresponds to a fundamental fluid mode of the HMNS with $\ell = 2 = m$ [208, 295] and that the value of this frequency could also be used to set constraints on the maximum mass of the system and hence on the EOS [266, 304]. Subsequent analyses were performed by a number of groups with general-relativistic codes [219, 267, 269, 289, 299–301, 303], which confirmed that the conformally flat approximation employed by Bauswein and collaborators provided a rather accurate estimate of the largest peak frequencies in the PSDs.

Takami et al. [219, 267] presented a more advanced method to use detected gravitational waves for determining the EOS of matter in neutron stars. They used the results of a large number of accurate numerical-relativity simulations of binaries with different EOSs and different masses and identified two distinct and robust main spectral features in the post-merger phase. The first one is the largest peak in the PSD (whose frequency was called there f_2 and essentially coincides with the f_{peak} of Refs. [295, 296]). The functions describing the correlations of f_2 with the stellar properties (e.g., with the quantity $(\bar{M}/R_{\text{max}}^3)^{1/2}$, where R_{max} is the radius of the maximum-mass nonrotating star), which were first proposed by Bauswein et al. [295], are not universal, in the sense that different (linear) fits are necessary for describing the f_2 -correlations for binaries with different total masses. This conclusion can be evinced by looking at Figs. 22–24 of Bauswein et al. [296], but the different linear correlations were first explicitly computed by Takami et al. [219, 267] (see also Ref. [289]).

The second feature identified in all PSDs analysed by Takami et al. [219, 267] is the second-largest peak, which appears at lower frequencies and was called f_1 there. Clear indications were given about this low-frequency peak being related to the merger process (i.e., the first ≈ 3 ms after the merger). This was done by showing that the power in the peak is greatly diminished if the first few ms after the merger were removed from the waveform. Furthermore, a simple mechanical toy model was devised that can explain rather intuitively the main spectral features of the post-merger signal and therefore shed light on the physical interpretation of the origin of the various peaks. Despite its crudeness, the toy model was even able to reproduce the complex waveforms emitted right after the merger, hence possibly opening the way to an analytical modelling of a part of the signal [219].

More importantly, it was shown that the potential measurement of the f_1 frequency could reveal the EOS of the merging objects, since a correlation was found between the f_1 -frequency and the average compactness of the two stars in the binary. Interestingly, this relation appears to be universal, that is, essentially valid for all EOSs and masses, and could therefore provide a powerful tool to set tight constraints on the EOS [219, 305]. Indeed, an analytic expression was suggested in Ref. [219] to express the f_1 frequency via a third-order polynomial of the (average) stellar compactness, which reproduces reasonably well the numerical results. In addition to the correlations described above, Takami et al. [219, 267] also discussed additional correlations (24 in all), some of which had been already presented in the literature, e.g., in Refs. [160, 218], and some of which are presented there for the first time. Examples of these correlations are reported in Fig. 10 and refer to the f_{max} , f_1 and f_2 frequencies and the physical quantities of the binary system, e.g., the average compactness \bar{M}/\bar{R} , the average density $(\bar{M}/\bar{R}^3)^{1/2}$, the pseudo-average rest-mass density $(\bar{M}/R_{\text{max}}^3)^{1/2}$, or the dimensionless tidal deformability $(\lambda/\bar{M}^5)^{1/5}$ (cf., also Fig. 15 of Ref. [219]). In confirmation of the accuracy of the computed frequencies, very similar values for the f_1 frequencies were also found by Dietrich et al. [299] in a distinct work aimed at determining the impact that conservative mesh-refinement techniques have on the accuracy of the post-merger dynamics.

Even though the toy model proposed by Takami et al. [219] provides a simple and convincing explanation of the power associated to the f_1 frequency peak, alternative interpretations of the low-frequency part of the PSD have also been suggested. More specifically, Bauswein et al. [298] claimed that the lower-frequency peak (i.e., the f_1 peak in Refs. [74, 219, 267]) is actually made of two separate peaks originating from different processes. One of these peaks is said to be produced by a nonlinear combination between the dominant quadrupolar oscillation (f_{peak} or f_2) and the

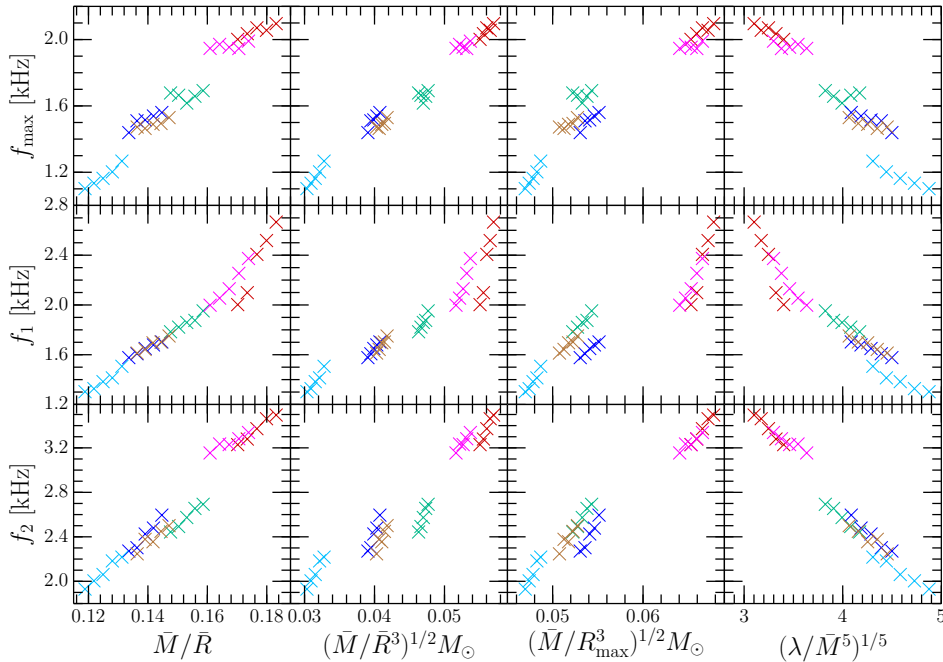


FIG. 10. Empirical correlations between the f_{\max} , f_1 and f_2 frequencies and the physical quantities of the binary system. [Reprinted with permission from Ref. [219]. © (2015) by the American Physical Society.]

quasi-radial oscillation of the remnant and is named f_{20} [208], while the other is said to be caused by a strong deformation initiated at the time of the merger, the pattern of which then rotates (in the inertial frame) slower than the inner cores of the remnant and lasts for a few rotational periods, while diminishing in amplitude. The gravitational-wave emission associated with this motion then powers a peak that was named f_{spiral} in Ref. [298]. The connection between the f_{spiral} peak and the deformation was supported by showing that only PSDs computed from time intervals of the gravitational waveform that contain the deformation have the f_{spiral} peak. It was also claimed that the f_{spiral} peak can be roughly reproduced in a toy model, where two bulges orbit as point particles around the central double-core structure for a duration of few milliseconds, but no details were given in Ref. [298].

In their analysis, Bauswein et al. [298] also proposed an explanation for the low-frequency modulations seen in quantities like the lapse function at the stellar center, the maximum rest-mass density, and the separation between the two cores of the remnant. Such quantities are modulated according to the orientation of the antipodal bulges of the deformation with respect to the double central cores: the compactness is smaller, the central lapse function larger, and the gravitational-wave amplitude maximal when the bulges and the cores are aligned, and viceversa.

Making use of a large set of simulations, Bauswein et al. [298] were able to obtain empirical relations for both types of low-frequency peaks in terms of the compactness of nonrotating individual neutron stars. Different relations, however, were found for different sequences of constant total mass of the binary, in contrast with what found in Takami et al. [219, 267], where a different definition for the low-frequency peak was used. As discussed by Bauswein et al. [298], the different behaviour

could be due to the fact that the results of Takami et al. [219, 267] were based on a limited set of five EOSs of soft or moderate stiffness (with corresponding maximum masses of nonrotating neutron stars only up to $2.2 M_{\odot}$), as well as on different chosen mass ranges for each EOS with a spread of only $0.2 M_{\odot}$ in the total mass of the binary. In Bauswein et al. [298], on the other hand, ten EOSs (including stiff EOSs with maximum masses reaching up to $2.8 M_{\odot}$) and a larger mass range of $2.4 - 3.0 M_{\odot}$ were used. Overall, the differences between the results of the two groups are significant only for very low-mass neutron stars (i.e., $M = 1.2 M_{\odot}$), which Takami et al. [219, 267] had not included in their sample because of the low statistical incidence they are thought to have (see also below).

One important consideration to bear in mind is that measuring the f_{spiral} frequencies through the motion of matter asymmetries via gauge-dependent quantities such as the rest-mass density is essentially impossible in genuine numerical-relativity calculations. This is because the spatial gauge conditions can easily distort the coordinate appearance of mass distributions and even the trajectories of the two stars during the inspiral (see Appendix A 2 of Ref. [32] for some dramatic examples). In an attempt to clarify the different interpretations suggested in Refs. [219, 298, 305] and to bring under a unified framework the spectral properties of the post-merger gravitational-wave signal, Rezzolla and Takami [303] have recently presented a comprehensive analysis of the gravitational-wave signal emitted during the inspiral, merger and post-merger of 56 neutron-star binaries [303]. This sample of binaries, arguably the largest studied to date with realistic EOSs, spans across five different nuclear-physics EOSs and seven mass values, including the very low-mass binaries (e.g., with individual neutron-star masses of $1.2 M_{\odot}$) that were suggested by Ref. [298] to be lacking in the previous analysis of Ref. [219]. After a systematic analysis of the complete sample, it was possible to sharpen a number of arguments on the spectral properties of the post-merger gravitational-wave signal. Overall it has found that: (i) for binaries with individual stellar masses differing no more than 20%, the frequency at the maximum of the gravitational-wave amplitude is related quasi-universally with the tidal deformability of the two stars; (ii) the spectral properties vary during the post-merger phase, with a transient phase lasting a few milliseconds after the merger and followed by a quasi-stationary phase; (iii) when distinguishing the spectral peaks between these two phases, a number of ambiguities in the identification of the peaks disappear, leaving a simple and robust picture; (iv) using properly identified frequencies, quasi-universal relations are found between the spectral features and the properties of the neutron stars; (v) for the most salient peaks analytic fitting functions can be obtained in terms of the stellar tidal deformability or compactness. Overall, the analysis of Rezzolla and Takami [303] supports the idea that the EOS of nuclear matter can be constrained tightly when a signal in gravitational waves from BNSs is detected.

An interesting extension of the work of Takami et al. [219, 267] was suggested by Bernuzzi et al. [268], who expressed the correlation between the peak frequencies f_2 with the tidal coupling constant κ_2^T instead of the tidal deformability parameter Λ , as done in Refs. [219, 267]. As found in previous works by Bernuzzi et al. [159, 218] (see Sect. V A), the dimensionless gravitational-wave frequency depends on the stellar EOS, binary mass, and mass ratio only through the tidal coupling constants κ_2^T and thus this is a better choice of parameter, also because it can be extended more straightforwardly to the case of unequal-mass binaries. The relation $f_2(\kappa_2^T)$ was found in Ref. [268] to be very weakly dependent on the binary total mass, mass ratio, EOS, and thermal effects (through the ideal-fluid index Γ_{th}). Relevant dependence on the stellar spins was instead found. This is shown in Fig. 11, which reports the dimensionless frequency Mf_2 as a function of the tidal coupling constant κ_2^T . Each panel shows the same data set; the colour code in each panel indicates the different values of binary mass (top left), EOS (top right), mass-ratio (bottom left), and Γ_{th} (bottom right). The black solid line is the fit obtained by Bernuzzi et al. [268], while the grey area marks the 95% confidence range.

Although not explicitly stated, all of the considerations made so far about the spectral properties

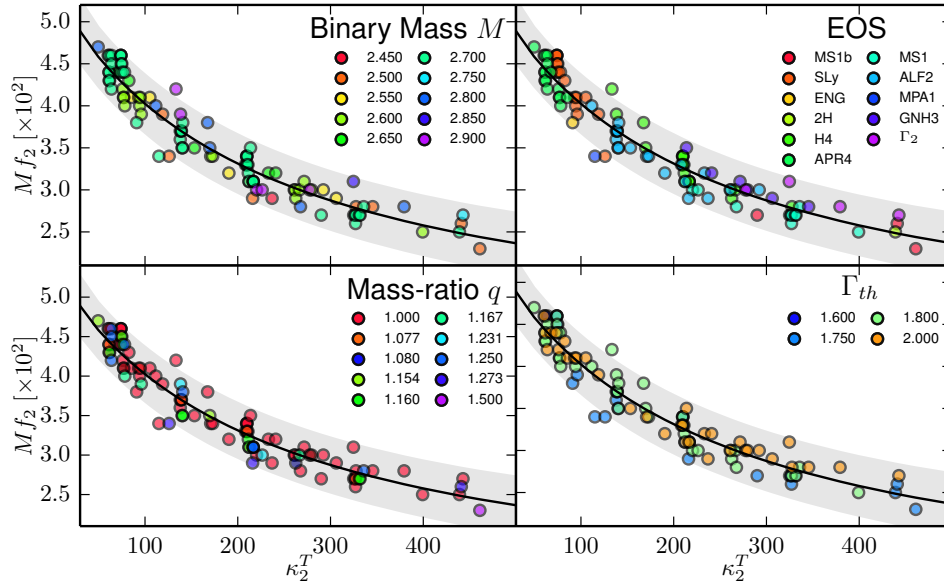


FIG. 11. Dimensionless frequency (Mf_2) as a function of the tidal coupling constant κ_2^T . Each panel shows the same data set; the colour code in each panel indicates the different values of binary mass (top left), EOS (top right), mass-ratio (bottom left), and Γ_{th} (bottom right). The black solid line is the fit, while the grey area marks the 95% confidence interval. [Reprinted with permission from Ref. [268]. © (2015) by the American Physical Society.]

of the post-merger signal refer to binaries that are initially irrotational. It is therefore natural to ask how does the dynamics change, both qualitatively and quantitatively, when spinning binaries are considered (a discussion on the modifications of the post-merger dynamics introduced by magnetic fields will be discussed in Sect. VIA 2). This was done in part by Bernuzzi et al. [250] and by Kastaun and Galeazzi [74]. The first work considered in particular whether the main-peak frequency f_2 is influenced by the initial state of rotation and found that this is indeed the case at least for very rapidly rotating neutron stars, suggesting that spin effects may be more important than found by Ref. [295]. Kastaun and Galeazzi [74], on the other hand, analysed the spectral changes induced by the initial spin and showed that the low-frequency peak f_1 is due to the gravitational-wave signal during the plunge and the first bounces. They also studied in detail the Fourier decomposition of the rest-mass density of the binary-merger product and its rotational profile, which is important for determining its lifetime, especially in view of the amplification of the magnetic field. A problem that needed to be tackled in their analysis is that of potential gauge artefacts. We recall, in fact, that rest-mass density distributions are gauge-dependent quantities and even when the system approaches an axisymmetric state after the merger, the spatial coordinates may not reflect this, because the gauge conditions employed in the evolution introduce local and global deformations. In order to exclude such systematic gauge effects, Kastaun and Galeazzi [74] introduced a different coordinate system, used just for post-processing. In this new coordinate system, they found that, the Fourier decomposition is far more regular than in the coordinate system normally used in the evolution. Furthermore, they showed that, contrary to common assumptions, the binary-merger product law of differential rotation consists of a slowly rotating core with an extended and massive envelope rotating

close to Keplerian velocity. The latter result has been confirmed recently also for the binary-merger product produced by the merger of unequal-mass magnetised binaries [306].

Before concluding this discussion on the post-merger gravitational-wave signal we should also make two important remarks. The first one is that gravitational-wave measurements at the expected frequencies and amplitudes are very difficult, namely limited to sources within ~ 20 Mpc. This number can be easily estimated with back-of-the-envelope calculations, but it was confirmed through detailed analysis of the detectability of the dominant oscillation frequency in Ref. [297] via a large-scale Monte Carlo study in which simulated post-merger gravitational-wave signals are injected into realistic detector data that matches the design goals of Advanced LIGO and Advanced Virgo. The second consideration to bear in mind is that the post-merger frequencies evolve in time, albeit only slightly. Hence, the spectral properties of the gravitational-wave signal can be asserted reliably only when the signal-to-noise ratio is sufficiently strong so that even these changes in time can be measured in the evolution of the PSDs [285, 289, 305, 307].

In light of these considerations, the prospects for high-frequency searches for the post-merger signal are limited to rare nearby events. Yet, if such detections happen, the error in the estimate of the neutron star radius will be of the order of a few hundred metres [297, 308].

3. *Black-hole–torus system*

As mentioned a number of times already, the collapse of the binary-merger product is expected to lead quite generically to the formation of a black-hole–torus system, with the black hole having a dimensionless spin of $J/M^2 \sim 0.7 - 0.8$ and the torus a mass of $\gtrsim 10^{-3} M_\odot$. An accurate determination of the final spin produced in the merger of BNSs is not a mere academic question as the rapid rotation of the black hole is a key ingredient in all of the models in which the BNS merger is thought to lead to a jet formation and a SGRB [39, 309, 310]. Because the energetics of the emission will depend sensitively on the black-hole spin, an accurate measure of the maximum value attainable can help set upper limits on the efficiency of the process. In view of this, Kastaun et al. [184] have focused on the accurate computation of the spin of the black hole originated in BNS mergers. Their initial data consisted of irrotational equal-mass binaries to which various amounts of rotation (parallel to the orbital angular momentum) are added to increase the total angular momentum (see Sect. IV). Although the initial data violated the constraint equations, the use of the constraint-damping CCZ4 formulation (see Sect. III B) yielded evolutions with violations smaller than those with irrotational initial data and non-constraint-damping formulations.

Overall, Kastaun et al. [184] found that a limit of $J/M^2 \approx 0.89$ exists for the dimensionless spin of the black hole and that any additional angular momentum present in the binary ends up in the torus rather than in the black hole, thus providing also another nontrivial example supporting the cosmic censorship hypothesis. The material in the torus will eventually be accreted onto the black hole, transferring angular momentum and further increasing the black-hole spin. However, this will happen on dissipative time scales which are longer and thus not relevant for the central engine of gamma-ray bursts, which should be ignited on a dynamical time scale after the merger.

4. *Spectral properties and the mass-redshift degeneracy*

Besides providing information on the EOS, the spectral properties of the gravitational-wave post-merger signal can also be used in a completely different manner, namely, to remove the degeneracy in the determination of redshift and mass for cosmological investigations. Indeed, a well-known problem of the detection of gravitational waves from compact-object binaries at cosmological distances

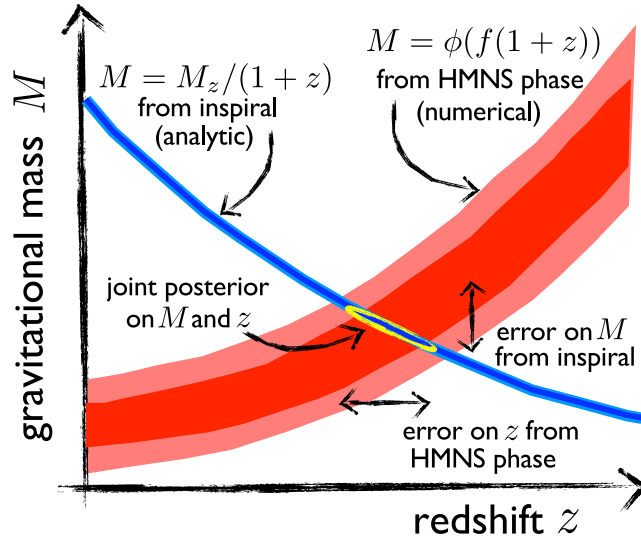


FIG. 12. A cartoon illustrating how the mass-redshift degeneracy is broken through the use of information from the inspiral and HMNS stages of a BNS merger event. Cross-correlating the information on the redshifted mass as a function of the redshift (blue stripe) with the information from the spectral properties of the HMNS phase (red stripe) will provide a localised range in mass and redshift, breaking the degeneracy. [Reprinted with permission from Ref. [244]. © (2014) by the American Physical Society.]

is the so-called “mass-redshift degeneracy”. More precisely, given a source of (gravitational) mass M at a cosmological redshift z , a direct gravitational-wave observation provides information only on the combined quantity $M(1+z)$, so that it is not possible to have an independent measurement of M and of z . The standard solution to this problem is to detect an electromagnetic counterpart to the gravitational-wave signal, so as to measure z and hence the mass M . While this is still possible, it may be not easy in the case of BNSs, as the electromagnetic counterpart, may not be directed towards us if in the form of the collimated jet of a SGRB.

In a recent investigation, Messenger et al. [244] described how this degeneracy can be broken when exploiting information on the spectral properties of the post-merger gravitational-wave signal. More specifically, making use of numerically generated BNS waveforms, it was shown that it is possible to construct frequency-domain power-spectrum reference templates that capture the evolution of two of the primary spectral features in the post-merger stage of the waveforms as a function of the total gravitational mass.

This is summarised via a cartoon in Fig. 12, which shows how the information on the redshifted mass as a function of the redshift (blue stripe) can be correlated with complementary information from the spectral properties of the HMNS phase. The overlap will provide a localised range in mass and redshift, breaking the degeneracy. A Bayesian inference method was then used to test the ability of the Einstein Telescope [291] to measure the characteristic frequencies in the post-merger stage of the signal, finding that redshift and gravitational mass can be determined separately, with uncertainties in the redshift of sources at $z = 0.01 - 0.04$ of 10% – 20% and in the gravitational mass of $< 1\%$ in all cases (see also Sect. VA for a method to determine the redshift based on tidal deformation in the inspiral of BNS systems).

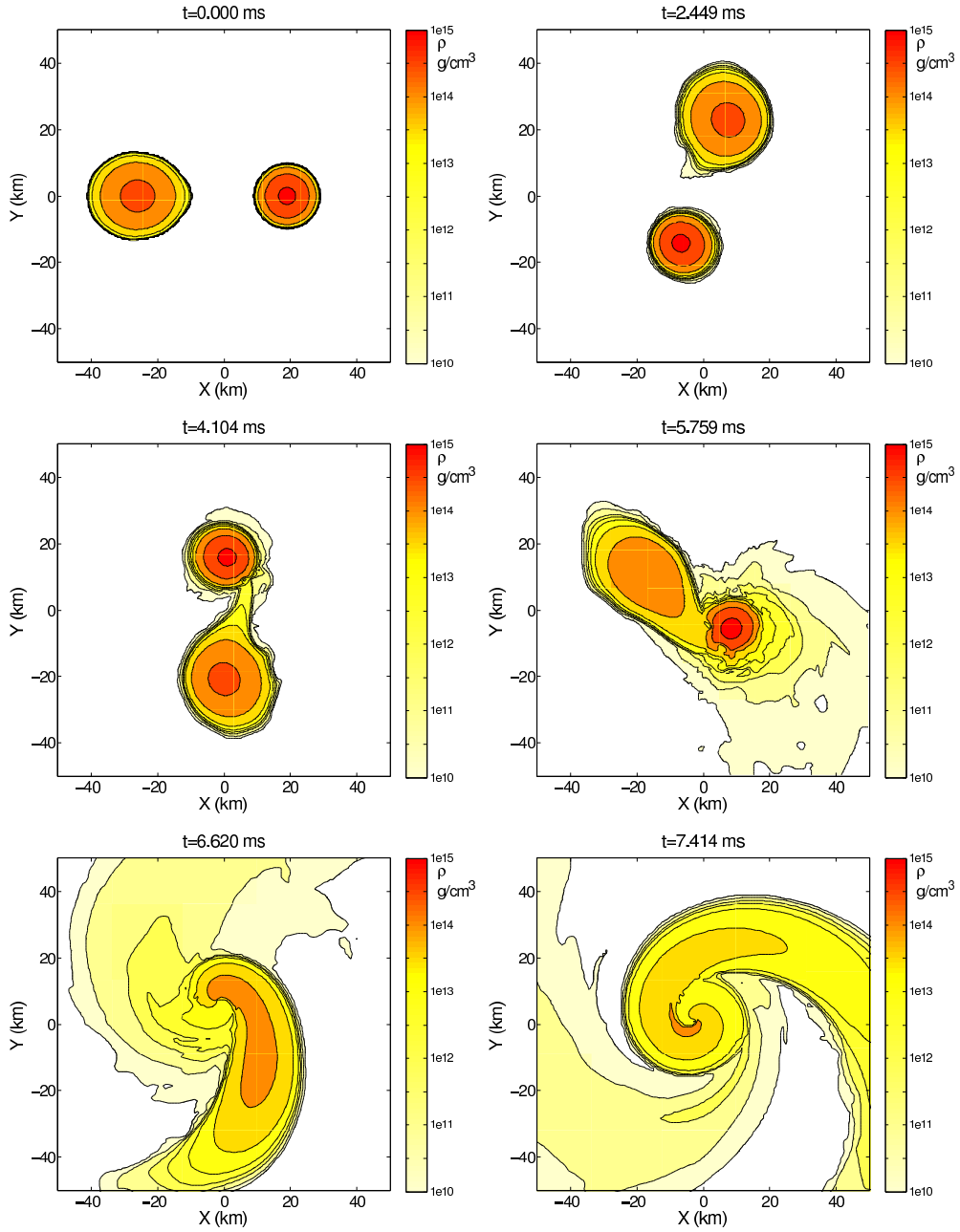


FIG. 13. Isodensity contours in the (x, y) plane for the inspiral and merger of a binary with mass ratio $q = 0.7$ and total gravitational mass $M_{\text{tot}} = 3.07 M_{\odot}$. The third frame shows the onset of the merger and the last two frames show the behaviour of the system during the collapse to a black hole. [From Ref. [58] © IOP Publishing. Reproduced with permission. All rights reserved.]

C. Unequal-mass binaries

Neutron stars in binaries are expected to be produced mostly with masses that are very similar to each other and thus with mass ratios in the range $q := M_B/M_A \in [0.7 - 1.0]$ [177]; although the number of observed BNS systems is rather limited with only a dozen of known systems [311], the mass-ratio distribution is peaked around $q \simeq 0.9 - 0.95$. Although these mass differences may appear small and indeed are so when comparing with the mass ratios expected for binaries of stellar-mass black holes and even more of supermassive black holes, these mass asymmetries are sufficient to produce significantly different dynamics.

The first general-relativistic investigations of unequal-mass BNS systems were performed in Refs. [58, 199], although these systems have been studied also earlier in various approximations (see, e.g., Refs. [312, 313]). A representative example of the dynamics of an unequal-mass binary with an ideal-fluid EOS is shown in Fig. 13, which shows isodensity contours in the equatorial plane for the inspiral and merger of a binary with a mass ratio $q = M_B/M_A = 0.7$ and a total gravitational mass $M_{\text{tot}} = M_B + M_A = 3.07 M_\odot$. During the inspiral phase, the heavier and more compact star is only slightly affected by its companion, whereas the latter is decompressed rapidly while being accreted onto the heavier star (see the three intermediate panels of Fig. 13).

In addition to a different dynamics during the inspiral, unequal-mass mergers also lead to substantial differences in the tori formed after the merger and surrounding the black hole. More specifically, while equal-mass mergers produce a highly symmetric disc, unequal-mass mergers produce initially asymmetric discs, because of the presence of a large spiral arm. The tidal disruption of the smaller-mass neutron star results in an extended tail (extending well beyond the domain shown in Fig. 13), which, unlike what happens in the equal-mass case, transfers angular momentum outwards very efficiently.

There has been a lot of research on general-relativistic simulations of the black-hole–torus system emerging from BNS mergers of unequal-mass binaries. Kiuchi et al. [314] tried to schematise the relation between the possible formation process of the central engine of SGRBs (namely a system composed of a black hole surrounded by a disc) and the gravitational waveforms that it generated. In particular, it was pointed out that the gravitational-wave spectra of different models are all qualitatively similar and that the various features of such spectra are connected qualitatively with the different phases of the merger (e.g., the transition between a merged object with two separate density maxima, reminiscent of the individual stars, and a merged object with a single density maximum; or the formation of spiral arms; or the ringdown of the black hole). It was also found that the torus mass has a positive correlation with the frequency of the highest peak in the spectra, with the total mass, and with the mass ratio.

More quantitative estimates of the disc mass and spin were given by Rezzolla et al. [58], who also measured recoil velocities of the black hole. In case of unequal-mass mergers, in fact, the formed black hole may recoil as a result of the asymmetrical emission of gravitational radiation in the final stages of the inspiral. Velocities of $\lesssim 100 \text{ km s}^{-1}$, much smaller than those observed in black hole simulations (see, e.g., [315–317]), were calculated. Yet, such a recoil could yield astrophysically interesting results, being comparable to or larger than the escape velocity from the core of a globular cluster, that is, $v_{\text{esc}} \sim 50 \text{ km s}^{-1}$ [318].

Using the results of numerous simulations and some simple physical considerations, Rezzolla et al. [58] also built a phenomenological expression that reproduces reasonably well the mass distribution of tori produced in the merger of unequal-mass binaries, i.e.,

$$M_{b,\text{tor}} = [c_1(1 - q) + c_2][c_3(1 + q)M_{\text{TOV}} - M_{\text{tot}}], \quad (47)$$

where M_{tot} and M_{TOV} are the gravitational mass of the binary and the maximum mass for an isolated neutron star with the same EOS, respectively. The coefficients $c_1 = 2.974 \pm 3.366$, $c_2 = 0.11851 \pm$

0.07192, and $c_3 = 1.1193 \pm 0.1579$ were determined by fitting equation (47) to the results of the fully general-relativistic simulations of Refs. [32] and [58], but rescaled to allow for a value of $M_{\text{TOV}} = 2.20 M_{\odot}$ to be more consistent with current observations of neutron star masses¹⁸. We expect that the values of the coefficients will depend on the EOS considered (in [58] a simple ideal-fluid EOS with $\Gamma = 2$ was used), but also that the functional dependence suggested in (47) will be the same for all EOSs.

Overall, expression (47) indicates that: (i) the mass of the torus increases with the asymmetry in the mass ratio; (ii) such an increase is not monotonic and for sufficiently small mass ratios the tidal disruption leads to tori that have a smaller mass for binaries with the same total mass; (iii) tori with masses up to $\sim 0.35 M_{\odot}$ are possible for mass ratios $q \sim 0.75 - 0.85$. This information has also been used to derive a relation between observations of the energy emitted by SGRBs and the mass of BNSs that produce the tori that are presumed to feed them [319]. In particular, after comparing the masses of the tori with the results of the simulations it was possible to infer the properties of the binary progenitors that yield SGRBs. By assuming a constant efficiency in converting torus mass into jet energy, (i.e., an efficiency of $\sim 10\%$), it was found that most of the tori would have masses smaller than $0.01 M_{\odot}$, favouring “high-mass” binary NSs mergers, i.e., binaries with total masses $\gtrsim 1.5$ times the maximum mass of an isolated NS. This has important consequences for the gravitational-wave signals that may be detected in association with SGRBs, since “high-mass” systems do not form a long-lived HMNS after the merger. Furthermore, the analysis carried out by Giacomazzo et al. [319] suggested that although binary systems comprising a black hole and a neutron star cannot be excluded as the engine of at least some of the SGRBs, the black hole would need to have an initial dimensionless spin of $J/M^2 \sim 0.9$, or higher.

A more recent analysis has been carried out by Dietrich et al. [299], who have presented results of a systematic investigation of unequal-mass binaries using four different nuclear-physics EOSs and significantly different stellar masses, i.e., with $q \simeq 0.66 - 0.86$. The binary with very small ratio is probably at the edge of what is realistic to expect from an astrophysical scenario, but is a useful reference to explore the dynamics of these systems in the most extreme conditions. Indeed, for $q \simeq 0.66$ and a stiff EOS, the secondary star is highly deformed during the inspiral, and its tidal disruption ejects substantial amounts of unbound matter, i.e., $0.03 M_{\odot}$, which could have a significant impact on the subsequent nucleosynthesis (cf., Sect. VIC). Also quite large is the mass of the torus produced around the black hole, which has been measured to be $\sim 0.3 M_{\odot}$ and that would obviously lead to a powerful electromagnetic counterpart

A number of very recent works have considered unequal-mass binaries as complementary cases within more systematic investigations, such as those involving microphysical nuclear EOSs and neutrino effects [320, 321], the spectral properties of the post-merger signal [303] or the influence of magnetic fields [306]. In general, it was found that the results do not differ considerably from the equal-mass binary simulations of the same kind as long as the difference in the masses is 10% or less. One aspect that may show larger differences is the composition of the ejecta [321].

D. Dynamically captured binaries

Dynamical-capture compact-object binaries are binaries that form through the close interaction (i.e., “collision”) of compact objects, as opposed to the more standard compact-object binaries, whose components were originally in the binary, *before* becoming compact objects. Recent studies

¹⁸ For completeness we also recall the coefficients originally reported in [58], that are: $c_1 = 1.115 \pm 1.090$, $c_2 = 0.039 \pm 0.023$, $c_3 = 1.139 \pm 0.149$.

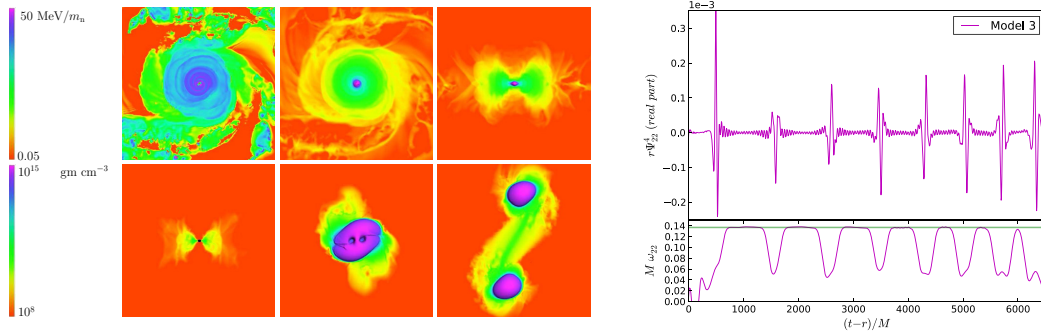


FIG. 14. *Left panel*: Snapshots of thermal specific energy (top left sub-panel) and rest-mass density (other five sub-panels). The top left and top middle, and bottom middle and bottom right sub-panels show the equatorial plane, while the other two show a perpendicular plane through the center of mass. The top sub-panels show an HMNS with surrounding disc and unbound material. The bottom sub-panels show, from left to right, a black hole and a surrounding disc; neutron stars with excited f-mode perturbations after a close encounter. The first four sub-panels have the same distance scale, where the coordinate radius of the HMNS and black hole are ≈ 13 and ≈ 6 km, respectively. The last two sub-panels share a second distance scale; the coordinate separation between the NSs in the last panel is ≈ 73 km. [Adapted from Ref. [148] with permission by the authors.] *Right panel*: Real part of the waveform (upper panel) and instantaneous gravitational wave frequency (lower panel) as a function of retarded time, for a model of Ref. [149] that shows several elliptical orbits. [Reprinted with permission from Ref. [149]. © (2012) by the American Physical Society.]

have suggested that there may be a significant population of compact-object binaries formed via dynamical captures in dense stellar environments [5–7], such as globular clusters. These binaries could contribute to the observed SGRB rate, even if it is difficult to quantify what fraction of SGRBs may be attributed to them [322].

Dynamically formed binary systems are born at small orbital separations and with large eccentricities, so that their orbits are likely to remain eccentric up to merger, since circularisation due to gravitational-wave emission requires longer timescales. As a result, their close orbital dynamics and gravitational-wave signal may differ substantially from those of standard BNS systems in quasi-circular orbits. Initially, dynamically formed binary systems may produce at periastron a series of well-separated, repeated gravitational-wave bursts that last for minutes to days (see right panel of Fig. 14). This sequence of bursts gradually transforms into the final chirp inspiral signal of an eccentric binary system.

Although the integrated energy released in gravitational waves is comparable to that of a quasi-circular inspiral, it will be more difficult to measure it in the advanced interferometric detectors that are coming into operation because a larger part of the radiation from dynamical-capture binaries is emitted at the close periastron and at rather high frequencies, which are mostly outside the best sensitivity range of the detectors [322].

As for the matter dynamics, each close encounter may launch a tidal tail and the neutron stars may be spun up to rotation frequencies close to breakup. The final remnant is then, like in the standard merger case, a compact object surrounded by a disc, but the disc is more likely to be externally fed by the tidal tails that are produced at each close encounter. A good fraction of the disrupted mass that orbits at some distance from the merged object is still gravitationally bound and will fall back on the central remnant on timescales substantially exceeding the dynamical timescale of the central object, but within seconds at most. Some snapshots of a simulation are reproduced from Ref. [148]

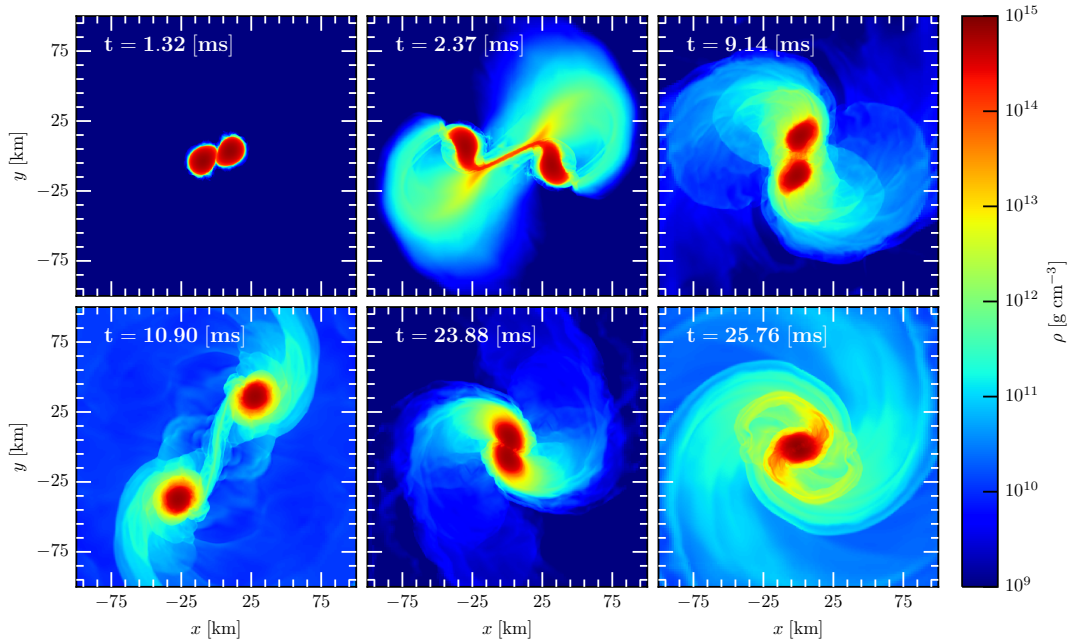


FIG. 15. Rest-mass density in the orbital plane for a parabolic-encounter simulation at six different times. The neutron stars undergo three close encounters before merging. The panels show snapshots of the two stars immediately before and after each encounter. Tidal torques at the periastron result in large mass ejection and trigger oscillations in the neutron stars. [Adapted from Fig. 1 of Ref. [72] with permission of authors.]

in the left panel of Fig. 14.

Newtonian calculations of eccentric binaries were performed long ago [146, 147], but general-relativistic simulations appeared in the literature only in 2012, with the work of Gold et al. [149]. One important result of the Newtonian studies [147] is that the eccentric orbits lead to tidal interactions that can excite oscillations of the stars. Such oscillations, in turn, generate an additional and characteristic gravitational-wave signal. In some cases, the gravitational signal can be dominated by these non-orbital contributions.

The general-relativistic simulations Gold et al. [149] started from initial-data sets created by superposing two boosted nonrotating equal-mass stars without solving the constraint equations. They found, however, that the constraint violation was at the level of the truncation error of the evolution scheme. The gravitational-wave signal computed in Ref. [149] (and reproduced in the right panel of Fig. 14) was obviously much more accurate than that from Newtonian calculations and was indeed interpreted as produced by oscillations of the individual stars that are tidally induced by the companion. Such a clear signal from orbit-induced stellar oscillations could be a very interesting source for third-generation gravitational-wave detectors such as the Einstein Telescope [291], but not for second-generation ones (except for very nearby events), because of the high frequency and short duration of the merger or of the quasi-periodic signals from the HMNS.

Although they employed a simple polytropic EOS with $\Gamma = 2$, Gold et al. [149] also pointed out that the neutron-star crusts may disrupt or fracture during the inspiral under such strong tidal deformations. This point was later put in evidence also by East and Pretorius [148], who performed improved general-relativistic simulations that included initial data produced by solving the constraint equations for colliding neutron stars (with equal and unequal masses) with a given impact parameter

and piecewise polytropic EOS models [217]. It was then shown that dynamical-capture mergers can produce accretion discs with masses $\lesssim 0.1 M_{\odot}$ and eject unbound material of up to a few percent of a solar mass.

Indeed, the copious ejection of matter is one of the aspects of the dynamics of dynamically captured binaries that makes them particularly interesting. Later on, in Sect. VIC, we will discuss in more detail the work done in this context and will also review the impact that the ejected material has on the electromagnetic signal and on the nucleosynthesis. However, it is worth mentioning here three works that represent in many respects the state of the art in the modelling of dynamically captured BNSs. The first one is by Rosswog et al. [150], who studied dynamical-capture binaries with a code that treats gravity in a Newtonian fashion but that treats microphysics (neutrinos, radioactive decay) in very sophisticated ways. In addition to finding results similar to the ones in Refs. [148, 149] for the bulk dynamics and for the amount of ejected material, Rosswog et al. [150] also computed neutrino luminosities from dynamical collisions and found them to be at least comparable to those from the merger of BNSs in quasi-circular orbits. The second work is by Radice et al. [72], which is more recent and has considered the dynamics of BNSs in parabolic orbits in full general relativity, with high-order numerical methods and with different treatments of the radiative effects. It was then found that eccentric binaries can eject significantly more material than quasi-circular binaries and that the outflow is composed of a combination of tidally- and shock-driven ejecta, mostly distributed over a broad $\sim 60^{\circ}$ angle from the orbital plane, and, to a lesser extent, by thermally driven winds at high latitudes [72]. Ejecta from such eccentric mergers were also found to be more neutron rich than those of quasi-circular mergers. This is due to the strong tidal torques exerted on the neutron stars during their periastron passages and that lead to the ejection of cold, neutron-rich material. The third work is by East et al. [71] and focused on the influence of the initial spin of the neutron stars in eccentric orbits. It was found that even moderate spins can significantly increase the amount of ejected material, including the amount unbound with velocities greater than half the speed of light. This would predict brighter electromagnetic signatures (cf. Sect. VIC).

The dynamics of a representative parabolic-encounter simulation from Ref. [72] is shown in Fig. 15, where the rest-mass density is shown in the orbital plane at representative times during the evolution before and after each close encounter. During the periastron passage strong tidal torques and shocks result in episodic outflow events. Part of the ejected neutron-rich matter is unbound from the system, while the rest settles in a thick atmosphere around the neutron stars.

VI. BEYOND PURE HYDRODYNAMIC SIMULATIONS

A. Ideal and resistive magnetohydrodynamics simulations

Very strong magnetic fields¹⁹, in the range of $10^{12} - 10^{15}$ G, are known to endow neutron stars. In addition to modifying the dynamics of the matter, such strong magnetic fields are likely related to observable electromagnetic emissions (see Sect. VIA 3), which will yield important information on these systems when observed through the electromagnetic counterparts they can lead to. We should note that hereafter we will make the distinction between “*prompt*” electromagnetic counterparts and “*delayed*” electromagnetic counterparts, or “*afterglows*”. The former is expected to take place in a window in time that starts just before (i.e., a few seconds) the merger and ends a few hours after the merger, while the latter is instead expected to take place from days to years after the actual merger. Hence, while we discuss prompt electromagnetic counterparts in Sections VIA 1, VIA 2, and VIA 3, we will discuss delayed electromagnetic counterparts in Section VIC.

Although neutron stars can in principle be endowed with very large magnetic fields, in practice, such large fields are not expected to be present in old neutron stars right before merger, as they must have decayed considerably, reaching values that are instead in the range i.e., $10^8 - 10^{10}$ G. Yet, even comparatively weak initial magnetic fields are expected to be amplified during and after the merger through different mechanisms and instabilities, which have received particular attention over the years. In particular, five different and quite general amplification mechanisms have been so far explored with BNS mergers: (i) magnetic compression; (ii) turbulent amplification, (iii) the Kelvin-Helmholtz instability (KHI), either at the merger or later on in the dynamics [41] (cf., Sect. V); (iv) magnetic winding by differential rotation; (v) the magneto-rotational instability (MRI) [325–328] in the binary-merger product and/or the massive disc around it or around the black hole after the collapse has taken place.

In view of the considerations above, the inclusion of magnetic fields in simulations of BNS mergers, although far from being trivial, is a necessity, and a number of codes have been developed to solve the equations of relativistic ideal MHD (IMHD; see Sect. III F). While several of the codes adopt a fixed curved background spacetime (see, e.g., Refs. [121, 329–335]), considerable development has also been made with codes that can handle arbitrary and dynamical spacetimes (see, e.g., Refs. [122, 123, 336–339]). In addition, an effort has been dedicated to going beyond IMHD and thus to including resistive effects as a way to better model resistive contributions to the energy losses from the system. The importance of resistivity effects can be easily deduced from observing the evolution of a current sheet in high but finite conductivity. Under these conditions, several instabilities can take place in the plasma and release substantial amounts of energy via magnetic reconnection [340]. Because the study of reconnection in relativistic phenomena is important to try to explain the origin of flares in relativistic sources, it is not surprising then that several groups have developed in recent years numerical codes to solve the equations of special and general-relativistic RMHD [38, 41, 118–120, 341–348].

Among the instabilities expected to develop, the KHI and MRI in particular are those that give the fastest, exponential growths, and therefore particular attention has been concentrated on them. In contrast to the KHI, where a numerical triggering is necessary when dealing with inviscid fluids [349], the MRI develops also in inviscid plasmas, but requires the highest grid resolutions to be

¹⁹ Quantum electrodynamics effects may become important and would need to be accounted for if the magnetic fields are sufficiently strong and the rest-mass density sufficiently low. For example, the so-called Landau quantisation (see, e.g., Ref. [323]) may occur if the magnetic fields exceed a critical value of $B_{\text{crit}} = 4.414 \times 10^{13}$ G and the rest-mass density is below a critical value $\rho_{\text{crit,B}} = 7.04 \times 10^{10} (0.1/Y_e) (B/10^{16} \text{G})^{3/2} \text{g/cm}^3$, where Y_e is the electron fraction per baryon. Kiuchi et al. [324] have concluded that Landau quantisation is not important during the merger of magnetised BNSs because the regions where the QED limit is exceeded are at rest-mass densities above the critical one. Other effects have not been investigated and are routinely neglected in general-relativistic MHD simulations.

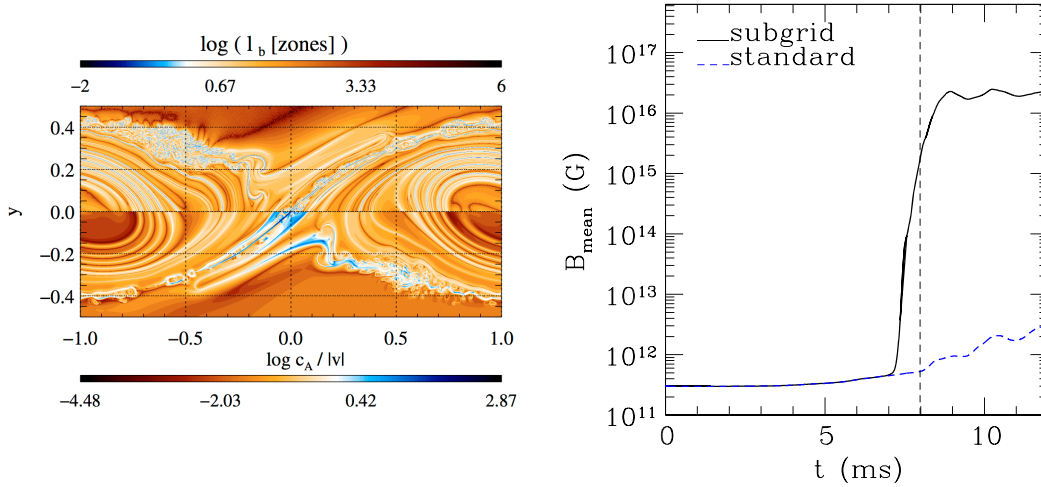


FIG. 16. *Left panel:* Snapshot of the structure of a model studied in Ref. [353], taken shortly after the termination of the kinematic amplification phase. The top half shows the logarithm of the characteristic length scale of the magnetic field in units of the zone size. The bottom half shows the logarithm of the ratio of the Alfvén velocity and the modulus of the fluid velocity, bluish and reddish colours denoting strongly and weakly magnetized regions, respectively. [Reproduced with permission from [353]. © ESO.] *Right panel:* Evolution of the mean value of the magnetic field when a subgrid model is implemented (black solid line) and when it is not (blue dashed line). The vertical dashed line shows the time of merger (when the neutron-star cores collide). In the simulation implementing the subgrid model the magnetic field grows by five orders of magnitude up to $\sim 10^{16}$ G and saturates when reaching equipartition with the kinetic energy of the fluid in the turbulent regions. In the simulation without the subgrid model the magnetic field grows by only one order of magnitude. [Reprinted with permission from Ref. [351]. © (2015) by the American Physical Society.]

resolved for realistic magnetic-field strengths, and so is effectively the most difficult to investigate. Local simulations with sufficient resolutions are possible, as nicely displayed in the left panel of Fig. 16, which shows a snapshot of a developed KHI, but it is believed that in the near future computational resources will not be sufficient to study the MRI quantitatively in BNS merger simulations, despite some impressively expensive attempts having been made [65, 350]. As a result, current attempts are moving towards the use of models of the magnetic-field amplification at the subgrid level [351, 352], as done in other research fields where turbulent flows need to be modeled. In practice, these approaches aim at including the contribution to the bulk flow from the unresolved turbulent dynamics by introducing suitably tuned corrections to the equations (most notably the induction equation). Subgrid approaches make computationally feasible the inclusion of effects that are prohibitively expensive to be included via direct simulations, but the results they provide are dependent on the choice made for the subgrid dynamics. Therefore, although subgrid modelling appears the only convincing way to proceed in the near future, computations based on direct simulations under reasonably realistic conditions or first-principle studies of the properties of relativistic turbulence (see, e.g., [353–356]) are definitively still very important.

In addition to the challenges related to the abundance of physical instabilities, IMHD and RMHD simulations are also made difficult by the necessity of conserving during the evolution the divergence-free condition of the magnetic field. This is an obvious requirement to avoid the spurious generation of magnetic monopoles which would act as energy sinks, but is particularly challenging

to enforce when adopting mesh-refined grids. This issue has been addressed in general-relativistic MHD simulations mainly in three ways: (i) through the “*constrained transport*” approach [357–361]; (ii) through the “*hyperbolic divergence cleaning*” method [362]; (iii) through the use of the vector potential as evolution variable in place of the magnetic field [205, 363–365]. While we refer to Ref. [359] for a more detailed review of these methods, we here simply recall that the constraint-transport approach preserves the constraint to machine accuracy but requires special interpolation at refinement-level boundaries in order to preserve the constraint. Hyperbolic divergence cleaning, on the other hand, may require a tuning of the parameters it uses to damp-out any violation of the constraints and hence its efficiency is problem dependent but generally worse than the constraint transport approach. Finally, the vector-potential formulation is the one that seems to work best in AMR, since the constraint is preserved by construction with the vector potential, even though problems may arise with the restriction and prolongation operations of AMR grids. Overall, the last two approaches, although not optimal, are easier to implement and hence have become the standard choice in many general-relativistic IMHD and RMHD codes.

1. *Inspiral and merger dynamics*

As in the case of pure-hydrodynamics simulations, also in IMHD, the study of the inspiral phase is the simplest to calculate as no instabilities are expected to develop and hence has been the focus of the early calculations. Furthermore, given that the inspiral may be the only part of the signal that can be detected by present gravitational-wave detectors for sources that have a small signal-to-noise ratio, it is natural to ask whether the detection of the inspiral can be used to measure the strength of the magnetic field in the neutron stars prior to the merger. The answer to this question can be easily worked out analytically and it is not difficult to conclude that, for realistic initial magnetic fields (i.e., $B_0 \lesssim 10^{10}$ G) the magnetic energy in the two stars is several orders of magnitude smaller than the binding energy of the binary and hence magnetic fields can only provide very small corrections to the orbital dynamics. While correct, this estimate does not address the problem of whether an advanced detector would be able to measure such a small correction.

Hence, a number of groups have undertaken the task of providing a quantitative answer to this question by measuring the orbital corrections induced in BNS systems with variable magnetic-field strengths [34, 69, 205, 366]. A common feature of these simulations is that they all employed very simplified EOSs (i.e., an ideal-fluid EOS with $\Gamma = 2$) and all used fully buried magnetic fields that were added to the pure hydrodynamical solutions of irrotational binaries. More specifically, since no self-consistent solution was (and still is!) available for magnetized binaries, a poloidal magnetic field was added a posteriori using a suitable prescription for the vector potential. The disappointing, but not surprising, answer coming from these simulations is that for realistic magnetic-field strengths the changes introduced in the inspiral waveforms are too small to be detected by present and possibly future detectors such as the Einstein Telescope [205, 366]. On the other hand, if unexpectedly high magnetic fields, i.e., $B_0 \gtrsim 10^{10}$ G are present in the stars before the merger, these would leave a sufficiently strong imprint to be detected [366].

To reach these conclusions, Giacomazzo et al. [366] have computed the overlap, \mathcal{O} , between the waveforms produced during the inspiral by magnetized and unmagnetized binaries, finding that for initial magnetic-field strength $B_0 \lesssim 10^{14}$ G the overlap during the inspiral is $\mathcal{O} \gtrsim 0.999$ and is quite insensitive to the mass of the neutron stars. Only for unrealistically large magnetic fields like $B_0 \simeq 10^{17}$ G, the overlap does decrease noticeably, becoming $\mathcal{O} \lesssim 0.76$ (0.67) for stars with rest-mass masses $M_b \simeq 1.4$ (1.6) M_\odot , respectively. On the other hand, in agreement with what found by Refs. [34, 69], Giacomazzo et al. [205] also find that magnetic fields do have an impact after the merger. Some representative waveforms of BNS systems with different masses and magnetic-field

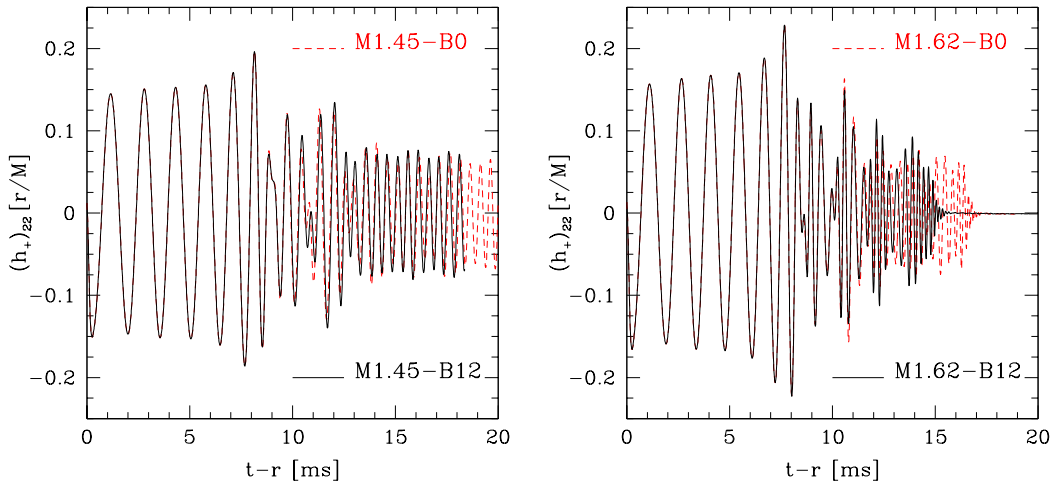


FIG. 17. Gravitational waves for a low-mass (individual stellar rest mass $1.445M_{\odot}$) binary (left panel) and a high-mass (individual stellar rest mass $1.625M_{\odot}$) binaries (right panel) as a function of the retarded time $t - r$ in ms. Shown with red dashed lines are the corresponding models with zero magnetisation. Note that the differences become appreciable only after the merger. [Reprinted with permission from Ref. [205]. © (2011) by the American Physical Society.]

strengths are shown in Fig. 17, which displays the waveforms for a low-mass (left panel) and a high-mass binary (right panel) as a function of the retarded time. Shown with red dashed lines are the corresponding models with zero magnetisation. It is clear how the black and red lines become discernible only after the merger.

Already the early works on the inspiral and merger of magnetised BNSs, e.g., Refs. [34, 69, 205, 366], pointed out that the KHI develops at the beginning of the merger in the shear layer where the two stars enter into contact, causing an amplification of the magnetic-field strength. Because these works used rather coarse spatial resolutions, the highest being that of Ref. [205], 220 m on the finest grid, the amplification reached was rather modest: of one order of magnitude at most [205]. Hence, it was not possible to confirm the results of Price and Rosswog [204] and assess whether a KHI fully develops at the merger.

However, simulations with very high resolution were carried out by Kiuchi et al. [65], who used the code already employed and tested in Refs. [367, 368]. With a grid spacing of 70 m on the finest grid and an evolution time of ~ 100 ms, these computations were the most accurate and computationally expensive simulations of magnetised BNS mergers, but have been further improved in even more recent (and expensive) simulations by Kiuchi et al. [324], where an impressive resolution of only 17.5 m on the finest grid was used. In both works [65, 324], the simulations used a nuclear-physics EOS (i.e., the stiff EOS H4 [369], which is based on relativistic mean field theory with hyperon effects). The study of the various amplification mechanisms observed in these simulations confirmed and improved previous results. In particular, the development of the KHI was studied with great care and, thanks to the high resolution employed, Kiuchi et al. [65, 324] were able to show that the amplification factor depends on the grid resolution but not on the initial magnetic-field strength [39, 205, 353]; this is nicely summarised in the left panel of Fig. 18, which shows that the growth rate actually scales inversely with resolution [324]. The figure also shows a divergent behaviour,

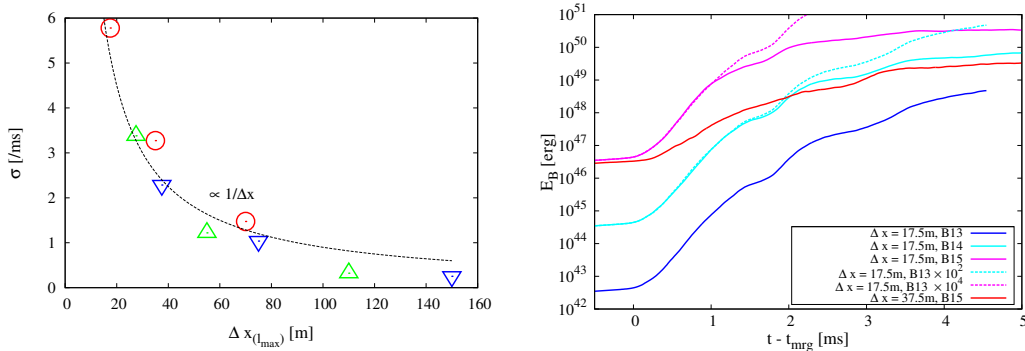


FIG. 18. *Left panel:* Growth rate of the magnetic-field energy as a function of the final grid resolution. *Right panel:* Evolution of the magnetic-field energy for a number of different simulations with different initial magnetic fields (see legend). The cyan and magenta dashed curves show the evolution when the initial magnetic field of $B_0 \sim 10^{13}$ G has been magnified by a factor of 10^2 and 10^4 , respectively. [Reprinted with permission from Ref. [324]. © (2015) by the American Physical Society.]

so that even with resolutions one order of magnitude higher than other groups, Kiuchi et al. [324] were not able to observe the saturation that is however expected to take place under more realistic conditions. This behavior can be understood in terms of the basic properties of the KHI, whose cut-off wavenumber can only increase with grid resolution unless some other cut-off is introduced by other physical processes, e.g., via viscosity or resistivity. These results seem to suggest that, unless a better microphysical treatment is introduced, e.g., through a realistic treatment of viscosity and resistivity, even resolutions orders of magnitude higher than those commonly used nowadays may be insufficient to capture the realistic development of the KHI in magnetised BNS mergers.

Another important aspect explored by the simulations of Kiuchi et al. [324, 367] is that of the amplification of the magnetic field once the KHI has fully developed. This is reported in the right panel of Fig. 18, which shows the evolution of the magnetic-field energy for a number of different simulations with different initial magnetic fields (see legend). The cyan and magenta dashed curves show the evolution when the initial magnetic field of $B_0 \sim 10^{13}$ G has been magnified by a factor of 10^2 and 10^4 , respectively. The data refers to the simulations reported in Ref. [324] and shows that amplifications in the magnetic field of about three orders of magnitude are possible; these results also show how the amplification of the magnetic field in such direct simulations depends sensitively on the grid resolution, since Kiuchi et al. [65] found a much smaller amplification (of one order of magnitude only) when employing a resolution of 70 m.

In summary, despite the computationally impressive efforts carried out recently by Kiuchi et al. [65, 324], the issue of the final amplification of the magnetic field as a result of the development of the KHI at the merger of magnetised BNS systems remains open. It is clear that the magnetic-field energy is amplified by at least about three orders of magnitude after the merger and also that the saturation energy of the magnetic-field is likely to be $\gtrsim 0.1\%$ of the bulk kinetic energy, i.e., $\gtrsim 4 \times 10^{50}$ erg. It is yet unclear, however, whether these results will continue to hold if one considered lower but more realistic initial magnetic field, e.g., $B_0 \sim 10^8 - 10^{10}$ G, and whether the newly produced magnetic-field energy can actually saturate near equipartition. We should however remark that, albeit almost prohibitively expensive, such direct simulations are essential, since they can provide the correct physical input for the subgrid modelling that may be necessary for less expensive simulations investigating large parameter spaces.

Exploring a computationally less expensive approach to the development of the KHI and hence to the amplification of the magnetic fields at the merger, Giacomazzo et al. [351] were the first to study magnetic-field amplification in the KHI via a subgrid model for the magnetic-field amplification. The resolution on the finest grid was about 225 m, but they introduced a subgrid model that served to include within global direct simulations some effects of the small-scale amplification of the magnetic field caused by turbulence. More in detail, this subgrid model was intended to account for the electromotive forces arising from unresolved fluctuations in the magnetic field and bulk fluid velocity. The magnetic field evolution was modified according to the strength of the fluid vorticity, the rest-mass density and the original magnetic field, and tuning the magnitude of the magnification through the results of high-resolution local special-relativistic simulations of driven relativistic MHD turbulence made by Zrake et al. [370]. Among other results, Giacomazzo et al. [351] found that the magnetic field reaches saturation very rapidly after the merger (cf. the right panel of Fig. 16), with different resolutions giving the same amplification. While this is the first time that a similar result has been obtained in BNS simulations, it is also a natural consequence of the recipe adopted for the subgrid modelling, which effectively quenches the magnetic-field growth at equipartition.

In a series of recent works, Neilsen et al. [206] and Palenzuela et al. [352] have described simulations from a code that implements general-relativistic MHD with tabulated EOSs and a neutrino leakage scheme to account for cooling via neutrino emission²⁰. The resolution of the finest grid was of 460 m in Ref. [206] and of 230 m in Ref. [352], which also adopted a subgrid modelling of the magnetic field in terms of the fluid vorticity. Overall, these works confirmed that the effects of the magnetic field and of neutrino production and cooling play a subleading role in the dynamics of the binary during the inspiral, and that during the merger the magnetic field strength can increase to $10^{15} - 10^{16}$ G through compression, the KHI and turbulent amplification.

A distinct, but equally interesting series of studies about the inspiral part of magnetized BNS simulations has been focusing on the interaction of the stellar magnetospheres just before the merger, exploring whether the resulting electromagnetic radiation can represent a counterpart to the gravitational-wave emission. A number of mechanisms have been suggested in this regard [38, 347], e.g., the interaction with the interstellar medium in the form of synchrotron radio emission, the emission of flares induced by resonant excitations of neutron-star modes by tides that could induce crust cracking, and unipolar induction [371], the extraction of stellar kinetic energy through the interaction of the stellar magnetosphere with an external magnetic field. This last process can be modeled as a perfect conductor moving through an ambient magnetic field, which induces a charge separation on its surface and drives electrical currents. The kinetic energy from the moving conductor is extracted in the form of MHD waves propagating along the magnetic field lines, or of particle acceleration as in ordinary pulsars. In terms of simulations, a systematic investigation has been carried out by Palenzuela et al. [38, 347], who studied in RMHD the electromagnetic emission originating a few orbits before the merger of a BNS²¹. By using the Poynting flux as a first approximation to the energetics, Palenzuela et al. [38, 347] found that the emitted power can outshine pulsars in binaries, that it displays a distinctive angular- and time-dependent pattern, and that it radiates within large opening angles. These properties suggest that some BNS mergers could yield interesting prompt electromagnetic counterparts to gravitational-wave events, although the comparatively low luminosity of $\sim 10^{40} - 10^{42}$ erg/s and the large error box of gravitational-wave detectors would make the identification rather challenging.

The systematic work of Refs. [38, 347] was completed in a follow-up analysis [372], where the same group studied the dependence of the electromagnetic luminosity on the inclination of the dipolar magnetic fields relative to the orbital plane; in principle, the dipoles are expected to be arbitrarily

²⁰ A more complete discussion of results about neutrino emission will be presented more in detail in Sect. VIB.

²¹ Although with an admittedly coarse resolution of about 300 m, the system was also followed up to a few milliseconds after the merger, thus including the dynamics of the magnetic fields during the formation of the HMNS.

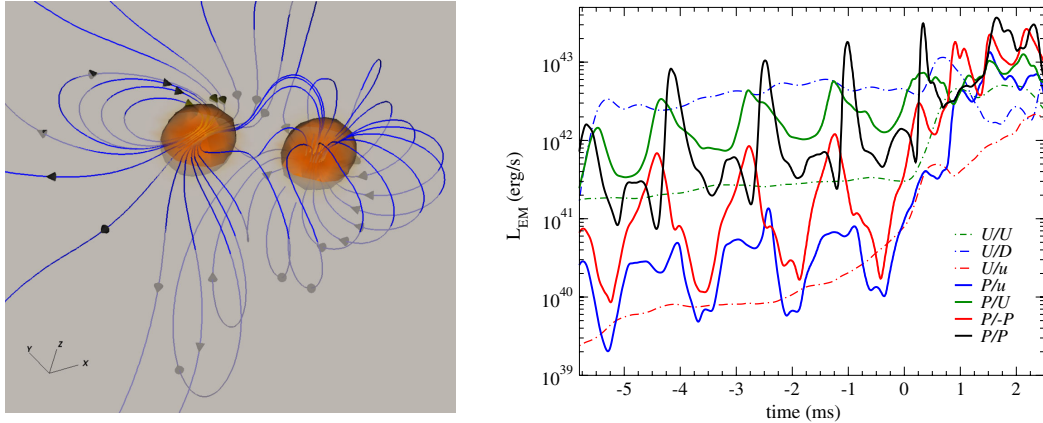


FIG. 19. *Left panel:* Three-dimensional arrangement of magnetic-field lines, roughly 3 ms before merger, for an evolution starting with one star having a dipole magnetic field perpendicular to the orbital angular momentum and the other having it parallel (the “ P/U case” in the nomenclature of Ref. [348]). The orbital plane was made translucent (displayed in grey) to aid in distinguishing sections of the field lines lying above from those below the $z = 0$ plane (the latter in less vivid colours). Notice that field lines naturally venture off the orbital plane. *Right panel:* Luminosities for different magnetic-dipole configurations in a binary neutron-star system, shifted in time so that $t = 0$ denotes first contact between the stars. Solid lines refer to configurations studied in Ref. [348], dot-dashed lines to those studied in Refs. [38, 347]. The legend refers to the initial alignment of the initial dipole magnetic field of each star in the binary: U means parallel to the orbital angular momentum, u means parallel to the orbital angular momentum but with a smaller intensity, D means antiparallel to the orbital angular momentum, P means perpendicular to the orbital angular momentum. [Reprinted with permission from Ref. [348]. © (2014) by the American Physical Society.]

oriented, while they were assumed perpendicular to the orbital plane in the previous works. In this way it was pointed out that indeed there is a strong dependence on the dipole orientations, as it can be seen in the right panel of Fig. 19. This dependence can be linked to the reconnection and redistribution of the magnetic field (the shape of the magnetic-field lines can become rather complex, as shown in the left panel of Fig. 19) as the stars interact. In particular, the luminosities are roughly periodic, accompanied by an overall increase as the orbit tightens, and the local maxima of the luminosity occur when the magnetic fields emanating from each star reconnect. The Poynting flux was found to be not strongly collimated and thus producing isotropic emissions. Finally, as we will further discuss in Sect. VIII, Ponce et al. [372] also examined whether the characteristics of the electromagnetic counterparts can provide an independent way to test gravity in the strong regime. They found that in some cases the electromagnetic flux emitted by binaries in scalar-tensor theories may show small but potentially measurable deviations from the prediction of general relativity.

2. Post-merger dynamics: short-lived merger product and black-hole–torus system

We now shift to describing the progress of MHD simulations relative to the post-merger phase when the binary-merger product is short lived. We recall that we define the binary-merger product as whatever object is produced after the merger, bearing in mind that this object can actually change its nature over time. In fact, depending on the total mass and mass ratio of the binary, the EOS, and the

time after the merger, this can be a *stable* object, i.e., a black hole or a neutron star, or a *metastable* object that will eventually reach, on timescales that can be much larger than the dynamical timescale, one of the two stable states mentioned above. In the phase in which the binary-merger product is a metastable object (if this phase exists at all), the binary-merger product will either be an SMNS (i.e., a uniformly rotating star with mass above the maximum mass for nonrotating star M_{TOV} , but below the maximum mass for uniformly rotating stars M_{max} , with $M_{\text{max}} \simeq 1.20 M_{\text{TOV}}$ [60]), or an HMNS (i.e., a differentially rotating star more massive than an SMNS). When talking about a *short/long-lived* binary-merger product we refer only to the metastable phase of the binary-merger product before its collapse to black hole, hence considering whether the metastable object lives for a *short* or *long* time before collapsing to a black hole. In this Section, in particular, we will concentrate on those scenarios where the progenitors neutron stars have masses sufficiently large so that the binary-merger product collapses rather rapidly (i.e., within ~ 1 s) to a rotating black hole, producing a black-hole–torus system (see Sect. VIA 3 for a discussion of long-lived binary-merger products).

Before dwelling on the details of this section, it may be useful to remark right at the outset that simulating this stage of the binary evolution is particularly challenging and possibly the most difficult aspect of the simulation of merging BNSs. This is because after the merger convergence order of any known numerical method reduces to one or less, while ultra-high accuracy is needed to resolve those MHD instabilities as the MRI that are supposed to play a crucial role. It will probably be difficult to resolve such instabilities in current and near-future simulations. Important additional factors that make post-merger simulations more challenging are related to both missing physical input, such as accurate neutrino treatment, and numerical issues, such as the dependence of the HMNS lifetime on the grid resolution, the AMR grid setup, the boundary location and conditions, and the unresolved numerical resistivity.

The first, pioneering works in IMHD, reported in Refs. [34, 69, 366], which used extremely high and unrealistic initial magnetic fields of $B_0 = 10^{15} - 10^{17}$ G, explored the effects that magnetic fields have on the lifetime of the HMNS created after the merger. Later on, Giacomazzo et al. [205] reported a study with more realistic initial magnetic fields and pointed out that the amplified magnetic field in the HMNS can redistribute the angular momentum, transporting it outwards and reducing the amount of differential rotation that is essential in supporting the HMNS against gravitational collapse. As a result, if the magnetic tension is sufficiently strong to be comparable to or larger than the matter pressure gradients (i.e., $B_0 \gtrsim 10^8$ G), magnetic fields can contribute to causing the collapse of the HMNS [59, 205]. For larger initial magnetic fields (i.e., $B_0 \sim 10^{12} - 10^{17}$ G), however, the amplified magnetic fields will also introduce a significant magnetic pressure, which provides additional pressure support and thus either compensates or even dominates the angular-momentum redistribution, with an overall delay of the collapse [205].

The study of Giacomazzo et al. [205] was then improved by Rezzolla et al. [39], whose analysis of the post-merger evolution was extended to much longer times, thus providing the first evidence of the connection between the merger of magnetized BNSs and SGRBs (see also Sect. VB). In particular, it was shown for the first time that, after black-hole formation, a poloidal component of the magnetic field around the black-hole rotation axis is generated in addition to the predominant toroidal component that persists in the accreting torus. Representative snapshots of the rest-mass density and of the magnetic-field lines are shown in Fig. 20. The low-matter-density “funnel” or “magnetic-jet” structure (i.e., a structure characterized by a large-scale ordered poloidal magnetic field along the black-hole spin axis) may be arguably connected to the launch of jets related to SGRBs, even if it should be remarked that *no ultrarelativistic outflow* was observed in the funnel produced in those simulations. An intense outflow of matter was instead seen from the torus and, in particular, in the regions that surround the magnetic jet. Within the IMHD approximation, this outflow was able to stretch the magnetic field lines and lead to the formation of the funnel with

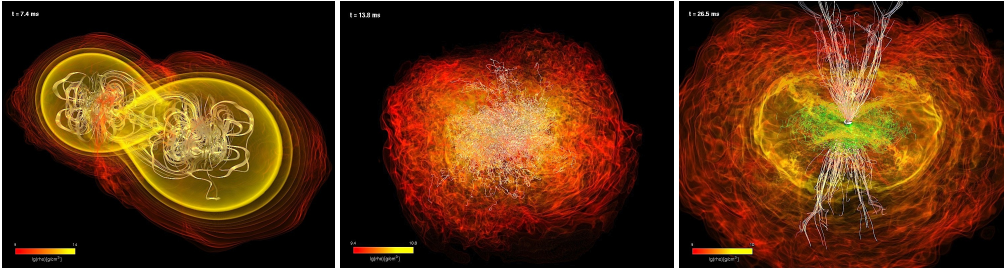


FIG. 20. Snapshots at representative times of the evolution of the binary and of the formation of a large-scale ordered magnetic field. Shown with a colour-code map is the rest-mass density, over which the magnetic-field lines are superposed. The panels refer to the binary during the merger ($t = 7.4$ ms), *before* the collapse to black hole ($t = 13.8$ ms), and *after* the formation of the black hole ($t = 26.5$ ms). Green lines sample the magnetic field in the torus and on the equatorial plane, while white lines show the magnetic field outside the torus and near the black-hole spin axis. The inner/outer part of the torus has a size of 90 to 170 km, while the horizon has a diameter of $\simeq 9$ km. [Adapted from Ref. [39] with permission by the authors.]

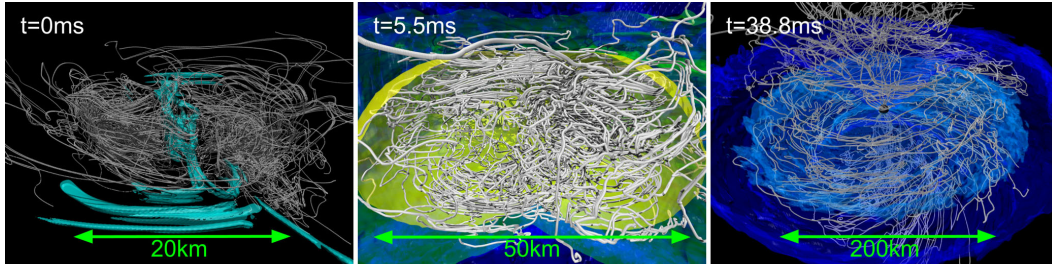


FIG. 21. Snapshots of the density, magnetic-field strength and magnetic-field lines. The left, middle, and right panels show the configuration just after the onset of the merger, during the HMNS phase, and when a black hole formed, surrounded by an accretion torus, respectively. In each panel, the white curves are the magnetic-field lines. In the left panel, the cyan colour represents magnetic fields stronger than $10^{15.6}$ G. In the middle panel, the yellow, green, and dark blue surfaces represent the density iso-surfaces of 10^{14} , 10^{12} , and 10^{10} g/cm³, respectively. In the right panel, the light and dark blue surfaces are the density iso-surfaces of $10^{10.5}$ and 10^{10} g/cm³, respectively. [Reprinted with permission from Ref. [65]. © (2014) by the American Physical Society.]

predominantly poloidal magnetic field.

In a related work, Aloy et al. [373], studied magnetic instabilities in BNS mergers comparing the results of two different numerical approaches: the above-mentioned global numerical simulations of Rezzolla et al. [39] and the local numerical simulations of Obergaulinger et al. [353], which can be run with numerical resolution much higher than that of global simulations and adequate to capture the fastest growing modes. While this is a very interesting approach, the results of Aloy et al. [373] found significant differences between local and global simulations. These could be due to a number of causes and primarily to the fact that the development of the MRI in BNSs may be influenced by the varying background flow that is produced by the colliding stellar cores and that cannot be reproduced in the local simulations.

The scenario of magnetic-field amplification in IMHD simulations has also been investigated with

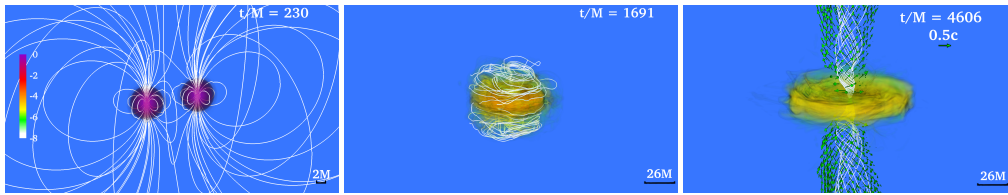


FIG. 22. Snapshots of the rest-mass density, normalized to its initial maximum value $\rho_{0,\max} = 5.9 \times 10^{14} \text{ g/cm}^3$ shown in a logarithmic scale at selected times. Arrows indicate plasma velocities, and white lines show the magnetic-field structure. [Adapted from Ref. [42] with permission by authors.]

the high-resolution simulations of Kiuchi et al. [65, 324], who describe in detail how the growth of the magnetic-field energy in the HMNS phase is attributable to nonaxisymmetric MRI in the low-density regions, while magnetic winding contributes to the growth of the toroidal magnetic-field energy as well. Figure 21 shows some representative snapshots of the rest-mass density and magnetic-field lines as obtained from the simulation of Ref. [65]. The last panel in particular seems to show the formation of a poloidal component, though not as clear as in the simulations [39]. The different behaviour may be due to the different EOSs employed in the simulations, or to the different visualisation of the magnetic-field lines. In particular, Kiuchi et al. [65] use a much stiffer EOS (H4 [369]), which leads to a smaller matter outflow and, consequently, to a weaker poloidal-field component; the latter, we recall, is generated by the motion of matter along the edges of the torus near the rotation axis since in IMHD the magnetic-field lines are advected by the fluid.

Indeed, the generation of a coherent poloidal magnetic field at late times was also observed in other simulations employing the ideal-fluid EOS, such as those of black-hole–neutron-star binaries of Etienne et al. [374] or, more recently, of Paschalidis et al. [40] for neutron-star–black-hole systems, and of Ruiz et al. [42] for BNS systems. Indeed, it is worth noting that the most recent work of Ruiz et al. [42] is very similar to the one by Rezzolla et al. [39] in terms of EOS and stellar properties, but uses higher initial magnetic fields and has a different treatment of the “atmosphere”, which could explain why, in addition to a coherent magnetic structure, Ruiz et al. [42] find that the funnel becomes magnetically dominated at the end, and are able to measure a sustained outflow (although only mildly relativistic). This is shown in the representative snapshots reported in Fig. 22.

Finally, as an additional confirmation of the robustness of the process, the formation of a coherent magnetic-jet structure was observed also in the work of Dionysopoulou et al. [41], who have evolved BNSs in RMHD (see discussion below); also in this latter case, however, only a magnetic structure was formed and no sustained ultra-relativistic outflow was observed²². Overall, the results of Refs. [39, 41, 42, 350] are interesting because they provide proof-of-principle evidence that the merger of magnetised BNSs could provide the basic physical processes necessary to explain the phenomenology invoked to explain the observations of SGRBs. Hence, they serve as a link between the theoretical modelling of BNSs and the observations of SGRBs; however only an electromagnetic counterpart to a BNS merger can cast this link on an undisputed ground.

Resistive MHD codes are harder to build and use because of the increased complexity of the equations, because of the additional difficulties posed by their numerical solution (the equations easily

²² It is presently unclear whether the jet acceleration mechanism is the result of some energy extraction from the accreting black hole, as in the Blandford-Znajek mechanism [375], or of some other acceleration mechanism, e.g., as in the Aloy-Rezzolla booster [376].

become stiff in regions of high conductivity), and because the choice of realistic values for the resistivity is far from trivial (see, e.g., [377]), as experiments and current astronomical observations do not set any stringent constraint on its values at the temperatures, rest-mass densities, and magnetic fields appearing in BNS mergers. The resistive MHD code `whiskyRMHD` of Dionysopoulou and collaborators [41] matches the highly conducting stellar interior to an electrovacuum exterior. This is different from and complementary to the approach of Refs. [38, 347, 348], in which the resistive description is matched to a force-free one in order to study the interaction of the two stellar magnetospheres before the merger (see Sect. VIA 3 for more details). This choice was made because the focus of Dionysopoulou et al. [41] was the dynamics of post-merger objects, which are surrounded by matter emitted through the large baryonic winds produced after the merger, and to ensure that in the low-density regions the electromagnetic fields behave as if in vacuum.

Using such a resistive code, Dionysopoulou et al. [41] performed a systematic comparison of the dynamics of equal-mass magnetized BNSs when simulated either in IMHD or in RMHD. One of the most important differences found is that, since in RMHD the magnetic field is not perfectly locked with the plasma, resistive simulations show a less efficient redistribution of the angular momentum in the HMNS. This, in turn, causes an increase in the lifetime of the HMNS. Another difference is that the modulus of the magnetic field along the rotation axis is about two orders of magnitude larger than in the IMHD simulation. This is due mainly to the intense currents produced by the rapidly rotating torus and also to the magnetic-field diffusion of the strong magnetic field in the torus across the walls of the funnel. As mentioned above, Dionysopoulou et al. [41], also confirmed the formation of a low-density funnel produced by a predominantly poloidal magnetic field along the black-hole rotation axis, although also in this case no ultra-relativistic outflow was observed in the simulation. The magnetic-jet structure that forms can be viewed as a quasi-stationary structure that confines the tenuous plasma in the funnel away from the dense plasma in the torus. However, the plasma in the funnel does not have sufficient internal energy to launch a relativistic outflow. It is also possible that reconnection processes or neutrino pair annihilation, not treated in their work, could generate the energy required for launching a relativistic outflow along the baryon-poor funnel. Two representative snapshots of these simulations are presented in Fig. 23, which displays large-scale two-dimensional views on the (x, z) planes of the magnetic field for an IMHD simulation (left panel) or an RMHD one (right panel). The snapshots refer to when a black hole has already formed. It should be noted that the formation of a magnetic-jet structure around the black-hole rotation axis extends on scales that are much larger than those of the accreting torus. Note also that in the RMHD case, the magnetic field shows a coherence on the largest scales of the system.

Finally, Dionysopoulou et al. [41] noted the potentially very interesting fact that a shearing boundary layer is present at the interface between the magnetic-jet structure and the torus. A KHI is expected to form there, but it was not investigated because of the insufficient resolution.

In summary, a number of simulations suggest that when the binary-merger product from the merger of magnetised BNSs collapses to a rotating black hole, the matter in the region along the rotation axis does not have much centrifugal support and accretes onto the black hole, leaving behind a funnel of low-density matter. Both in IMHD and in RMHD simulations, the magnetic fields in this region are stretched into a poloidal component, either because of the inflow onto the black hole, or because of the outflow along the torus edges, or both. While reasonable and fundamentally what is expected, many details of this picture still need to be cast on firmer grounds.

3. *Post-merger dynamics: long-lived merger product and extended X-ray emission*

We next shift to describing the progress of MHD simulations relative to the post-merger phase, concentrating on those scenarios in which the binary-merger product is long-lived (i.e., does not col-

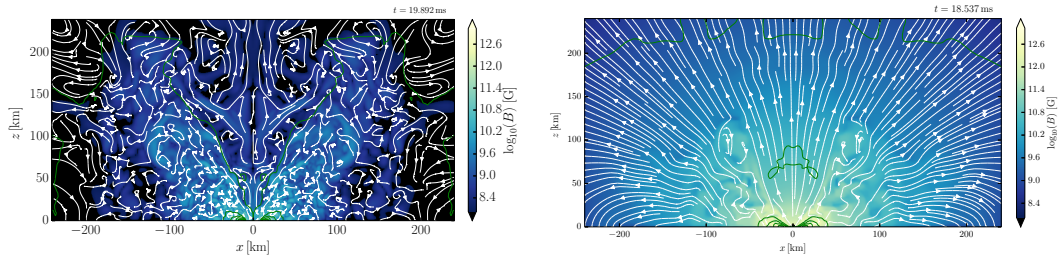


FIG. 23. Large-scale two-dimensional snapshots on the (x, z) planes of the magnetic field in the case of a simulation in IMHD (left panel) or RMHD (right panel). The snapshots refer to slightly different times but in both cases to when a black hole has already formed. Note again the formation of a magnetic-jet structure around the black-hole rotation axis, which extends on scales that are much larger than those of the accreting torus. Note also that in the RMHD case, the magnetic field shows a coherence on the largest scales of the system. [Reprinted with permission from Ref. [41]. © (2015) by the American Physical Society.]

lapse on a timescale of $\sim 10^3 - 10^4$ s) and could be used to explain otherwise puzzling astronomical observations. We recall, in fact, that the *Swift* satellite [378] has revealed phases of roughly constant luminosity in the X-ray afterglows of a large subclass of SGRBs (i.e., $\gtrsim 25\%$ of the full set of SGRBs). These are referred to as “X-ray plateaus” (see, e.g., Refs. [379, 380]) and last $10 - 10^4$ s. The riddle is then in the timescales involved, which are too long if the X-ray emission is really an afterglow. Making the standard assumption that the gamma-ray emission is associated to an ultra-relativistic jet launched by the black hole as it accretes matter from the torus and since the torus mass is $\lesssim 0.1 M_\odot$, with accretion rates $\sim 10^{-3} - 10^{-2} M_\odot \text{ms}^{-1}$ [58, 381], the accretion timescale is at most ~ 1 s. This is three or more orders of magnitude smaller than the observed timescale for the *sustained* X-ray emission.

A way out from this riddle is in principle available and involves the presence a long-lived “proto-magnetar”, that is, a uniformly rotating object formed in the merger that powers the X-ray emission through standard dipolar radiation and spin-down [346, 382–386]. By performing general-relativistic MHD simulations of BNS mergers, Giacomazzo et al. [387] showed for the first time that the end result of the merger may be a stable magnetar, surrounded by an extended disc. This result is not particularly surprising given that the total mass of the binary was chosen to be below the maximum mass of the corresponding nonrotating star, but it was nevertheless useful to remark that the violent dynamics at the merger is not sufficient to induce the collapse of a binary with a subcritical mass. Giacomazzo et al. [387] also estimated the proto-magnetar typical periods of the order of a few milliseconds, magnetic field strengths in the range $B \sim 10^{15} - 10^{16}$ G, and, under the assumption of energy loss by pure dipole radiation, luminosities of $\sim 10^{46} - 10^{49}$ erg/s. In a follow-up work, Dall’Osso et al. [388] studied the gravitational-wave emission from the proto-magnetars deformed because of the large magnetisation [389–391], finding, as expected, that such radiation is dependent on the EOS and yields a potential detection rate of $0.1 - 1 \text{ yr}^{-1}$ events with advanced detectors.

Although the formation of a proto-magnetar and its dipolar radiation can help explain the long timescale over which the sustained X-ray emission is observed in some SGRBs, it also introduces a different riddle. What is difficult to explain in this case is the timing of the gamma- and X-ray emissions. If the X-ray emission is produced by the binary-merger product, then it *cannot* follow the gamma-ray emission, which seems to require a jet and hence a black hole. Indeed, none of the simulations to date indicates the generation of a collimated jet by the binary-merger product [34, 38, 65, 204, 324, 351, 392], which instead appears after the formation of a black hole [39, 41, 42].

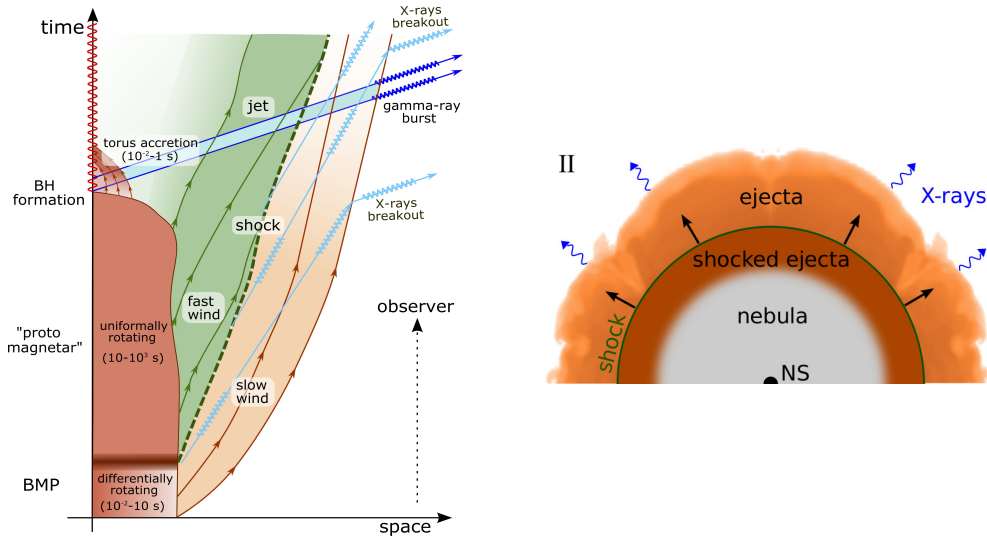


FIG. 24. *Left panel:* Schematic spacetime diagram showing in red the region occupied by the binary-merger product that eventually collapses leading to a black-hole–torus system. Shown in brown and green are the regions occupied by the magnetically driven slow wind and by the dipole-driven fast wind. The interaction of the two winds generates a shock and the sustained X-ray emission, while a jet is produced by the black-hole–torus system. [Reproduced from Ref. [75] with permission by authors.] *Right panel:* Schematic representation at a given time of the shock structure. [Reproduced from [393] with permission by authors.]

To resolve this riddle a scenario has been developed that involves a delay in the detection of the X-ray emission which is trapped in the material ejected after the merger. The scenario has been suggested simultaneously by two groups, i.e., as the “two-winds” scenario [75] or as the “time-reversal” scenario [393]; while both scenarios stem from initial joint discussions among the authors, they have been developed entirely independently and present slight differences²³. In what follows we concentrate on the former, but details on the latter can be found in Refs. [393].

The easiest way to describe this scenario is to discuss it via a spacetime diagram as the one shown in the left panel of Fig. 24. There, shown as red-shaded is the region occupied by the binary-merger product, which eventually collapses to produce a rapidly rotating black hole surrounded by an accreting torus. The binary-merger product is expected to rotate differentially for an Alfvén timescale, i.e., $\lesssim 1 - 10$ s and if it does not collapse to a black hole when differential rotation is lost, it rotates uniformly for considerably longer, i.e., $\lesssim 10^3 - 10^4$ s. Shown instead as brown-shaded is the region occupied by a *slow* and baryon-rich wind, whose geometry is approximately spherical and which moves at bulk speeds of $\sim 0.01 - 0.1 c$, then progressively slowing down as it loses part of its kinetic energy to climb out of the gravitational potential. There are a number of ways in which this wind can be driven, possibly all acting at the same time: via shock heating [381], via magnetic fields and differential rotation [261, 367, 394], or via neutrinos [395, 396]. In all cases, the duration of the slow wind is $\lesssim 1 - 10$ s, and in the first two scenarios the wind is isotropic for realistic magnetic-field

²³ More specifically, the model of Ref. [75], provides a detailed calculation of the resulting X-ray lightcurves and suggests as signature the presence of inverse-Compton scattered thermal cocoon photons that should show up at energies > 10 MeV with a luminosity $\sim 10^{50}$ erg/s. The model of Ref. [393], on the other hand, provides a more systematic analysis that the time delay between the prompt SGRB and the long-lasting X-ray signal can be large enough to explain the observed X-ray emission.

topologies [394].

Once differential rotation is lost, the magnetically driven wind is quenched and the uniformly rotating and magnetized binary-merger product will emit a *fast* and baryon-poor wind (green-shaded area) moving with bulk speeds of $\sim 0.3 - 0.5$. The binary-merger product can provide a continuous source of dipole radiation over a timescale set by the stability of the binary-merger product, i.e., $\sim 1 \text{ s} - 10^3 \text{ s}$.

Since the slow and fast winds have different velocities, the latter catches up with the former, producing a shock which heats the matter locally and leads to an X-ray emission. At the same time, because the matter of the slow wind is baryon rich and optically thick, the X-ray photons cannot propagate freely, but rather diffuse through the slow-wind material till reaching a photospheric radius from which they travel directly towards the observer. The effective speed of propagation of the X-ray photons is $\sim c/\tau$, where $\tau \gg 1$ is the optical depth of the slow wind where photons are produced, and the shock front moves through the wind with a relative speed of $\sim c/5$, therefore X-ray diffusion can be ignored until the shock is close to the photosphere. A snapshot of the expanded wind structure is shown in the right panel of Fig. 24 and is taken from Ref. [393].

As the X-ray photons “slowly” diffuse in the slow wind, the binary-merger product will spin down via dipolar emission to a sufficiently slow rate to collapse to a black hole surrounded by a hot dense torus²⁴. magnetic instabilities will develop in the torus, amplifying the magnetic field [39, 65] and leading to the construction of a jet-like magnetic structure [39, 41, 42]. This magnetic funnel can collimate the low-density material in its interior, which could be heated either by the neutrinos emitted from the torus [397], or via magnetic reconnection. In addition, the matter ejected with the slow wind can further confine the propagation of the jet [201, 398, 399]. As a result, an ultrarelativistic jet could be launched propagating with Lorentz factors $\Gamma \sim 100 - 1000$ (light-blue shaded area). Clearly, within this scenario the dynamics of the jet across the winds material is similar to the one envisaged for long GRBs, so that a burst of gamma rays is expected to be produced as the jet breaks out, with luminosities of $L \simeq 10^{50} - 10^{51} \text{ erg/s}$, over the timescale of the duration of the accreting torus, i.e., $0.01 - 1 \text{ s}$.

Although still largely qualitative, the two-winds/time-reversal models solve both the X-ray timescale riddle (the emission is produced by the binary-merger product, which can survive up to 10^4 s) and the timing riddle (the X- and gamma-ray emission are produced at different times, locations and propagate at different speeds). In order to reproduce self-consistently this scenario one would require numerical simulations on timescales of hours and these are still too expensive to be feasible, even in two dimensions. However, there are several observational features that can be used to confirm or rule out this novel paradigm. First, it is clear that the launching of the jet will take place considerably after the actual merger of the two neutron stars, which is also when the gravitational-wave amplitude reaches its first maximum. Hence, the observation of a SGRB which is seen to take place $10^3 - 10^4 \text{ s}$ after the maximum gravitational-wave emission would be a confirmation of the validity of this scenario for SGRBs with extended X-ray emission. Second, future observations could test this scenario by looking for inverse-Compton scattered thermal cocoon photons that should show up at energies $> 10 \text{ MeV}$ with a luminosity $\sim 10^{50} \text{ erg s}^{-1}$ lasting for about a second. Finally, the detection of an X-ray emission anticipating the SGRB, such as the precursor signals in some SGRBs [400] would also represent a strong validation of this model.

²⁴ As mentioned in Sect. II, it has been pointed out that the collapse of the uniformly rotating SMNS cannot lead to a torus surrounding the black hole as too little angular momentum is available in outer layers of the star [36]. At the same time, it has been noted that the binary-merger product prior to collapse is still expected to be surrounded by matter in quasi-Keplerian orbits, so that a torus is likely to be formed [75]. This conjecture has still to be proven via simulations.

B. Inclusion of radiative losses

Radiative effects, and in particular those associated with the emission of neutrinos, can influence significantly the evolution of the HMNS and the disc produced after the merger, and possibly play an important role in the mechanisms that generate SGRBs. We recall that before the merger, each neutron star can be considered “cold” (namely, such that the thermal energy of constituent nucleons is much smaller than the Fermi energy); at the merger, however, strong shocks are generated, which heat the merged stellar object up to temperatures of $\sim 30 - 50$ MeV. This increased internal energy can be lost very efficiently via copious emission of neutrinos, which may reach luminosities of the order of 10^{53} erg s $^{-1}$, which can be deposited along the baryon-free axis of rotation of the black hole via neutrino pair annihilation. This energy injection can therefore play an important role, or even be entirely responsible for powering the relativistic jets needed for the beamed emission of a SGRB [29, 309, 401] (see however Ref. [402] for a different conclusion). Neutrinos are also expected to play an important role in the ejection of matter from the merged object and such matter contributes to heavy-element generation and macronovae/kilonovae phenomena (see Sects. VIA 3 and VIC).

For all of these reasons, incorporating the energy and momentum losses via neutrinos in simulations of merging BNS is universally recognised as very important. Yet, a complete treatment of the microphysics of these systems would generally require solving the full transport problem (the Boltzmann equation, including the absorption, emission, and scattering source terms) in six dimensions (plus time): three for the spatial components and an additional three for the momentum components. Even if Shibata et al. [403] have derived a concise and general formulation for the conservative form (very important for numerical simulations, as mentioned in Sect. III E) of the Boltzmann equation in general relativity, such simulations are out of reach for current (and near-future) computational resources (except for one-dimensional simulations, like in Ref. [404]).

As a result, a number of approximations, either in the gravitational sector or in the radiation one, need to be adopted to make some progress. A simple and yet reasonably robust approach to approximate neutrino radiative losses is the so-called grey (energy-averaged) “leakage scheme”, which is essentially a parameterized neutrino cooling scheme. This scheme was initially developed by van Riper and Lattimer [405] and has been widely used for both core-collapse supernovae and BNS simulations [206, 396, 405–409]. Such schemes estimate only the local changes in the lepton number and the associated energy losses via neutrino emission, but this is probably sufficient when simulating the late stages of compact binary mergers, because they usually evolve on short timescales and thus the details of radiation transport are expected not to dominate the bulk dynamics of the system.

Furthermore, neutrino leakage schemes provide a good approximation at those rest-mass densities in which neutrinos are either mostly trapped or almost free streaming, namely at rest-mass densities larger than $\sim 10^{12}$ g/cm 3 and temperatures around ~ 10 MeV (neutrinos are trapped because their scattering off baryons is so efficient that they quickly reach a thermal equilibrium with the nuclear matter), or at rest-mass densities smaller than $\sim 10^{11}$ g/cm 3 and with energies below ~ 10 MeV (neutrinos in these regimes interact rarely with the nuclear matter and can therefore be considered as free streaming). Most of the matter in BNS systems before and in the early stages of the merger is in such ranges, while for matter outside those ranges interpolation between the two limiting regimes can be used.

Of course, also more sophisticated approaches to approximating the radiative transport in general-relativistic simulations have been proposed over the years. One of them is Thorne’s truncated moment formalism for radiation hydrodynamics [410–416], whose simplest implementation involves the evolution of the zeroth moment of the free-streaming neutrino distribution function on a set of individual radial rays (this is also referred to as the “M0” approach). Such a scheme is simpler than the two-moment grey method (“M1”) [300, 414, 417, 418] and, because it tracks both neu-

trino density and average energies, it allows one to model a number of important effects, such as gravitational redshift, velocity dependence and non local-thermodynamical equilibrium that cannot be easily incorporated into grey schemes. In this respect, the work of Sekiguchi et al. [321, 418], whose neutrino transport is computed in a leakage-based scheme [286, 419, 420] and incorporates Thorne’s moment formalism [410], can currently be considered the most sophisticated approaches to account for radiative losses in binary-merger simulations in general relativity, together with the M1 approach of Foucart et al. [300, 421].

Another approach developed recently is the spherical-harmonics method, based on an expansion of the radiation intensity in angles using spherical harmonics basis functions [356, 422]. Yet another example are the “ray-by-ray”, multi-energy-group neutrino schemes, like multigroup flux-limited diffusion and isotropic diffusion source approximation [423–427]. These schemes can offer a rather good approximation under many conditions, but they are still rather computationally expensive and have not yet been used in BNS simulations.

When discussing the actual applications of radiative-transfer schemes to BNS simulations, we should start by mentioning that the first ones were obviously made in Newtonian gravity, where neutrino leakage schemes were initially employed by Ruffert et al. [397, 406, 428, 429] and more recently by Rosswog et al. [407, 430], also with nuclear EOSs and magnetic fields. On the other hand, the first works in general relativity considering some form of neutrino cooling are those of Sekiguchi et al. [431] and have been followed by others [72, 206, 284–287, 320, 352, 409]. In addition to the general-relativistic hydrodynamics equations with realistic hot EOSs, these works generally solve also the evolution equations for the neutrino, electron, and the total lepton fractions per baryon, together with weak interaction processes and electron/positron capture.

Although the mathematical approaches for the inclusion of the radiative losses from BNS mergers, as well the numerical methods and their accuracies, vary considerably from simulation to simulation, over the last few years several groups [72, 206, 284–287, 320, 321, 352, 409, 418] obtained a number of results that do not depend on such “details” and can therefore be considered robust features of the radiative properties of BNS merger simulations. The first of such features is the fact the neutrino luminosity is high in the outer regions of the HMNS, in particular near the polar cap, where the rest-mass density is also relatively small. This is a result that supports the merger hypothesis for the engine of SGRB: pair annihilation of neutrinos and antineutrinos could supply the required amount of thermal energy necessary to drive a fireball along the rotation axis. This conclusion is in stark contrast with the recent work of Just et al. [402], who have considered the long-term evolution of the black-hole–torus system using a multi-energy group M1-type scheme for the neutrino transport. In particular, Just et al. [402] found that the neutrino emission of the accreting torus (which is also expanding because of viscous transport) is too short and too weak to yield the energy necessary for the outflows to break out from the surrounding ejecta shell as highly relativistic jets. While the work of Just et al. [402] explores in detail timescales that are considerably longer than those considered so far, it is also restricted to two spatial dimensions and, more importantly, is not fully general-relativistic. Because a number of examples have shown that the inclusion of general relativity is essential for a proper assessment of the energetics and efficiencies in black-hole processes, additional simulations in full general relativity are needed to assess whether or not BNS mergers can provide neutrino-powered jets.

A second robust feature is that the dominant neutrino emission, with luminosities of a few 10^{54} erg s⁻¹ consists of electron antineutrinos (see Fig. 25); this is because the HMNS has a high temperature, and hence, electron-positron pairs are efficiently produced from thermal photons, but then neutrons efficiently capture the positrons to emit antineutrinos, whereas electrons are not captured by protons as frequently as positrons because the proton fraction is much smaller than the neutron fraction.

A third and somewhat expected result is that the simulations have shown that the lifetime of the

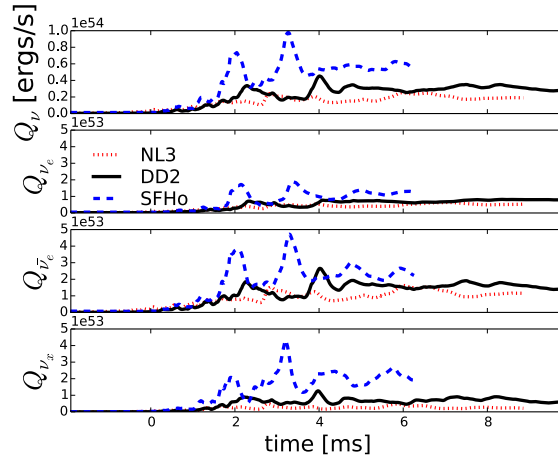


FIG. 25. Neutrino luminosities for the different EOSs used in Ref. [352]. The panels show, from top to bottom, the total neutrino luminosity and the luminosities for electron neutrinos, electron antineutrinos, and the other four lepton flavours combined. [Reprinted with permission from Ref. [352]. © (2015) by the American Physical Society.]

binary-merger product is influenced also by the timescale of neutrino cooling, as well as by the strength of the magnetic field and by the EOS. After the eventual collapse to black hole, muon and tau neutrino luminosities steeply decrease because most of the high-temperature regions are covered by the event horizon, while the luminosities of electron neutrinos and antineutrinos decrease only gradually, because these neutrinos are emitted via charged-current processes from the accretion disc.

A fourth result, due mostly to Refs. [72, 352, 418], is that after the merger, the electron fraction in the ejected matter has a broad distribution, in a range between 0.05 and 0.45 (see Fig. 26). This result is rather robust and depends very weakly on the grid resolution or the EOS considered. However, it is very different from what found in previous studies, which used either Newtonian codes [432, 433] or codes with an approximate treatment of general relativity [434, 435] and which had found that the distribution of the electron fraction was very narrow, with an average value $\lesssim 0.1$. There are several possible explanations for these differences: firstly, the Newtonian simulations of Refs. [432, 433], while taking into account neutrino cooling, underestimated significantly the effect of shock heating and thus the effect of the positron capture was much weaker. Furthermore, these simulations did not consider neutrino heating (absorption), which is expected to play an important role for stiffer EOSs, where positron capture is relatively less important because of the lower temperature [418]. Secondly, the differences with respect to approximate general-relativistic simulations [434, 435] can be explained by noting that the ejecta in such simulations remained neutron rich because weak interaction processes were not taken into account and thus there was no way to change the electron fraction [418].

Finally, in addition to these differences, Radice et al. [72] also found that the ejecta have a bimodal distribution in the electron fraction Y_e , with maxima around 0.08 and 0.16. This is because part of the outflow, driven by tidal torques, is cold and neutron rich, while another component, launched by shocks during merger, has high temperatures and rapid protonisation with values of Y_e peaking around 0.16.

As a concluding remark in this section we note that the presence of magnetic fields and radiative

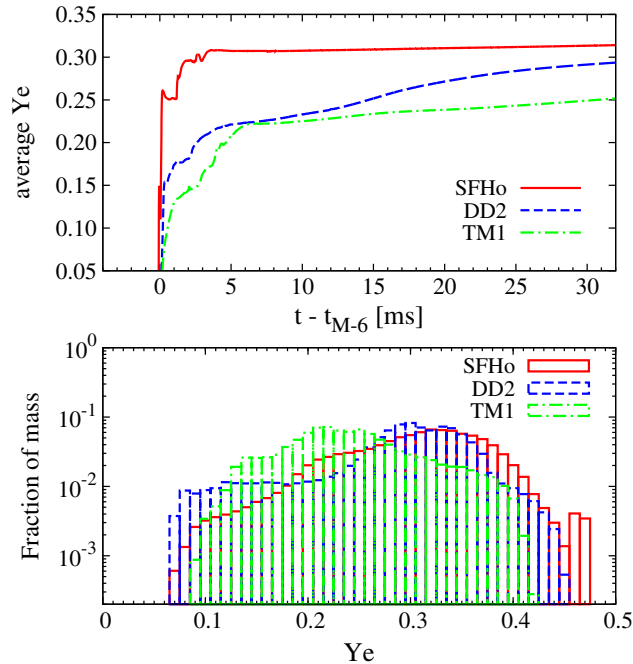


FIG. 26. *Upper panel*: evolution of the averaged value of the electron fraction Y_e for different EOSs: SFHo (red solid), DD2 (blue dashed), and TM1 (green dotted dashed). *Lower panel*: mass-distribution histograms of Y_e normalized to the total mass of ejecta measured at about 25 ms after the onset of merger for SFHo, DD2, and TM1. [Reprinted with permission from Ref. [418]. © (2015) by the American Physical Society.]

losses in full general relativity has been considered so far only by Neilsen et al. [206] and by Palenzuela et al. [352]. Their results indicate that magnetic fields do not seem to play a significant role in modifying the neutrino emission, although the resolutions employed were somewhat lower than the ones needed to resolve the complex dynamics behind magnetic-field amplification. Particularly interesting in the work of Neilsen et al. [206] is the use of a novel method for the calculation of the optical depth, which simplifies its use with distributed adaptive mesh refinement and has later been employed also in Ref. [72].

C. Non-bulk dynamics: ejecta, nucleosynthesis and afterglows

In what follows we will concentrate on two advanced topics that have been pursued in the modelling of merging BNSs and that revolve about the dynamics of that *tiny* amount of matter (i.e., $\lesssim 0.1\%$ of the total mass of the system) that does not participate to the bulk dynamics nor is ultimately accreted onto the black hole, but that leaves the system because it becomes gravitationally unbound. Over the last few years a lot of progress has been made in the study of such material ejected from BNSs during and after the merger. The neutron-rich dense material that becomes gravitationally unbound and so escapes to larger distances, undergoes decompression and changes in its electron fraction, so that rapid neutron capture processes (i.e., “ r processes”) [436] and radioactive decays [45, 47, 437, 438] take place. While r processes are responsible for the nucleosynthesis of heavy

elements, possibly playing a fundamental role in the cosmic chemical evolution, the radioactive decays could lead to the release of large amounts of electromagnetic radiation which would become observable as a delayed electromagnetic counterpart. Both of these processes are related to two outstanding issues in astrophysics: the explanation of the observed heavy-element abundance in the Universe and the modelling of afterglows (of SGRBs or mergers) that are expected to produce optical and infrared (or even longer-wavelength) emissions. Although such topics are obviously closely related, we present them separately in Sects. [VIC 1](#) and [VIC 2](#), as this helps us collect the various contributions.

1. Ejected matter and nucleosynthesis

As mentioned above, that of the construction of the chemical abundance presently observed in the Universe is a long-standing problem in astrophysics. It is clear that Big-Bang nucleosynthesis cannot produce heavy elements and that these need to be produced within stars through their nuclear evolution. Core-collapse supernovae have been traditionally considered as the channel through which heavy elements produced via r processes can be distributed across the Universe. This picture, however, is becoming increasingly difficult to support as the numerical simulations are showing that the physical conditions necessary to produce elements with atomic number $A > 90$, namely, high entropy, low electron fraction, and very rapid expansion, are hard to be met in core-collapse supernovae. Such conditions, however, are quite natural in BNS mergers, which have therefore become an interesting alternative for r -process nucleosynthesis and the construction of heavy/very-heavy elements in the Universe.

We recall that BNS mergers can release neutron-rich matter in at least four different ways (see also Sect. [VIA 3](#)): (i) in the matter that is ejected dynamically via gravitational torques (tidal ejection) [[58](#), [435](#), [438](#), [439](#)] or shocks [[440](#)]; (ii) through neutrino-driven winds [[321](#), [396](#), [402](#), [417](#), [418](#), [441](#), [442](#)]; (iii) through magnetically driven winds (see Sect. [VIA 3](#) [[75](#), [367](#), [393](#), [394](#), [443](#)]); (iv) from shock waves in the late-time evolution of accretion discs [[74](#), [444](#)]. In all cases, the ejected matter is neutron-rich, cold if dynamically ejected (i.e., if not shock heated), and in beta equilibrium; however, to the different channels correspond different amounts of ejected matter, as well as different distributions in entropy, electron fraction, and velocity. As a result, they might possibly produce different nucleosynthetic signatures [[72](#), [150](#), [321](#), [396](#), [402](#), [417](#), [418](#), [442](#), [445](#)].

Perhaps in no aspect of the dynamics of BNS mergers other than that of the ejected matter and nucleosynthesis are the differences between various approaches larger. On the one side, there are codes making use of Newtonian (or pseudo-Newtonian) descriptions of gravity and implementing either SPH techniques [[150](#), [433](#), [435](#), [445–447](#)] or Eulerian hydrodynamics approaches [[396](#), [402](#), [442](#)], which are combined with very advanced treatments of radiative transfer and nuclear-reaction networks. In addition, either exploiting symmetries or larger timesteps, these codes can achieve evolutions of the dynamical ejecta over very long-term and through direct hydrodynamical simulations lasting up to 100 years and over a density range of roughly 40 orders of magnitude. On the other side, there are codes in full general relativity, but that implement simpler approaches to the neutrino radiative losses and are necessarily restricted to much shorter timescales [[72](#), [300](#), [320](#), [321](#), [352](#), [417](#), [418](#)]. Inevitably perhaps, these methodological differences are then responsible for systematic differences in the results from the two classes of approaches. Fortunately, these differences are mostly quantitative, leaving behind a qualitative picture which is instead rather robust.

The most important quantitative difference is in the actual amount of mass ejected. Codes adopting approximate treatments of gravity, in fact, tend to overestimate the relative ratio of tidally- to shock-driven ejecta for quasi-circular binaries [[304](#)]. More specifically, simulations that are not

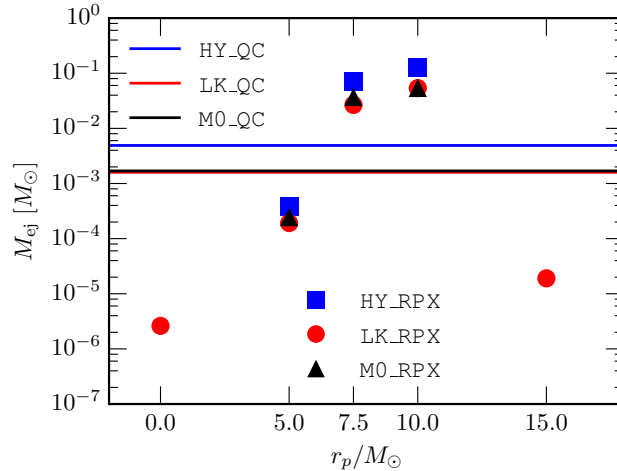


FIG. 27. Dynamically ejected mass for BNS mergers coming either from dynamical encounters or from quasi-circular inspirals (in this latter case since the mass does not depend on r_p , it is marked as a horizontal line). The ejecta mass is computed integrating in time the flux of unbound matter (with the covariant time-component of the four-velocity $u_t \leq -1$) across the surface of a spherical sphere with radius $r \simeq 295$ km. Overall, eccentric binaries can eject up to 2 orders of magnitude more mass than quasi-circular binaries. [Adapted from Ref. [72].]

fully general-relativistic show that even mergers from equal-mass systems tend to develop prominent tidal arms before the actual contact. At the same time, these simulations tend to underestimate the strength of the shocks that develop at the merger and that are able to impart larger kinetic and internal energies to the shocked material [72, 448]. Both of these aspects are clearly the consequence of “shallower” gravitational potentials than those computed in general relativity, which tend to produce larger “spills” of matter during the inspiral and less “catastrophic” mergers. These differences apply also to eccentric binaries, where Newtonian studies tend to overestimate the amount of shocked ejecta, leading to outflows that are more proton-rich in eccentric binaries than in quasi-circular mergers [150] (see also Sect. VD). In contrast, general-relativistic eccentric mergers are typically more neutron rich than those of quasi-circular mergers, the reason being that the ejecta in eccentric mergers is increasingly dominated by the tidal component [72].

A summary of how much the amount of ejected matter can vary under different physical conditions, either before the merger (quasi-circular versus eccentric encounters) or after the merger (in pure hydrodynamics or with radiative effects taken into account) is shown in Fig. 27, which is taken from the work of Radice et al. [72]. More specifically, shown are the total ejected rest mass as computed integrating in time the flux of matter with covariant time-component of the four-velocity $u_t \leq -1$, across a spherical coordinate surface with radius $\simeq 295$ km²⁵. Shown with symbols are the results of simulations of BNS systems on parabolic orbits with varying impact parameters, while the horizontal lines show the corresponding results when considering binaries in quasi-circular orbits (the gravitational masses are essentially the same in the two cases) [72].

Note that the eccentric mergers lead to considerably larger amounts of ejected masses, which is

²⁵ A detailed discussion of possible alternative criteria to identify unbound fluid elements has been made by Kastaun and Galeazzi [74].

hardly surprising given that the binaries themselves are in this case only weakly bound. Furthermore, the mass lost depends sensitively on the impact parameter, showing a local maximum for BNS systems close to the threshold between prompt merger and multiple-encounters [72, 109]. Overall, eccentric encounters can yield up to $\sim 0.1 M_{\odot}$ of ejecta, slightly less than what can be achieved with black-hole–neutron-star mergers [300, 449], but almost two orders of magnitude larger than what is ejected by mergers of BNSs in quasi-circular orbits [72] and one order of magnitude larger than what is ejected in unequal-mass BNS mergers in quasi-circular orbits [321]. The ejecta from unequal-mass BNS mergers may also have a different composition (electron fraction), because the tidal component is larger for mass ratios more different from one [320, 321].

The amount of ejected matter also depends on the inclusion of radiative losses, which are either absent (blue squares) or accounted via a neutrino leakage (red circles) or an “M0” approach (black triangles), discussed in Sect. VIB. The differences in this case are far smaller, but it is also clear that neglecting neutrino cooling results in an overestimate of the unbound mass by a factor $\gtrsim 2$. This is because neutrino losses in the optically thin outflows are rapid and sufficient to cause part of the material to become gravitationally bound again by removing part of its internal energy. Finally, we note that the amount of matter ejected from quasi-circular mergers is larger if the progenitors are spinning. Kastaun and Galeazzi [74] measured ejecta masses of a factor of a few larger for constraint-violating spinning initial data (see discussion in Sect. IVB). More work is needed to further explore ejecta in the case of realistic spins and constraint-satisfying initial data.

Next, we turn our attention to the nucleosynthesis resulting from the ejected matter. In this context, when discussing more in detail the results of a number of simulations performed by various groups using different approaches and approximations, we will distinguish those works that focused on the nucleosynthesis of matter that was dynamically ejected from those studies that instead focused on neutrino-driven ejecta. For the first class of simulations, the ejecta are normally followed through the times when radioactively powered transients should peak (of the order of days) and up to the point when the radio flares from the interaction with the ambient medium are expected (of the order of years). Essentially all results, independently of whether performed in full general relativity [72, 300, 320, 321, 352, 381, 418, 450] or with approximate treatments of gravity [150, 439], conclude that the dynamical ejecta very robustly produce strong r -process elements with $A > 130$ with a pattern that is essentially independent of the details of the merging system. In particular, the r -process peaks around $A \approx 130$ and $A \approx 195$ are fairly independent from the details of the initial data used (quasi-circular or eccentric) or the details of the radiative losses (from pure hydrodynamics simulations over to those having “M1” approaches) [72].

Furthermore, the recent simulations by Wanajo et al. [417], Sekiguchi et al. [418], and Radice et al. [72], using a general-relativistic treatment, advanced neutrino transport schemes and state-of-the-art finite-temperature EOSs, also showed that the dynamical and early-merger neutrino-wind ejecta of BNS mergers can be the dominant origin of all the Galactic r -process nuclei. These general-relativistic simulations [72, 417, 418] have highlighted that shock-heated and neutrino-processed dynamical ejecta from the HMNS are not made of almost pure neutron matter (as previously thought), but also contain modestly neutron-rich matter. This result makes the r -process abundance distribution from the calculations agree with the solar one over the full range of $A \simeq 90 - 240$, while all previous works obtained a good matching without fine tuning only for the production of nuclei with $A \gtrsim 130$.

Interestingly, Goriely et al. [448], have conducted a systematic investigation of the potential impact that weak interactions could have on the electron-fraction evolution in merger ejecta, suggesting that the relative contributions of matter in the intervals $A \lesssim 90$, $90 \lesssim A \lesssim 140$ and $A \gtrsim 140$ depend strongly not only on the EOS, but also on whether a large tidal tail develops after the merger. If this is the case, considerable amounts of cold, unshocked matter could be centrifugally ejected before the neutrino luminosities rise and thus before neutrino exposure of these ejecta plays an important role.

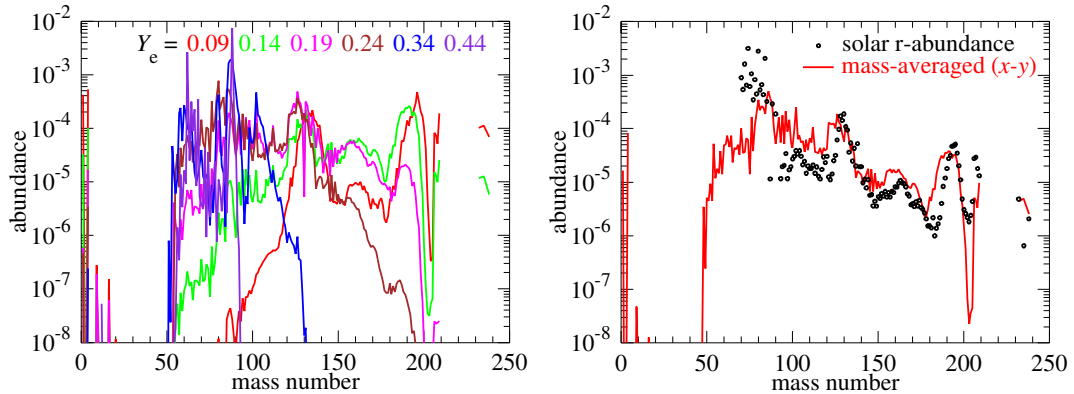


FIG. 28. *Left panel:* Final nuclear abundances for selected trajectories with given electron fraction on the orbital plane. *Right panel:* Comparison between the solar r -process abundances and the mass-averaged nuclear abundances obtained by weighting the final yields for the representative trajectories in the simulations with their electron-fraction mass fractions on the orbital plane. [Adapted from Ref. [417] with permission by the authors.]

Under these conditions, the ejecta will be expelled highly anisotropically and will carry a dominant fraction of the mass in the form of $A \gtrsim 140$ nuclei [448].

A summary of the results relative to the nucleosynthesis of the matter ejected in BNS mergers is shown in Fig. 28, which is taken from the work of Wanajo et al. [417], where thermodynamical trajectories of particles in the ejecta are traced on the orbital plane and each representative particle is chosen from a bin defined by an electron fraction $0.09 \leq Y_e \leq 0.44$. The left panel, in particular, shows the final nuclear abundances for the selected trajectories, which reproduce a variety of nucleosynthetic features: the iron-peak and $A \approx 90$ abundances made in nuclear quasi-equilibrium for $Y_e \gtrsim 0.4$, light r -process abundances for $Y_e \approx 0.2\text{--}0.4$, and heavy r -process abundances for $Y_e \lesssim 0.2$. The right panel, on the other hand, shows the mass-averaged nuclear abundances by weighting the final yields for the representative trajectories with their Y_e mass fractions on the orbital plane. The agreement with the solar r -process abundance distribution over the full atomic-number range of $A \approx 90 - 240$ is quite good; an even closer agreement in the high- A regime, including in particular the second $A \approx 130$ and third $A \approx 195$ peaks, has been shown recently by Radice et al. [72], by considering full three-dimensional trajectories, not restricted to the orbital plane.

When considering now those studies that focused on neutrino-driven ejecta, we should note that in this case, because one needs to explore timescales that are of the order of seconds (and not of tens of milliseconds), the simulations all employ some approximation, either in the treatment of gravity or in the underlying spatial symmetries. With these considerations in mind, the inclusion of neutrino transport and the contribution from neutrino-driven winds in long-term simulations do bring different results for the properties of the dynamical ejecta of the merger such as total mass, the average electron fraction, and the thermal energy, and thus for the properties of the nucleosynthesis as well [396, 417, 418, 441, 442]. This is because some fraction of the total ejected material comes through neutrino dynamics, especially for stiffer EOSs. Furthermore, such ejecta have the peculiarity of being emitted also at high latitudes, near the rotation axis, while other types of ejecta are mostly constrained to lower latitudes. More specifically, Perego et al. [396] found that the neutrino winds provide a substantial contribution to the total mass lost in a BNS merger and that material ejected at higher and lower latitudes has different properties. It was found that polar ejecta, characterized by more intense neutrino irradiation, larger electron fraction, entropies, and expansion velocities,

produce r -process contributions from $A \approx 80$ to $A \approx 130$, while the more neutron-rich, lower latitude parts produce elements up to the third r -process peak, near $A \approx 195$.

An exhaustive analysis has been carried out by Just et al. [442], who employed a three-dimensional relativistic SPH code, using the conformally flat approximation for the spacetime [434] and different microphysical EOSs for nonzero-temperature neutron-star matter. The subsequent, seconds-long evolutions of the black-hole–accretion-torus system were carried out starting from tori in rotational equilibrium with a Newtonian hydrodynamics code that includes dynamical viscosity effects, pseudo-Newtonian gravity for rotating black holes, and an energy-dependent two-moment closure scheme for the transport of electron neutrinos and antineutrinos. As a result of their analysis, Just et al. [442] reiterated that the solar r -abundance pattern can be reproduced well in the whole range $90 < A < 240$ by a mass-weighted combination of the dynamical ejecta from the BNS merger phase and the secular ejecta from the black-hole–torus evolution, to which neutrino-powered winds contribute only at most another 1%. In particular, the black-hole–torus outflows are able to reproduce well the region $A \lesssim 140$, where the prompt merger ejecta under-produce the nuclear abundances.

In conclusion, research on the ejected matter and the consequent heavy-element nucleosynthesis from BNS mergers is a comparatively young field of research that has already seen considerable efforts at multiple levels of mathematical approximation and physical sophistication. Overall, the results show that amounts of matter in the range $10^{-3} - 10^{-1} M_{\odot}$ can be lost to spatial infinity in the course of the merger and post-merger dynamics, and that the details depend on a rich combination of factors: EOS, mass ratio, pre-merger dynamics, etc. At the same time, robust results emerge from the nuclear evolution of the ejected matter, which provides a surprisingly good match with the chemical abundances observed and promotes BNS mergers to a primary role in the chemical enrichment of the Universe. These promising first results also call for further investigations to set on firmer grounds a number of details that have been neglected so far for a number of reasons. These include: long-timescale fully general-relativistic calculations, improved treatments of radiative transfer, and more advanced numerical approaches for the study of the tiny and tenuous component of the BNS matter that is ejected at the merger.

2. *Macronovae and other afterglows*

Observations of electromagnetic radiation from astrophysical events that also emit gravitational radiation will be very important and for several reasons. Such simultaneous detections of electromagnetic and gravitational-wave signals, in fact, would significantly increase the confidence in the detection of gravitational waves [445, 451]. Furthermore, such delayed electromagnetic counterparts would contribute considerably to the sky localisation of astrophysical events emitting gravitational waves. Since gravitational-wave detectors will have only moderate space localisation capabilities (of the order of one square degree at best), electromagnetic observations can be crucial for extracting information about the astrophysical properties of the source and of its environment (e.g., the host galaxy and its redshift).

As discussed in detail in Sect. VB, in addition to SGRBs, which are the most plausible electromagnetic manifestation of BNS mergers [29, 30], and certainly the best studied electromagnetic emission that such mergers could produce (either before or after the merger; see Sect. VIA 1), there is also another class of delayed electromagnetic counterparts to BNS mergers that has caught a widespread attention recently. This electromagnetic emission is the one caused by the radioactive decay taking place mostly in ejecta and by the interaction of the ejecta with the interstellar medium, long time after the merger. This is nicely summarised in the schematic diagram in Fig.29, which illustrates the various potential electromagnetic emissions from the post-merger phase. In this Sec-

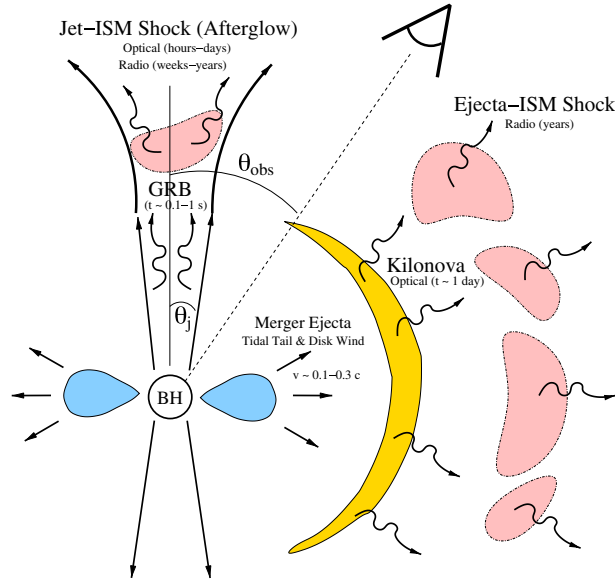


FIG. 29. Schematic summary of potential electromagnetic counterparts of BNS mergers, as a function of the observer angle, θ_{obs} . Following the merger, a centrifugally supported disc (blue) remains around the central compact object (usually a black hole). Rapid accretion lasting ~ 1 s powers a collimated relativistic jet, which produces a SGRB. Due to relativistic beaming, the gamma-ray emission is restricted to observers at small viewing angles. Non-thermal afterglow emission results from the interaction of the jet with the surrounding circumburst medium (pink). Optical afterglow emission is observable on timescales up to days/weeks by observers with larger viewing angles. Radio afterglow emission is observable from all viewing angles (isotropic) once the jet decelerates to mildly relativistic speeds on a timescale of weeks/months, and can also be produced on timescales of years from sub-relativistic ejecta. Short-lived isotropic optical emission lasting a few days (kilonova/macronova; yellow) can also accompany the merger, powered by the radioactive decay of heavy elements synthesised in the ejecta. [Reproduced from Ref. [451] with permission by the authors.]

tion, we will address the latter processes, among which the most promising are the *macronovae* (or *kilonovae*) [43–50].

We recall that macronovae [45] are electromagnetic emissions about one to three orders of magnitudes brighter than regular novae (which are caused by hydrogen fusion explosions on a white dwarf accreting from a larger companion star), hence the name macronovae [46] or kilonovae [47]. In the standard scenario, macronovae shine days after the merger in ultra-violet, optical, and infrared bands probably because of radioactive decay of r -process elements [45–47] (however, see also [452] for an alternative explanation). Macronovae are particularly promising delayed electromagnetic counterparts because their emission is relatively isotropic, contrary to SGRBs, which are thought to be highly beamed; furthermore, statistical evidence being presently collected indicates that they may be ubiquitous [49]. Hence, the probability of observing electromagnetic radiation from a given macronova together with the gravitational waves from the BNS system is larger than the probability to observe the SGRB together with the gravitational emission.

The results of numerical simulations agree on the fact that the nuclear decay in ejecta from BNS mergers is consistent with the electromagnetic radiation observed as macronovae, even if, as pointed out in detail in Ref. [72], different initial data and levels of microphysical description give intrinsic

luminosities and peak times that are different of factors of a few. The consistency is present notwithstanding the fact that the codes used for such simulations are rather diverse, both in the mathematical description and in the numerical techniques used. Some codes, in particular, make use of Newtonian (or pseudo-Newtonian) descriptions of gravity and implement either SPH techniques [395, 435] or Eulerian hydrodynamics approaches [396, 442], which are combined with very advanced treatments of radiative transfer and nuclear-reaction networks. In addition, either exploiting symmetries or larger timesteps, these codes can achieve evolutions of the dynamical ejecta over very long-term and through direct hydrodynamical simulations lasting up to 100 years and over a density range of roughly 40 orders of magnitude. Other codes, instead, implement full general relativity, but simpler approaches to the neutrino radiative losses and are necessarily restricted to much shorter timescales [72, 417].

Another feature found irrespective of the various approaches used is the clear dependence of the optical emission on the EOS of the neutron stars, with softer EOSs yielding brighter transients and peaking on longer timescales and with a lower effective temperature [72, 417, 435, 450]. Finally, also a commonly observed feature is the dependence on the binary mass ratio, with brighter emissions with increasingly smaller mass ratios [450]. Both these last two features are rather easy to explain as softer EOSs and smaller mass ratios generically yield larger ejecta and hence larger amounts of matter undergoing radioactive decay.

In view of this, the dependence on the EOS and in particular the relations between peak luminosity (or peak timescale or effective temperature at the time of the peak luminosity) and the original stellar radii suggest the possibility to constrain neutron-star radii and thus the high-density EOSs from observations of optical transients associated with BNS mergers [416, 435, 450]. Following this line of thought, Hotokezaka et al. [416] were the first to attempt to extract information on possible progenitor models for the macronova transient associated with GRB 130603B. Assuming that the electromagnetic transient was powered by the radioactive decay of r -process elements, they estimated that the central engine of GRB 130603B was a massive torus of approximately $0.1 M_{\odot}$ produced in a BNS merger and accreting onto a spinning black hole. Soft EOS models were found to be favoured to explain the observations.

As mentioned in Sects. VIB and VIC 1, the inclusion of neutrino transport in simulations does bring different results for the properties of the dynamical ejecta of the merger, such as total mass, average electron fraction, and thermal energy, and thus for the properties of the nucleosynthesis as well [72, 320, 321, 396, 417, 418, 441, 442]. This is because some fraction of the total ejected material is the result of neutrino emission, in particular for stiffer EOSs as these produce smaller amounts of dynamical ejecta.

Using a pseudo-Newtonian code that solves the hydrodynamics equations with dynamical viscosity and in axisymmetry, Metzger and Fernández [395] have studied the dependence of the ejecta and their emissions over the lifetime of the HMNS, till its collapse, if this takes place²⁶. Starting with models of tori in equilibrium and approximating the HMNS as a reflecting inner boundary at a fixed radius, they found that the lifetime of the merger remnant may be directly imprinted in the radioactively powered macronova emission following the merger. In fact, when black-hole formation is relatively prompt (i.e., when the HMNS survives for $\lesssim 100$ ms), outflows from the disc are sufficiently neutron rich to form heavy r -process elements, resulting in week-long emission with a spectral peak in the near-infrared, similar to that produced by the dynamical ejecta, emitted during the merger. In contrast, if the black-hole formation is delayed, neutrinos from the HMNS are able to raise the electron fraction in the polar direction to values such that outflows may be generated.

²⁶ We should note that the use of a viscosity description instead of magnetohydrodynamics modelling is a major source of uncertainty as it may well influence the nucleosynthetic predictions, as shown in Ref. [442].

The lower opacity of this region would then produce a brighter, bluer, and shorter-lived day-long emission prior to the late peak in the near infrared from the dynamical ejecta and equatorial wind.

Almost at the same time, Perego et al. [396], presented detailed, three-dimensional viscous-hydrodynamics simulations performed with a Newtonian Eulerian code with a spectral neutrino leakage scheme accounting for neutrino absorption (but not for neutrino annihilation in optically thin conditions, which may further enhance ejecta). The simulations were started from a direct re-mapping of the matter distribution of three-dimensional SPH simulations of the merger of two non-spinning $1.4 M_{\odot}$ neutron stars obtained through the code of Rosswog and Price [453], covering the time interval up to about 100 ms after the merger and including a spatial domain extending up to 1500 km from the HMNS, which was again treated as an inner boundary. With this setup, Perego et al. [396] found that the collapse timescale has a minor impact on electromagnetic counterparts and nucleosynthesis yields, in contrast to the results of Metzger and Fernández [395]. Perego et al. [396] also remark that winds from the polar regions produce ultraviolet and optical transients reaching luminosities up to $10^{41} \text{ erg s}^{-1}$ and peaking around one day after emission, as found by Metzger and Fernández [395] too. Winds from lower latitude regions, instead, being contaminated with high-opacity heavy elements, produce dimmer and redder signals, peaking after about two days in optical and infrared.

More recently, Metzger et al. [447] considered the electromagnetic emissions coming from the decay of free neutrons emitted by the BNS merger, following a suggestion first pointed out by Kulkarni [46]. Even if most of the material ejected is so dense that almost all neutrons are captured into heavy nuclei via r processes, some fast expanding matter ejected during the initial phases of the merger from the interface between the two stars could produce a relevant flow of free neutrons. Such free neutrons could alter the early macronova light curves, since their decay timescale is long and they release a large quantity of energy per decay as compared to the majority of the r processes. The signature of free-neutron decay would be a blue/visual bump that peaks at a luminosity $L_{\text{tot}} \sim 10^{41} \text{ erg s}^{-1}$ on a timescale of less than few hours after the merger. Metzger et al. [447] calculated that the observation of the imprint of free neutrons on the light curve is within reach of near-future telescopes and that the presence of such imprint would allow immediate discrimination between a BNS merger and the merger of a neutron star with a black hole, which would not show such a feature.

When considering fully general-relativistic approaches to the modelling of the macronova afterglow emission, much less has been done and the state-of-the-art is represented by the work of Wanajo et al. [417], who employed advanced neutrino transport schemes [410, 412], finite-temperature EOSs and a detailed nuclear-reaction network. When the r processes end a few hundreds of ms after the merger, their simulations followed the β decay, fission, and α decay for a timescale of about 100 days and found that the total heating rate is dominated at all times by β decays from a small number of species with precisely measured half-lives and that therefore uncertainties in other nuclear data seem to be irrelevant. More recent works [454, 455], however, found that realistic thermalisation efficiencies of β decay may be lower than thought before and, if so, contributions from fission and alpha-decays of transuranic nuclei (whose reaction parameters are not well known) can actually be important at late times.

We conclude this Section by discussing yet another type of “afterglow” electromagnetic transient that could accompany BNS mergers and is related to the dissipation of the kinetic energy of the ejecta in the ambient interstellar medium. This dissipation manifests itself through radio flares that arise from the interaction of sub- to mildly relativistic outflows with the surrounding matter and lead to non-thermal radio synchrotron emission [456]. The resulting signal is a potentially detectable, isotropic radio emission that peaks in the radio band near 1 GHz and persists on a detectable level for weeks [72, 150, 445, 457]. Studies performed with Newtonian codes [150, 445] suggest that observations at the sub-milliJansky level at 1.4 GHz are optimal for the detection of BNS mergers

through their post-merger radio transient. However, their detectability depends strongly on the density of the medium around the merging binaries, which may be low if the binary has been ejected from its host galaxy before the merger. More recent works have considered initial configurations in full general relativity [72, 457]. In particular, Radice et al. [72] have found that, depending on the initial configurations and the level of microphysical description, the timescale for the radio emission varies from about 1 year to almost 30 years and the radio fluence may vary by more than two orders of magnitude.

VII. ADVANCED TECHNIQUES AND ALTERNATIVE SCENARIOS

A. The zoology of binary neutron-star codes

As the study of the merger of BNS systems is transforming into a mature field of research, a number of numerical codes have been developed to achieve this result, producing a relative abundance of computational infrastructures able to solve the Einstein equations together with those of relativistic hydrodynamics and MHD. Some of the codes used in the last five years for general-relativistic simulations of BNS were first written ten or more years ago and have been continuously developed since²⁷. This is the case for the `SACRA` code [65, 254, 321, 463, 464] (and the other codes developed by the group now in Kyoto, starting from Refs. [31, 197, 465]), the `Whisky` code (in its various versions [117, 119, 122, 409, 466]), the `HAD` code [33, 69, 120, 352, 467], and the code developed by the group in Illinois [363, 468–471]. A special note should be made for the publicly available Einstein Toolkit [269, 301, 339, 472–474], whose routines for hydrodynamics were originally taken from a public version of the `Whisky` code [475] and then were developed in an independent way, its implementations becoming increasingly different from the original ones.

In addition to the more “traditional” codes mentioned above, new codes have recently been developed and particular attention is deserved by the relativistic-hydrodynamics code developed by Thierfelder et al. [222] and coupled to the `BAM` infrastructure [476–478] code for spacetime evolution and grid setup. The code implements HRSC schemes on a hierarchy of mesh refined Cartesian grids with moving boxes and solves the Z4c formulation of the Einstein equations (see Sect. III B).

Another recently developed code is the one by East et al. [70, 71, 109, 479, 480], where the authors show how they evolve the fluid conservatively using HRSC methods and a refluxing AMR scheme, while the field equations are solved in the generalized-harmonic formulation [103, 104] (see Sect. III C) with finite differences, like the `HAD` code mentioned above.

Last but certainly not least, is the use of the `SpEC` computational infrastructure [481], which had been originally employed to study the inspiral and merger of binary black holes or of neutron-star–black-hole binaries [188, 421, 482–484], to investigate BNS mergers [110]. `SpEC` employs a mixed approach to solve the Einstein equations in the generalized harmonic formulation coupled to matter [481], in which the evolution equations for the spacetime metric are solved using spectral methods as described in Refs. [485–488], while the fluid equations are solved using HRSC methods as described in Refs. [188, 481, 484]. It also uses comoving coordinates, which minimise the movement of the stars on the numerical grid during the inspiral, thus decreasing the numerical error due to interpolation between different refinement levels.

As previously mentioned several times, in addition to Eulerian codes that solve the full Einstein equations without approximations (except the truncation error and the errors associated to numerical methods), some other codes currently employed for BNS merger simulations make theoretical approximations to the evolution of gravity but are very advanced in treating microphysical processes and treat matter with smoothed-particle-hydrodynamics (SPH) methods. In particular, one code of Rosswog [432, 433] assumes Newtonian gravity and another code of Rosswog [150, 312, 445, 489] and the code of Bauswein, Janka, Oechslin, and collaborators [434, 435, 442, 444, 490, 491] adopt a conformally flat approximation to general relativity.

A perhaps disappointing note that however needs to be made is that despite this abundance of numerical codes, systematic comparisons among the various codes are done seldom and the only cases we are aware of are the quantitative comparisons between the `SACRA` and `Whisky` codes [160,

²⁷ A number of other general-relativistic hydrodynamics codes on fixed spacetimes have been developed over the years for applications on astrophysical compact objects. Among such codes are: `Athena` [458], `Athena++` [459], `Castro` [460], `COSMOS++` [333], `Enzo` [461], `Flash` [462], and `HARM` [332].

492] and between the BAM and SpEC codes [110]; such comparisons are tedious and computationally expensive but important to gauge the systematic errors that the various code can introduce.

B. High-order numerical methods

In order to use results from numerical-relativity simulations to aid and interpret the analysis of gravitational-wave data from BNSs that will be soon measured by advanced detectors, it is of fundamental importance to improve not only the accuracy but also the computational efficiency of the simulations²⁸. Having these goals in mind, a number of groups have made progress in improving the numerical methods used in simulations of BNSs, starting with the simpler solution of the pure-hydrodynamics equations. There are two obvious directions in which developers are heading through improved numerical methods in numerical-relativity codes. The first one is a high convergence order of the emitted gravitational waves; the second one is the ability to limit the growth of (or even damp) the violation of the constraint equations (12), as discussed in detail in Sect. III B.

In this context, the newly developed `WhiskyTHC` code by Radice, Rezzolla and Galeazzi [117, 193, 194] deserves a special mention as it represents the first relativistic-hydrodynamics code employing high-resolution shock-capturing, finite-differencing schemes to go beyond second-order convergence in the modelling of BNS mergers²⁹. Thanks to this increased convergence order, from the $\simeq 1.8$ of “traditional” codes such as `Whisky` to $\simeq 3.2$ of `WhiskyTHC`, Radice et al. [117, 193, 194] were able to compute very accurate gravitational waveforms, including those for higher-compactness binaries, which are much more challenging to evolve accurately, because numerical viscosity becomes the leading source of de-phasing from the point-particle limit, since tidal effects are small. For all of the simulated BNSs, remarkable agreement was found between Richardson-extrapolated numerical waveforms and the ones from the tidally corrected post-Newtonian Taylor-T4 model [212, 235, 288, 493–495].

As the name implies, `WhiskyTHC` results from the merger of two codes: `Whisky` [496] and `THC` [349]³⁰. It inherited from `THC` the use of state-of-the-art high-order flux-vector splitting finite-differencing techniques and from `Whisky` the module for the recovery of the primitive quantities as well as the new EOS framework recently introduced in Ref. [409]. More specifically, `WhiskyTHC` employs a flux-vector splitting scheme that uses up to seventh-order reconstruction in characteristics fields and a novel entropy-fix prescription for the Roe flux splitting [193].

Among other more traditional algorithms, `WhiskyTHC` implements the formally-fifth-order-in-space MP5 scheme³¹ [497] for the flux reconstruction of the local characteristic variables, using in particular the explicit expression for the eigenvalues and left- and right-eigenvectors that can be found in, e.g., Ref. [59]. The spacetime is evolved via an implementation of the CCZ4 formulation (see Sect. III B) publicly available in the `Mclachlan` code [498] of the Einstein Toolkit [472–474].

As shown in Fig. 30, the convergence order of `WhiskyTHC` is 3.2 in the phase (left panel) and the amplitude of the gravitational waves, without the need to perform any artificial manipulation of the waveforms [194]. The measured order of convergence of 3.2 is somewhat smaller than the formal order of four of the scheme, but this is expected because HRSC methods typically reach

²⁸ The computational efficiency of the simulations can be defined in a number of different ways, but an effective one involves the computational cost in terms of CPU hours to obtain a given result with a specified truncation error. The smaller the number of CPU hours to obtain a result with a given truncation error, the more efficient the code.

²⁹ By using standard finite-difference methods, Hotokezaka et al. [221] also reported third- or higher-order convergence in some specific derived quantities in their long (i.e., $\simeq 16$ orbits), low-initial-eccentricity ($\lesssim 10^{-3}$) simulations; however the phase evolutions of the gravitational waves from simulations with different resolutions could be matched only after a suitable stretching of the time coordinate; it is not clear how this affects the convergence order.

³⁰ `THC` stand for Templated-Hydrodynamics Code. The “templated” aspect reflects the fact that the code design is based on a modern C++ paradigm called template metaprogramming, in which part of the code is generated at compile time. Using this particular programming technique it is possible to construct object-oriented, highly modular codes without the extra computational costs associated with classical polymorphism, because, in the templated case, polymorphism is resolved at compile time allowing the compiler to inline all the relevant function calls.

³¹ Other codes also implement variations of this scheme.

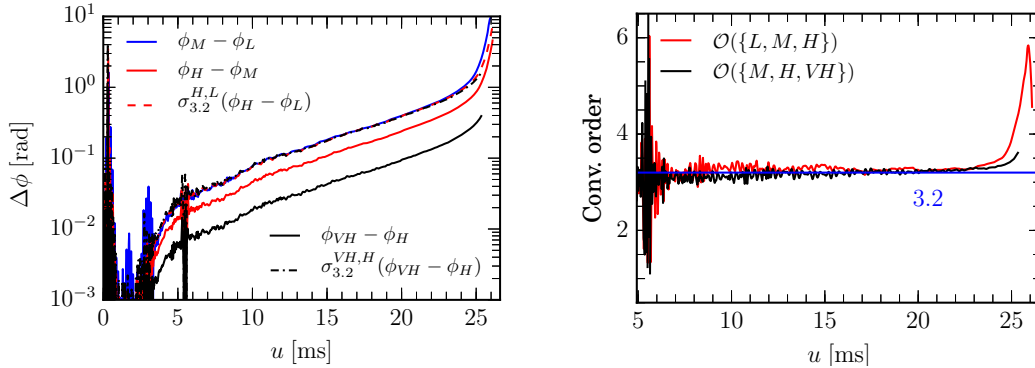


FIG. 30. Accumulate de-phasing (left panel) and estimated order of convergence (right panel) for the $\ell = 2, m = 2$ mode of the Weyl scalar Ψ_4 as extracted at $r = 450 M_\odot$. The de-phasing between high (H) and medium (M) and very high (VH) and high are also rescaled assuming an order of convergence of 3.2. The M, H , and VH resolution correspond to spatial spacings on the finest grid of $h = 0.2, 0.133, 0.1 M_\odot \simeq 295, 197, 148$ m, respectively. The instantaneous order of convergence is estimated separately from the first three resolutions $\mathcal{O}(\{L, M, H\})$ and from the last three $\mathcal{O}(\{M, H, VH\})$. Adapted from Ref. [194]

their nominal convergence order only at higher resolutions [349, 499]; see also Ref. [500] for a discussion of other possible sources of errors. Finally, Fig. 30 illustrates the fact that the solutions obtained through `whiskyTHC` show a loss of convergence (with apparent super-convergence) after time $u \gtrsim 24.6$ ms, as also observed with other codes [35]. This is roughly the time when the two neutron stars enter into contact. At this time the de-phasing between the H and VH resolution is $\simeq 0.26$ rad; such dephasings over almost seven orbits are comparable with those obtained for binary black-hole waveforms [175] and highlight that, given sufficiently good initial data, very accurate waveforms can be computed also for BNS mergers.

The possibility of employing high-order weighted-essentially-non-oscillatory (WENO) schemes [59, 499] in BNS mergers has been first considered by De Pietri et al. [301], who, through a series of simulations employing both the BSSNOK and the CCZ4 formulations and making use of the public codes within the Einstein Toolkit. Besides proving the maturity of such codes, Pietri et al. [301] have shown the ability of these schemes to yield physically consistent results even at rather low resolutions³². Simulations of BNS mergers with WENO schemes have also been reported more recently by Bernuzzi and Dietrich [501], who find that these schemes can be employed robustly for simulating the inspiral-merger phase and can improve the assessment of the error budget in the calculation of the gravitational waveforms when compared to finite-volume methods. The convergence order reported by Bernuzzi and Dietrich [501], however, is only $\simeq 2$, mostly because optimal choices for the WENO weights for this type of problem and in this range of frequencies are not available yet.

Before concluding this Section, we note that an effort has been invested recently also in the application of discontinuous-Galerkin methods [59, 502–504] within general-relativistic codes solving the equations of relativistic hydrodynamics or MHD. This is very much a growing field and, at present, these studies are either limited to dynamical curved spacetimes in one spatial dimension [505], to fixed curved spacetimes in three spatial dimensions [506], or to flat spacetimes, but in

³² De Pietri et al. [301] also remarked that the CCZ4 formulation normally requires higher resolutions to obtain consistent results, in agreement with what reported by Alic et al. [92].

relativistic MHD [507, 508].

C. Advanced Numerical Techniques

Among the advanced numerical techniques recently introduced in numerical-relativity codes modelling BNS mergers there is one that deals with the rather delicate treatment of interfaces between fluid regions and regions supposed to be vacuum. As mentioned above, this is one of the most challenging problems in Eulerian (relativistic) hydrodynamics codes (see e.g., [509–511]). As mentioned in Section III E, the most commonly used approach to treat vacuum regions is to fill them with a low-density fluid, the *atmosphere*, such that if the evolution of a fluid element would bring it to have a rest-mass density below a certain threshold, some hydrodynamical variables are set to a floor value. This approach works reasonably well for standard second-order codes and has been adopted, with some variations, by the vast majority of the relativistic-hydrodynamics codes, but it is problematic for higher-order codes [505]. The reason is that small numerical oscillations can easily couple with the prescription for the floor, violating the conservative character of the equations and affecting artificially the conservation of mass, energy, and momentum. Such oscillations may be amplified and ultimately cause instabilities in the evolution.

Radice et al. [117] have proposed and tested different solutions to this problem, finding that the positivity-preserving limiter recently proposed by Hu et al. [512] is the one that works best. This method still requires a low-density fluid everywhere and the enforcement of a floor value, but has the important property of enforcing the local conservation of the solution up to floating-point precision. In practice, the floor for the rest-mass density can be arbitrarily small and does not require any tuning. In contrast, the classical atmosphere prescriptions usually work only in a limited range floor values. The final prescription is rather simple: one fills the vacuum with a low rest-mass density floor at the beginning of a simulation and then lets it evolve freely, only relying on the positivity preserving limiters to ensure its proper behaviour. This typically results in the creation of accretion flows onto the compact objects, but, given the low rest-mass density that can be chosen for the floor³³, the effects of this artificial accretion are completely negligible. Radice et al. [117] tested all their proposed different atmosphere prescriptions and found that they give identical results during the inspiral and yield very marginal differences in the merger phase, while significant differences may appear in the post-merger phase. This suggests that the treatment of the neutron-star surface is not a leading source of error in BNS simulations, as far as the inspiral gravitational-wave signal is concerned.

Also worth discussing as an advanced numerical technique in codes for BNS mergers is the solution of the problem of small violations of the conservation of rest-mass that can take place when the fluid flow crosses a mesh-refinement boundary. These violations are the result of the jump in resolution across the refinement levels that, because of the average nature of finite-volume methods, can lead to violations of the conservative formulation of the hydrodynamic equations. The solution to this problem is called *refluxing* and was originally proposed by Berger and Colella [513]. As suggested by the name, the refluxing technique involves a suitable correction of the fluid fluxes across the mesh-refinement boundaries so as to enforce the conservative nature of the equations.

A first implementation of this technique within the Einstein Toolkit [339, 472–474] was performed by Reisswig et al. [514] and was later followed by Dietrich et al. [299], who carried out a detailed study of its efficacy. In particular, as shown in the left panel of Fig. 31, results obtained with and

³³ In Refs. [117, 193, 194], the atmosphere floor is taken to be 16 orders of magnitude smaller than some reference rest-mass density (normally the initial maximum rest-mass density), essentially below floating-point precision.

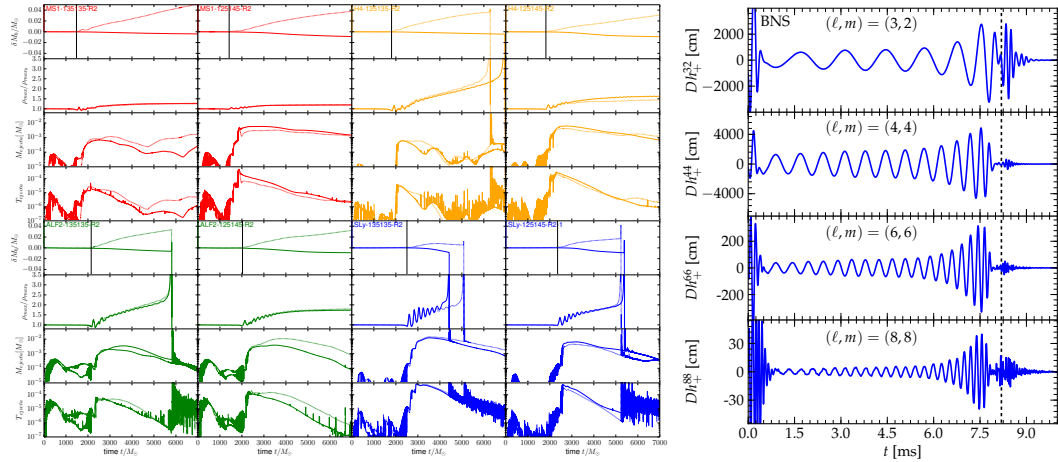


FIG. 31. *Left panel*: Evolution of some dynamical quantities for simulations of configurations with total mass $M = 2.7M_{\odot}$ and initial mass ratios $q = 1$ and $q = 1.16$. Results for different EOSs are in different colours. For each configuration, the panel contains four plots. From top to bottom: violation of rest-mass conservation $\delta M = M(t) - M(t = 0)$ on the intermediate fixed refinement level; maximum rest-mass density on the grid scaled to its initial value; rest mass of the ejected material; kinetic energy of the ejecta. Results for conservative AMR are presented with solid lines, while the corresponding results for nonconservative AMR are shown with dashed lines. Vertical lines indicate the time of merger, determined by the maximum in the gravitational-wave amplitude. [Reprinted with permission from Ref. [299] © (2015) by the American Physical Society.] *Right panel*: Various gravitational-wave modes (ℓ, m) from a BNS simulation, obtained via Cauchy-characteristic extraction. The vertical line indicates the time of appearance of an apparent horizon. [Reprinted with permission from Ref. [514]. © (2013) by the American Physical Society.]

without the conservative mesh-refinement algorithm were compared, and it was found that simulations of the post-merger phase can be affected by systematic errors if mass conservation across mesh refinements is not enforced. Such errors may affect estimates of the mass of the ejecta by factors of several. The computational overhead due to the enforcement of rest-mass conservation amounts to an increase of the evolution time of $\sim 10\%$ at most, which is quite acceptable in view of the benefits in terms of accuracy. Overall, it was found that the conservation of rest mass is improved of a factor ~ 5 , but also that the variance in other relevant quantities, such as the total mass of the ejecta and the time of collapse of the binary-merger product, depends sensibly on other factors that are far more difficult to control, e.g., the specific grid setup or the treatment of the atmosphere, in addition to the EOS.

The impressive investigation work by Reisswig et al. [514], also contained two additional new contributions to the use of advanced techniques to study BNS merger. The first one is the implementation in relativistic hydrodynamics of adapted curvilinear grids, called *multipatches* or *multiblocks*, coupled with flux-conservative, cell-centered adaptive mesh refinement. The idea is to cover the simulation domain with multiple curvilinear coordinate *patches*. Each patch is locally uniform, and diffeomorphic mappings from local to global coordinates enable the representation of a wide range of grid shapes in different regions of the simulation. The most common and useful setup here consists of a central Cartesian patch (for resolving the aspherical region of coalescence and merger) surrounded by six *inflated-cube* spherical grid patches. Multiblocks are useful in many different ways [514]: (i) it is possible to set the outer boundary very far, enough for it to be causally

disconnected from the interior evolution and the gravitational-wave extraction zone, thus avoiding systematic errors from the approximate and non-constraint-preserving outer-boundary condition; (ii) it is possible to track the ejected material out to large radii with relatively high resolution; (iii) the number of mesh-refinement levels can be decreased without reducing the resolution, leading to better parallel scaling.

The second important contribution by Reisswig et al. [514] is the first application in the context of BNS mergers of Cauchy-characteristic extraction (see Ref. [515] for a review) for gravitational-wave extraction at future null infinity. The characteristic formulation takes spacetime as foliated into a sequence of null cones emanating from a central geodesic. This approach has the advantage that the Einstein equations can be compactified so that future null infinity is rigorously represented on a finite grid, and there is no artificial outer boundary condition. However, it suffers from the disadvantage that the coordinates are based on light rays, which can be focused by a strong field to form caustics, which complicate a numerical computation [516]. Cauchy-characteristic extraction is capable of determining the gravitational radiation content unambiguously and without finite-radius and gauge errors. The combined use of causally disconnected outer boundaries and the application of Cauchy-characteristic gravitational-wave extraction allowed Reisswig et al. [514] to extract higher orders than the $\ell = 2 = m$ gravitational-wave mode, obtaining non-negligible signals up to $\ell = 6$ (see the right panel of Fig. 31).

D. Alternative theories of gravity

Building up on previous analytical studies within the post-Newtonian approximation on the dynamics and gravitational-wave emission from BNSs in scalar-tensor theories (see, e.g., Refs. [517–520]) a number of recent numerical-relativity investigations have addressed the problem of BNS mergers in gravitational theories alternative to general relativity [191, 307, 372, 521–523]. The efforts are concentrated on scalar-tensor theories of gravity [518, 524, 525], where the gravitational interaction is mediated by a scalar degree of freedom, in addition to the usual tensor one. Such theories have received much attention, because the presence of a scalar field in nature is motivated by, e.g., the low-energy limit of string theories, the observation of the Higgs boson, and cosmological phenomenology (see Refs. [518, 526] for reviews).

The parameters of scalar-tensor theories are constrained by solar-system experiments and binary-pulsars observations [527, 528], but even if such constraints are satisfied, significant differences from the predictions of general relativity could be observable in stronger gravity regimes. In particular, strong-field aspects of the dynamics of BNSs in scalar-tensor theories, e.g., late-inspirals, mergers, and post-merger phases, can show large deviations from general relativity, which cannot be captured accurately by weak-field analyses [521] and cannot be reproduced within general relativity, e.g., via exotic EOSs. Although the scalar field is only weakly coupled, it carries energy away from the source, exerting a significant back-reaction that could leave an imprint in the gravitational waves, detectable with Advanced LIGO/Virgo [307, 521–523, 529] (see Fig. 32). In practice, for some values of the parameters of the theory, neutron stars of a given mass and EOS may merge at significantly lower frequency than in general relativity [521]. A faster orbital decay may happen also because, in an unequal-mass binary, the system would emit also dipolar radiation due to the scalar field [521, 526, 530]. Such additional decay, as well as the existence of dipole radiation, scalarisation, and the magnitude of the parameters of the theory, are rather stringently constrained by binary-pulsars observations [527, 528], which however do not probe regions of the space of parameters relative to fields as strong as those occurring in the late inspiral of the binary.

Since the scalar charge of a compact object depends on the gravitational binding energy (or compactness) of the object itself, a neutron star can undergo a *spontaneous scalarisation* if it becomes

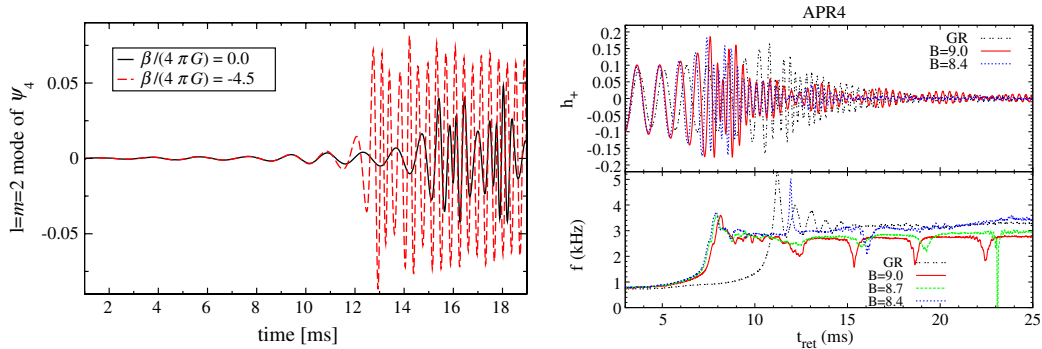


FIG. 32. *Left panel:* The dominant mode of the gravitational wave for an equal-mass binary with individual rest masses of $1.625M_{\odot}$. [Reprinted with permission from Ref. [521]. © (2013) by the American Physical Society.] *Right panel:* Plus-polarization of gravitational waves observed along the axis perpendicular to the orbital plane and their frequency as functions of the retarded time for simulations of BNSs of total rest mass $M = 2.7M_{\odot}$ with the APR4 EOS [Reprinted with permission from Ref. [307]. © (2014) by the American Physical Society.] In both panels, the results for general relativity are compared with the waves obtained in scalar-tensor theory, with different values of the free parameter (β on the left and B on the right; $B = -2\beta$).

compact enough (and for some values of the parameters of the scalar-tensor theory). That is, it can acquire a scalar field from an initial state where scalar fields were absent, since the scalarised configuration represents a lower-energy state [526, 530]. Furthermore, if the star is in a binary, the orbital binding energy of the binary system contributes to the scalarisation, and this process is referred to as *dynamical scalarisation* [521]. Dynamical scalarisation may also happen after the onset of the merger, if a more compact neutron star is formed [307]. Finally, once a star in a binary acquires a scalar charge, it can also scalarise its binary companion, through a process that is referred to as *induced scalarisation* [521]).

By modelling the early plunge through a toy model based on a simple EOS and employing Markov-Chain Monte-Carlo techniques, Sampson et al. [523] studied whether deviations from general relativity in gravitational-wave signals that are caused by a certain class of scalar-tensor theories can be detected with advanced detectors and found that this is the case for the standard projected sensitivity of the detectors, if the stars are sufficiently compact. However, not all scalarisation effects are easily detectable, so that dynamical scalarisation in the late inspiral of BNSs will be difficult to constrain with gravitational-wave observations, unless the system scalarises at a low enough orbital frequency (i.e., large enough orbital separation) that a sufficient amount of SNR is accumulated while the scalar-tensor modifications are active.

The first fully nonlinear numerical simulations of BNSs in scalar-tensor theories were performed by Barausse et al. [521] and were rapidly followed by those of Shibata et al. [307], who found similar results, but through more sophisticated and detailed simulations. Such simulations employed initial conditions from quasi-equilibrium configurations that consistently include also the scalar field, realistic EOSs (Barausse et al. [521] employed a polytropic EOS), and free parameters of the theory chosen taking into account the constraints imposed by the latest observations of neutron-star–white-dwarf binaries with pulsar timing. We note that while the simulations performed by Barausse et al. [521] employed the so-called “Einstein frame”, those of Shibata et al. [307] adopted the so-called “Jordan frame” (the results of Barausse et al. [521] are however expressed in the Jordan frame).

We should note that in both sets of simulations, the values chosen for the parameters of the scalar

field (and in particular the signs of such parameters) are compatible with solar system experiments, but only if the scalar field is assumed to have a mass in some specific range, namely with a Compton wavelength between kilometres and the Hubble scale [523, 531]. This assumption does not affect the results of simulations which are relative to much smaller lengthscales, but it remains an assumption.

Shibata et al. [307] also extended the study to the merger and post-merger phases and emphasized that also the evolution of the remnant neutron star in scalar-tensor theories may be quantitatively different from that predicted by general relativity, because, when the remnant is scalarised, the compactness is different from the one computed in general relativity, and thus the frequency of the quasi-periodic stellar oscillations and so of the gravitational waves is also different. Such a difference depends on the EOS. Shibata et al. [307] underline that the possibility (studied in many works [219, 266, 267, 269, 289, 295–297, 303]) to constrain the EOS of neutron stars by observing the frequency of post-merger quasi-periodic gravitational waves emitted by the binary-merger product may be compromised by the degeneracy introduced by scalar-tensor theories, since the frequency of such gravitational-wave emission depends also on the degree of scalarisation.

Taniguchi et al. [191], then, used quasi-equilibrium sequences, computing equal-mass, irrotational BNSs in scalar-tensor theory and with realistic EOSs (approximated as piecewise polytropes). These quasi-equilibrium sequences were used to compute the dependence of the binary scalar charge and binding energy on the orbital angular frequency and found that the absolute value of the binding energy is smaller than in general relativity, at most by 14%. It was also noted that dynamical scalarisation can yield a different number of gravitational-wave cycles prior to merger and that such a difference is much larger than the effect due to tidal interactions, which is of the order of a few gravitational-wave cycles at most.

There has been some debate on whether in order to compute the dynamics and the waveforms accurately enough it is necessary to solve consistently the initial data problem for configurations in which the scalar field is consistently taken into account as opposed to configurations in which the scalar field develops dynamically during the evolution (the initial data for such configurations without scalar field is of course consistently solved in all of the cited works). On the one side, in Refs. [521, 523] it is stated that even for such configurations the error introduced by neglecting the scalar field at the initial time is negligible; this conclusion is based also on the fact that the results of Refs. [521, 523] were later reproduced analytically in the post-Newtonian approximation [522, 532] (see below). On the other side, in Ref. [191] it is claimed that inaccurate initial data may cause artefacts in the dynamical evolution of the binary system, like a plunge more rapid than in general relativity, as reported in Refs. [521, 523] and not observed in Refs. [191, 307]. It should also be noted that the considerations made in Ref. [191] may be limited by the fact that they refer to equilibrium configurations and do not involve evolutions. Further work is needed to clarify the issue.

As mentioned above, Palenzuela et al. [522] have made computations with an improved post-Newtonian orbital-evolution technique, interfaced with a set of nonlinear algebraic equations that provide a description of the scalar charge (see also Ref. [532] for an improved approach using a resummed post-Newtonian expansion). After validating this semi-analytical procedure by comparing results to those of fully general-relativistic simulations, they investigated the behavior of BNSs prior to merger, exploring large portions of the parameter space of scalar-tensor theories and including equal-mass, unequal-mass, and eccentric BNS systems. This simplified model also allows for an efficient generation of templates of waveforms within scalar-tensor theories, for the exploration of possible degeneracies, and for the investigation of the extent to which existing data-analysis techniques can be exploited to test gravity theories alternative to general relativity.

Finally, Ponce et al. [372] examined whether the characteristics of the prompt electromagnetic counterparts (see Sect. VIA 3) to BNS systems can provide an independent way to test gravity in the strong-field regime. In particular, they found that in some cases the electromagnetic emission during

the inspiral in scalar-tensor theories may show deviations from the prediction of general relativity. These differences are quite small and so very accurate measurements are required to differentiate between general relativity and scalar-tensor theories when using electromagnetic observations alone; of course, a multimessenger signal would provide far more stringent constraints.

E. Relativistic collisions

We conclude this Chapter and review with a topic that still involves pairs of neutron stars, although under rather unusual circumstances, namely, through their head-on collision when they are boosted to relativistic speeds. Hence, this is not quite the type of BNS “merger” discussed so far, although it still involves the merger of two neutron stars.

Much of the interest in the collision of two neutron stars moving at relativistic speeds obviously stems from the possibility of using this system to study, in a controlled numerical environment, the conditions that may lead to black-hole formation, and, in particular, from the interest in extending to a more dynamical context Thorne’s *hoop conjecture* [533]. We recall that the hoop conjecture casts in rather loose terms the conditions for black-hole formation by stating that a black hole will be formed if an object of mass (energy) M is confined in a volume that in all directions (hence the word *hoop*) has a radius $R \leq 2M$. While somewhat obvious, this conjecture does not distinguish the amount of energy in M that could be of kinetic nature. It is not difficult, in fact, to imagine that the collision of two compact objects of mass $M/2$ when in isolation, could or could not lead to the formation of a black hole depending on the amount of kinetic energy they possess at the time of the collision [534, 535].

These considerations are not entirely academic and were spurred by the first operations of the Large Hadron Collider at CERN. Indeed, after applying the conjecture to particles, one finds that the threshold for black-hole formation occurs at Planck energy scales. However, some theories of quantum gravity with small or warped extra dimensions [536–539] predict that the energy required for black-hole formation might be significantly smaller than the Planck scale [537]. In this case, proton collisions at the Large Hadron Collider (LHC) [540], or collisions of cosmic rays with the Earth’s atmosphere [541], may become relevant to the formation of microscopic black holes. To date, however, no evidence for black-hole formation in these events has been found [542].

Also with this in mind, Rezzolla and Takami [543], expanding on their previous work [545–547], studied black-hole formation from the ultrarelativistic head-on collision of two neutron stars. They performed simulations that improve several aspects of previous work [534, 535]. In particular, their colliding objects are not treated as point particles or scalar fields, but rather as extended and self-gravitating fluid objects, thus representing a more realistic description of the baryonic matter involved in ultra-relativistic heavy-ion collisions. Their results confirmed that the collision of two self-gravitating objects gives rise to a type-I critical behaviour [545–550]³⁴, with a black hole being produced for masses above a critical value M_c and a partially bound object for masses below M_c .

Interestingly, the critical value depends on the Lorentz factor of the colliding stars, so that increasingly smaller masses are needed to produce a black hole when the stars are boosted to larger and larger velocity. The location of this critical line in the $(M, \langle\gamma\rangle)$ plane is expressed by the simple relation $M_c/M_\odot \approx 0.92 \langle\gamma\rangle^{-1.03}$, where $\langle\gamma\rangle$ is the average Lorentz factor of the boosted stars [543] (see left panel of Fig. 33). This expression essentially states the conservation of energy, but also that in the limit of zero initial velocities, i.e., $\langle\gamma\rangle \rightarrow 1$, twice the critical mass is slightly larger than the

³⁴ In analogy with first- and second-order phase transitions in statistical mechanics, critical phenomena characterised by a finite mass at the black-hole-formation threshold are called type I, while the critical phenomena with a power-law scaling of such mass are called type II [551].

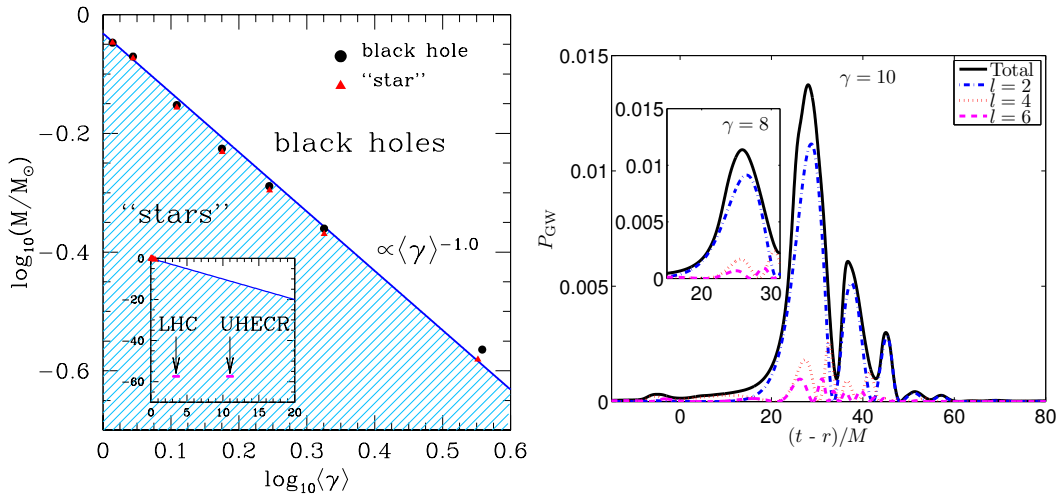


FIG. 33. *Left panel:* Critical line as a function of the effective Lorentz factor; here circles indicate black holes, while triangles self-gravitating partially bound objects. [From Ref. [543] © IOP Publishing. Reproduced with permission. All rights reserved.] *Right panel:* Total and spin-weight 2 spherical harmonic decomposition of the power in gravitational waves from a collision with $\langle \gamma \rangle = 10$ (the inset shows a case with $\langle \gamma \rangle = 8$). Only the power for $t - r > 0$ is accounted for in the estimate of the emitted energy. [Reprinted with permission from Ref. [544]. © (2013) by the American Physical Society.]

maximum mass of the relative spherical-star sequence, i.e., $2M_c \simeq 1.12 M_{\text{TOV}} \simeq 1.12 \times 1.637 M_{\odot}$ for the EOS considered. In the opposite limit of $\langle \gamma \rangle \rightarrow \infty$, the expression above predicts that the critical mass will go zero: as the kinetic energy diverges, no room is left for selfgravitating matter, which will all be ejected but for an infinitesimal amount that will go into building the zero-mass critical black hole. While the precise numbers reported in Ref. [543] refer to a given choice of the EOS, it is claimed that the same behaviour should hold qualitatively for all EOSs.

Returning to the hoop conjecture, Rezzolla and Takami [543] showed that the presence of a critical line can also be cast as a condition on a critical compactness, i.e., it can be expressed as $2M_{\text{lab}}/R \simeq 0.16 \langle \gamma \rangle^{-0.13}$, where $M_{\text{lab}} := \langle \gamma \rangle M$ is the mass in the lab frame and R is the largest dimension in that frame being transverse to the motion. Stated differently, two colliding self-gravitating systems moving with an average boost of $\langle \gamma \rangle$ will produce a black hole if the transverse compactness is $\simeq 0.08/\langle \gamma \rangle^{0.13}$. This extends the static hoop conjecture to a dynamical framework [543].

At about the same time when the results above were published, East and Pretorius [544] took further the investigation by exploring significantly higher-boost collisions where the ratio of kinetic to rest mass energy is of order 10 : 1, although for a more restricted range of masses. East and Pretorius [544] found that the threshold for black-hole formation is a factor of a few less than the estimate of the hoop conjecture. A new and interesting phenomenon was also presented, namely that for boosts slightly above the threshold, two separate apparent horizons form shortly after the collision and then some time later are encompassed by a single horizon that rings down to a Schwarzschild black hole. This is qualitatively explained as due to the strong focusing of the fluid elements of one star by the boosted spacetime of the other, and viceversa. Finally, East and Pretorius [544] were able to measure for the first time the gravitational-wave emission generated by the collision, finding that up to $16 \pm 2\%$ of the total energy of spacetime is radiated via gravitational waves (see right panel of

Fig. 33).

VIII. SUMMARY AND OUTLOOK

As anticipated in the Introduction, there is little doubt that this is a particularly exciting and highly dynamical time for research on neutron stars, in general, and on BNS mergers, in particular. In less than 10 years, i.e., starting approximately from 2008, a considerable effort by several groups across the world has obtained numerous important results about the dynamics of binary systems of neutron stars, employing a large variety of numerical (in most cases) and analytical (in a few cases) techniques and exploring this process with different degrees of approximation and realism.

Altogether, these works have revealed that the merger of a binary system of neutron stars is a marvellous physical laboratory. Indeed, BNS mergers are expected to be behind several fascinating physical processes, which we recall here: (i) they are significant sources of gravitational radiation; (ii) they could act as possible progenitors for short-gamma-ray bursts (SGRBs); (iii) they have the potential to produce electromagnetic and neutrino emission that is visible from enormous distances; (iv) they are likely responsible for the production of a good portion (if not all) of the very heavy elements in the Universe. When viewed across this lens, it is quite natural to consider BNS mergers as Einstein’s richest laboratory, binding in the same environment highly nonlinear gravitational dynamics with complex microphysical processes and astonishing astrophysical phenomena.

The huge progress accomplished over the last ten years has helped trace a broadbrush picture of BNS mergers that has several sound aspects, among which the most robust in our opinion are the following ones:³⁵

- Independently of the fine details of the EOS, of the mass ratio or of the presence of magnetic fields, the merger of a binary system of neutron stars eventually leads to a rapidly rotating black hole with dimensionless spin $J/M^2 \simeq 0.7 - 0.8$ surrounded by a hot accretion torus with mass in the range $M_{\text{torus}} \sim 0.001 - 0.1 M_{\odot}$. Only very low-mass progenitors whose total mass is below the maximum mass of a (nonrotating) neutron star would not produce a black hole. It is unclear whether such progenitors are statistically important.
- The complete gravitational-wave signal from inspiralling and merging BNSs can be computed numerically with precision that is smaller but overall comparable with that available for black holes.
- When considering the inspiral-only part of the gravitational-wave signal, semi-analytical approximations either in the post-Newtonian or EOB approximation, can reproduce the results of numerical-relativity calculations essentially up to the merger.
- The gravitational-wave spectrum is marked by precise frequencies, either during the inspiral or after the merger that exhibit a “quasi-universal” behaviour. In other words, while the position of the peaks depends on the EOS, it can be easily factored out to obtain EOS-independent relations between the frequencies of the peaks and the properties of the progenitor stars.
- The result of the merger, i.e., the binary-merger product, is a highly massive and differentially rotating neutron star. The lifetime of the binary-merger product depends on a number of factors, including the mass of the progenitors, their mass ratio and EOS, as well as the role played by magnetic fields and neutrino losses. While sufficiently large initial masses can yield a prompt collapse at the merger, smaller masses can lead to a binary-merger product surviving hundreds of seconds and possibly more.

³⁵ In this Section we will intentionally omit references to avoid cluttering the text; all the relevant references can be found in the various Sections covering the topics discussed here.

- When considering magnetic fields of realistic strengths endowing the stars prior to the merger, the correction imprinted by them on the gravitational-wave signal during the inspiral are too small to be detected from advanced gravitational-wave detectors. Electromagnetic signals could be produced before the merger, but these are probably too weak to be detected from cosmological distances.
- Magnetic fields are expected to be amplified both at the merger (via Kelvin-Helmholtz instability), after it and before the collapse and after the formation of a black-hole–torus system (in all cases via a magnetorotational instability or a dynamo action converting small-scale fields into large-scale ones). The final and effective amplification of the resulting magnetic fields is still uncertain, although it should be of at least two-three orders of magnitude.
- The interaction of amplified magnetic fields and accretion in the black-hole–torus system leads to the formation of a magnetically confined plasma along the polar directions of the black hole. Under suitable conditions, the plasma in this funnel may be launched to ultrarelativistic speeds (still unobserved in simulations).
- Matter is expected to be ejected both at the merger and subsequently as a result of a combination of processes: tidal and dynamical mass ejection, magnetically driven winds, neutrino-driven winds, shock-heating winds. Overall, the matter ejected from binaries in quasi-circular orbits amounts to $M_{\text{ejected}} \sim 0.001 - 0.01 M_{\odot}$, while binaries in eccentric orbits can yield up to one order of magnitude more.
- The ejected and unbound matter is expected to undergo nuclear transformations that are mediated by the emission and absorption of neutrinos. Rapid neutron-capture processes (*r*-processes) will then lead to nucleosynthetic yields that are insensitive to input physics or merger type in the regions of the second and third *r*-process peaks, matching the Solar abundances surprisingly well. However, first-peak elements are difficult to explain without invoking contributions from either neutrino and viscously-driven winds operating on longer timescales after the merger, or from core-collapse supernovae.
- The radioactive decay of the ejected matter or its interaction with the interstellar medium are likely to yield afterglows in the infrared or radio bands that are expected to follow the merger after timescales that go from several days to years.

Note that many of the aspects listed above are robust but have been addressed mostly at a rather qualitative level, with precisions that range from “a-factor-of-a-few” up to “order-of-magnitude” estimates. Furthermore, these results can be seen as the low-hanging fruits of a tree that still has a number of results to offer, although these will require an equal, if not larger, investments of effort, microphysical and numerical developments, and, of course, of computer time. Among the most pressing and exciting open issues we certainly list the following ones:

- Consistent initial data for magnetised and arbitrarily spinning neutron-star binaries.
- Semi-analytical and faithful description of the complete gravitational-wave signal, from the inspiral to the formation of a black-hole or stable neutron star.
- Robust and accurate estimate of the critical mass to prompt collapse and of the survival time of the binary-merger product.
- Robust and accurate estimate of the processes mediating the accretion of the torus formed around the black hole, hence obtaining reliable measurements of the timescale for accretion.

- Assessment of the role that turbulence and instabilities play in the amplification of the progenitor magnetic field and determination of the final strengths to be expected.
- Robust and accurate sub-grid modelling for a realistic simulation of the magnetic-field dynamics at the smallest scales.
- Assessment of a possible dynamo action occurring in a long-lived binary-merger product and leading to the generation of an ordered and large-scale magnetic field.
- Determination of the microphysical processes leading to the formation and launching of an ultra-relativistic jet.
- Determination of the acceleration sites of charged particles to ultrarelativistic energies and calculation of the energy distribution functions.
- Determination of the role played by neutrino losses in launching the jet and in modifying the chemical composition of the ejected material.
- Determination of the relative importance of dynamical tidal torques, magnetic unbalance, neutrino emission, or shock heating, for the ejection of matter from the system.
- Robust and accurate determination of the physical and chemical properties of material ejected from the whole merger process.
- Quantitative and accurate predictions of the electromagnetic signal produced by the merger, either directly or indirectly as afterglows.

In conclusion, if the first direct detection of the gravitational-wave signals from binary systems of black holes has officially given birth to the era of gravitational-wave astronomy and has, once again, emphasised general relativity as the best theory of gravitation known, the huge advances that are expected to come in the next few years on the physics and astrophysics of BNSs will help lift many of the veils that still cover Einstein’s richest laboratory.

ACKNOWLEDGEMENTS

Writing this review has been an effort we have diluted over a couple of years, during which it has been continuously updated as new results were produced and additional progress was made. We are indebted to the numerous friends and colleagues that have provided useful input and have helped us obtaining a review that is as complete and detailed as we could possibly have written. Special thanks go to E. Barausse, L. Bovard, R. De Pietri, N. Stergioulas, K. Taniguchi, A. Tsokaros, and S. Wanajo and for useful input on this review and to D. Alic, K. Dionysopoulou, T. Font, F. Guercilena, M. Hanauske, B. Mundim, and K. Takami for uncountable discussions.

Partial support has come from “NewCompStar”, COST Action MP1304, from the LOEWE-Program in HIC for FAIR, the European Union’s Horizon 2020 Research and Innovation Programme under grant agreement No. 671698 (call FETHPC-1-2014, project ExaHyPE), from the ERC Synergy Grant “BlackHoleCam - Imaging the Event Horizon of Black Holes” (Grant 610058), and from JSPS Grant-in-Aid for Scientific Research(C) No. 26400274.

-
- [1] M. Kramer, A. Lyne, M. Burgay, A. Possenti, R. Manchester, F. Camilo, M. McLaughlin, D. Lorimer, N. D'Amico, B. Joshi, J. Reynolds, and P. Freire, in *Binary Pulsars*, edited by Rasio and Stairs (PSAP, Chicago, 2004).
- [2] B. Kiziltan, A. Kottas, M. De Yoreo, and S. E. Thorsett, *Astrophys. J.* **778**, 66 (2013), arXiv:1011.4291 [astro-ph.GA].
- [3] N. Ivanova, S. Justham, X. Chen, O. De Marco, C. L. Fryer, E. Gaburov, H. Ge, E. Glebbeek, Z. Han, X.-D. Li, G. Lu, T. Marsh, P. Podsiadlowski, A. Potter, N. Soker, R. Taam, T. M. Tauris, E. P. J. van den Heuvel, and R. F. Webbink, *Astronomy and Astrophysics Reviews* **21**, 59 (2013), arXiv:1209.4302 [astro-ph.HE].
- [4] F. Özel and P. Freire, *Annual Review of Astronomy and Astrophysics* **54**, 401 (2016), arXiv:1603.02698 [astro-ph.HE].
- [5] R. M. O'Leary, B. Kocsis, and A. Loeb, *Mon. Not. R. Astron. Soc.* **395**, 2127 (2009), arXiv:0807.2638.
- [6] W. H. Lee, E. Ramirez-Ruiz, and G. van de Ven, *Astrophys. J.* **720**, 953 (2010), arXiv:0909.2884 [astro-ph.HE].
- [7] T. A. Thompson, *Astrophys. J.* **741**, 82 (2011), arXiv:1011.4322 [astro-ph.HE].
- [8] J. G. Martinez, K. Stovall, P. C. C. Freire, J. S. Deneva, F. A. Jenet, M. A. McLaughlin, M. Bagchi, S. D. Bates, and A. Ridolfi, *Astrophys. J.* **812**, 143 (2015), arXiv:1509.08805 [astro-ph.HE].
- [9] M. Kramer, I. H. Stairs, R. N. Manchester, M. A. McLaughlin, A. G. Lyne, R. D. Ferdman, M. Burgay, D. R. Lorimer, A. Possenti, N. D'Amico, J. M. Sarkissian, G. B. Hobbs, J. E. Reynolds, P. C. C. Freire, and F. Camilo, *Science* **314**, 97 (2006), astro-ph/0609417.
- [10] G. H. Janssen, B. W. Stappers, M. Kramer, D. J. Nice, A. Jessner, I. Cognard, and M. B. Purver, *Astron. Astrophys.* **490**, 753 (2008), arXiv:0808.2292.
- [11] E. Fonseca, I. H. Stairs, and S. E. Thorsett, *Astrophys. J.* **787**, 82 (2014), arXiv:1402.4836 [astro-ph.HE].
- [12] M. J. Keith, M. Kramer, A. G. Lyne, R. P. Eatough, I. H. Stairs, A. Possenti, F. Camilo, and R. N. Manchester, *Mon. Not. R. Astron. Soc.* **393**, 623 (2009), arXiv:0811.2027.
- [13] R. D. Ferdman, I. H. Stairs, M. Kramer, G. H. Janssen, C. G. Bassa, B. W. Stappers, P. B. Demorest, I. Cognard, G. Desvignes, G. Theureau, M. Burgay, A. G. Lyne, R. N. Manchester, and A. Possenti, *Mon. Not. R. Astron. Soc.* **443**, 2183 (2014), arXiv:1406.5507 [astro-ph.SR].
- [14] R. S. Lynch, P. C. C. Freire, S. M. Ransom, and B. A. Jacoby, *Astrophys. J.* **745**, 109 (2012), arXiv:1112.2612 [astro-ph.HE].
- [15] A. Corongiu, M. Kramer, B. W. Stappers, A. G. Lyne, A. Jessner, A. Possenti, N. D'Amico, and O. Löhmer, *Astron. Astrophys.* **462**, 703 (2007), astro-ph/0611436.
- [16] D. J. Champion, D. R. Lorimer, M. A. McLaughlin, J. M. Cordes, Z. Arzoumanian, J. M. Weisberg, and J. H. Taylor, *Mon. Not. R. Astron. Soc.* **350**, L61 (2004), astro-ph/0403553.
- [17] J. van Leeuwen, L. Kasian, I. H. Stairs, D. R. Lorimer, F. Camilo, S. Chatterjee, I. Cognard, G. Desvignes, P. C. C. Freire, G. H. Janssen, M. Kramer, A. G. Lyne, D. J. Nice, S. M. Ransom, B. W. Stappers, and J. M. Weisberg, *Astrophys. J.* **798**, 118 (2015), arXiv:1411.1518 [astro-ph.SR].
- [18] P. Lazarus, P. C. C. Freire, B. Allen, C. Aulbert, O. Bock, S. Bogdanov, A. Brazier, F. Camilo, F. Cardoso, S. Chatterjee, J. M. Cordes, F. Crawford, J. S. Deneva, H.-B. Eggenstein, H. Fehrmann, R. Ferdman, J. W. T. Hessels, F. A. Jenet, C. Karako-Argaman, V. M. Kaspi, B. Knispel, R. Lynch, J. van Leeuwen, B. Machenschalk, E. Madsen, M. A. McLaughlin, C. Patel, S. M. Ransom, P. Scholz, A. Seymour, X. Siemens, L. G. Spitler, I. H. Stairs, K. Stovall, J. Swiggum, A. Venkataraman, and W. W. Zhu, *Astrophys. J.* **831**, 150 (2016), arXiv:1608.08211 [astro-ph.HE].
- [19] J. M. Weisberg and Y. Huang, *Astrophys. J.* **829**, 55 (2016), arXiv:1606.02744 [astro-ph.HE].
- [20] J. K. Swiggum, R. Rosen, M. A. McLaughlin, D. R. Lorimer, S. Heatherly, R. Lynch, S. Scoles, T. Hockett, E. Filik, J. A. Marlowe, B. N. Barlow, M. Weaver, M. Hilzendeger, S. Ernst, R. Crowley, E. Stone, B. Miller, R. Nunez, G. Trevino, M. Doehler, A. Cramer, D. Yencsik, J. Thorley, R. Andrews, A. Laws, K. Wenger, L. Teter, T. Snyder, A. Dittmann, S. Gray, M. Carter, C. McGough, S. Dydiw, C. Pruetz, J. Fink, and A. Vanderhout, *Astrophys. J.* **805**, 156 (2015), arXiv:1503.06276 [astro-ph.HE].
- [21] B. A. Jacoby, P. B. Cameron, F. A. Jenet, S. B. Anderson, R. N. Murty, and S. R. Kulkarni, *Astrophys. J. Lett.* **644**, L113 (2006), astro-ph/0605375.

- [22] G. M. Harry *et al.*, *Class. Quantum Grav.* **27**, 084006 (2010).
- [23] The LIGO Scientific Collaboration and the Virgo Collaboration, *Phys. Rev. Lett.* **116**, 061102 (2016), [arXiv:1602.03837 \[gr-qc\]](#).
- [24] B. P. Abbott, R. Abbott, T. D. Abbott, M. R. Abernathy, F. Acernese, K. Ackley, C. Adams, T. Adams, P. Addesso, R. X. Adhikari, and et al., *Physical Review Letters* **116**, 241103 (2016), [arXiv:1606.04855 \[gr-qc\]](#).
- [25] T. Accadia *et al.*, *Class. Quantum Grav.* **28**, 114002 (2011).
- [26] Y. Aso, Y. Michimura, K. Somiya, M. Ando, O. Miyakawa, T. Sekiguchi, D. Tatsumi, and H. Yamamoto, *Phys. Rev. D* **88**, 043007 (2013), [arXiv:1306.6747 \[gr-qc\]](#).
- [27] S. Fairhurst, *Journal of Physics Conference Series* **484**, 012007 (2014), [arXiv:1205.6611 \[gr-qc\]](#).
- [28] J. Abadie *et al.*, *Class. Quantum Grav.* **27**, 173001 (2010), [arXiv:1003.2480 \[astro-ph.HE\]](#).
- [29] R. Narayan, B. Paczynski, and T. Piran, *Astrophysical Journal, Letters* **395**, L83 (1992), [astro-ph/9204001](#).
- [30] D. Eichler, M. Livio, T. Piran, and D. N. Schramm, *Nature* **340**, 126 (1989).
- [31] M. Shibata and K. Uryū, *Phys. Rev. D* **61**, 064001 (2000), [gr-qc/9911058](#).
- [32] L. Baiotti, B. Giacomazzo, and L. Rezzolla, *Phys. Rev. D* **78**, 084033 (2008), [arXiv:0804.0594 \[gr-qc\]](#).
- [33] M. Anderson, E. W. Hirschmann, L. Lehner, S. L. Liebling, P. M. Motl, D. Neilsen, C. Palenzuela, and J. E. Tohline, *Phys. Rev. D* **77**, 024006 (2008), [arXiv:0708.2720 \[gr-qc\]](#).
- [34] Y. T. Liu, S. L. Shapiro, Z. B. Etienne, and K. Taniguchi, *Phys. Rev. D* **78**, 024012 (2008), [arXiv:0803.4193 \[astro-ph\]](#).
- [35] S. Bernuzzi, M. Thierfelder, and B. Brügmann, *Phys. Rev. D* **85**, 104030 (2012), [arXiv:1109.3611 \[gr-qc\]](#).
- [36] B. Margalit, B. D. Metzger, and A. M. Beloborodov, *Phys. Rev. Lett.* **115**, 171101 (2015), [arXiv:1505.01842 \[astro-ph.HE\]](#).
- [37] B. Paczynski, *Astrophys. J. Lett.* **308**, L43 (1986).
- [38] C. Palenzuela, L. Lehner, M. Ponce, S. L. Liebling, M. Anderson, D. Neilsen, and P. Motl, *Phys. Rev. Lett.* **111**, 061105 (2013), [arXiv:1301.7074 \[gr-qc\]](#).
- [39] L. Rezzolla, B. Giacomazzo, L. Baiotti, J. Granot, C. Kouveliotou, and M. A. Aloy, *Astrophys. J. Letters* **732**, L6 (2011), [arXiv:1101.4298 \[astro-ph.HE\]](#).
- [40] V. Paschalidis, M. Ruiz, and S. L. Shapiro, *Astrophys. J. Lett.* **806**, L14 (2015), [arXiv:1410.7392 \[astro-ph.HE\]](#).
- [41] K. Dionysopoulou, D. Alic, and L. Rezzolla, *Phys. Rev. D* **92**, 084064 (2015), [arXiv:1502.02021 \[gr-qc\]](#).
- [42] M. Ruiz, R. N. Lang, V. Paschalidis, and S. L. Shapiro, *Astrophys. J. Lett.* **824**, L6 (2016), [arXiv:1604.02455 \[astro-ph.HE\]](#).
- [43] E. Berger, W. Fong, and R. Chornock, *Astrophys. J.* **774**, L23 (2013), [arXiv:1306.3960 \[astro-ph.HE\]](#).
- [44] N. R. Tanvir, A. J. Levan, A. S. Fruchter, J. Hjorth, R. A. Hounsell, K. Wiersema, and R. L. Tunnicliffe, *Nature* **500**, 547 (2013), [arXiv:1306.4971 \[astro-ph.HE\]](#).
- [45] L.-X. Li and B. Paczyński, *Astrophys. J.* **507**, L59 (1998), [astro-ph/9807272](#).
- [46] S. R. Kulkarni, [astro-ph/0510256](#) (2005), [astro-ph/0510256](#).
- [47] B. D. Metzger, G. Martínez-Pinedo, S. Darbha, E. Quataert, A. Arcones, D. Kasen, R. Thomas, P. Nugent, I. V. Panov, and N. T. Zinner, *Mon. Not. R. Astron. Soc.* **406**, 2650 (2010), [arXiv:1001.5029 \[astro-ph.HE\]](#).
- [48] B. Yang, Z.-P. Jin, X. Li, S. Covino, X.-Z. Zheng, K. Hotokezaka, Y.-Z. Fan, T. Piran, and D.-M. Wei, *Nature Communications* **6**, 7323 (2015), [arXiv:1503.07761 \[astro-ph.HE\]](#).
- [49] Z.-P. Jin, K. Hotokezaka, X. Li, M. Tanaka, P. D'Avanzo, Y.-Z. Fan, S. Covino, D.-M. Wei, and T. Piran, *Nature Communications* **7**, 12898 (2016), [arXiv:1603.07869 \[astro-ph.HE\]](#).
- [50] Z.-P. Jin, X. Li, Z. Cano, S. Covino, Y.-Z. Fan, and D.-M. Wei, *Astrophys. J. Lett.* **811**, L22 (2015), [arXiv:1507.07206 \[astro-ph.HE\]](#).
- [51] A. Wallner, T. Faestermann, J. Feige, C. Feldstein, K. Knie, G. Korschinek, W. Kutschera, A. Ofan, M. Paul, F. Quinto, G. Rugel, and P. Steier, *Nature Communications* **6**, 5956 (2015), [arXiv:1509.08054 \[astro-ph.SR\]](#).
- [52] K. Hotokezaka, T. Piran, and M. Paul, [ArXiv e-prints](#) (2015), [arXiv:1510.00711 \[astro-ph.HE\]](#).
- [53] A. P. Ji, A. Frebel, A. Chiti, and J. D. Simon, [ArXiv e-prints](#) (2015), [arXiv:1512.01558](#).
- [54] R. C. Tolman, *Phys. Rev.* **55**, 364 (1939).

- [55] J. R. Oppenheimer and G. Volkoff, *Phys. Rev.* **55**, 374 (1939).
- [56] J. Antoniadis, P. C. C. Freire, N. Wex, T. M. Tauris, R. S. Lynch, M. H. van Kerkwijk, M. Kramer, C. Bassa, V. S. Dhillon, T. Driebe, J. W. T. Hessels, V. M. Kaspi, V. I. Kondratiev, N. Langer, T. R. Marsh, M. A. McLaughlin, T. T. Pennucci, S. M. Ransom, I. H. Stairs, J. van Leeuwen, J. P. W. Verbiest, and D. G. Whelan, *Science* **340**, 448 (2013), [arXiv:1304.6875 \[astro-ph.HE\]](#).
- [57] P. B. Demorest, T. Pennucci, S. M. Ransom, M. S. E. Roberts, and J. W. T. Hessels, *Nature* **467**, 1081 (2010), [arXiv:1010.5788 \[astro-ph.HE\]](#).
- [58] L. Rezzolla, L. Baiotti, B. Giacomazzo, D. Link, and J. A. Font, *Class. Quantum Grav.* **27**, 114105 (2010), [arXiv:1001.3074 \[gr-qc\]](#).
- [59] L. Rezzolla and O. Zanotti, *Relativistic Hydrodynamics* (Oxford University Press, Oxford, UK, 2013).
- [60] C. Breu and L. Rezzolla, *Mon. Not. R. Astron. Soc.* **459**, 646 (2016), [arXiv:1601.06083 \[gr-qc\]](#).
- [61] M. Shibata, T. W. Baumgarte, and S. L. Shapiro, *Astrophys. J.* **542**, 453 (2000), [astro-ph/0005378](#).
- [62] L. Baiotti, R. de Pietri, G. M. Manca, and L. Rezzolla, *Phys. Rev. D* **75**, 044023 (2007), [astro-ph/0609473](#).
- [63] L. Franci, R. De Pietri, K. Dionysopoulou, and L. Rezzolla, *Journal of Physics Conference Series* **470**, 012008 (2013), [arXiv:1309.6549 \[gr-qc\]](#).
- [64] D. M. Siegel, R. Ciolfi, A. I. Harte, and L. Rezzolla, *Phys. Rev. D* **87**, 121302 (2013), [arXiv:1302.4368 \[gr-qc\]](#).
- [65] K. Kiuchi, K. Kyutoku, Y. Sekiguchi, M. Shibata, and T. Wada, *Phys. Rev. D* **90**, 041502 (2014), [arXiv:1407.2660 \[astro-ph.HE\]](#).
- [66] N. Stergioulas, *Living Rev. Relativ.* **6**, 3 (2003).
- [67] S. Ou and J. E. Tohline, *Astrophys. J.* **651**, 1068 (2006), [astro-ph/0604099](#).
- [68] G. Corvino, L. Rezzolla, S. Bernuzzi, R. De Pietri, and B. Giacomazzo, *Class. Quantum Grav.* **27**, 114104 (2010), [arXiv:1001.5281 \[gr-qc\]](#).
- [69] M. Anderson, E. W. Hirschmann, L. Lehner, S. L. Liebling, P. M. Motl, D. Neilsen, C. Palenzuela, and J. E. Tohline, *Phys. Rev. Lett.* **100**, 191101 (2008), [arXiv:0801.4387 \[gr-qc\]](#).
- [70] V. Paschalidis, W. E. East, F. Pretorius, and S. L. Shapiro, *Phys. Rev. D* **92**, 121502 (2015), [arXiv:1510.03432 \[astro-ph.HE\]](#).
- [71] W. E. East, V. Paschalidis, F. Pretorius, and S. L. Shapiro, *Phys. Rev. D* **93**, 024011 (2016), [arXiv:1511.01093 \[astro-ph.HE\]](#).
- [72] D. Radice, F. Galeazzi, J. Lippuner, L. F. Roberts, C. D. Ott, and L. Rezzolla, *Mon. Not. R. Astron. Soc.* **460**, 3255 (2016), [arXiv:1601.02426 \[astro-ph.HE\]](#).
- [73] L. Lehner, S. L. Liebling, C. Palenzuela, and P. Motl, *ArXiv e-prints* (2016), [arXiv:1605.02369 \[gr-qc\]](#).
- [74] W. Kastaun and F. Galeazzi, *Phys. Rev. D* **91**, 064027 (2015), [arXiv:1411.7975 \[gr-qc\]](#).
- [75] L. Rezzolla and P. Kumar, *Astrophys. J.* **802**, 95 (2015), [arXiv:1410.8560 \[astro-ph.HE\]](#).
- [76] V. Ravi and P. D. Lasky, *Mon. Not. R. Astron. Soc.* **441**, 2433 (2014).
- [77] M. Alcubierre, *Introduction to 3 + 1 Numerical Relativity* (Oxford University Press, Oxford, UK, 2008).
- [78] C. Bona, C. Palenzuela-Luque, and C. Bona-Casas, *Elements of Numerical Relativity and Relativistic Hydrodynamics: From Einstein's Equations to Astrophysical Simulations*, *Lecture Notes in Physics* (Springer, Berlin Heidelberg, 2009).
- [79] T. W. Baumgarte and S. L. Shapiro, *Numerical Relativity: Solving Einstein's Equations on the Computer by Thomas W. Baumgarte and Stuart L. Shapiro*, *Cambridge University Press, 2010*. ISBN: 9780521514071 (Cambridge University Press, Cambridge, UK, 2010).
- [80] E.ourgoulhon, *Lecture Notes in Physics, Berlin Springer Verlag*, *Lecture Notes in Physics*, Berlin Springer Verlag, Vol. 846 (2012).
- [81] M. Shibata, *Numerical Relativity* (World Scientific, Singapore, 2016).
- [82] R. Arnowitt, S. Deser, and C. W. Misner, *Phys. Rev.* **116**, 1322 (1959).
- [83] R. Arnowitt, S. Deser, and C. W. Misner, *General Relativity and Gravitation* **40**, 1997 (2008), [gr-qc/0405109](#).
- [84] T. Nakamura, K. Oohara, and Y. Kojima, *Progress of Theoretical Physics Supplement* **90**, 1 (1987).
- [85] M. Shibata and T. Nakamura, *Phys. Rev. D* **52**, 5428 (1995).
- [86] T. W. Baumgarte and S. L. Shapiro, *Phys. Rev. D* **59**, 024007 (1999), [gr-qc/9810065](#).
- [87] M. Alcubierre, B. Brügmann, T. Dramlitsch, J. A. Font, P. Papadopoulos, E. Seidel, N. Stergioulas, and R. Takahashi, *Phys. Rev. D* **62**, 044034 (2000), [gr-qc/0003071](#).

- [88] M. Alcubierre, B. Brügmann, D. Pollney, E. Seidel, and R. Takahashi, *Phys. Rev. D* **64**, 061501 (2001), [gr-qc/0104020](#).
- [89] M. Alcubierre, B. Brügmann, P. Diener, M. Koppitz, D. Pollney, E. Seidel, and R. Takahashi, *Phys. Rev. D* **67**, 084023 (2003), [gr-qc/0206072](#).
- [90] D. Mueller and B. Brügmann, *Class. Quantum Grav.* **27**, 114008 (2010), [arXiv:0912.3125 \[gr-qc\]](#).
- [91] D. Alic, L. Rezzolla, I. Hinder, and P. Mösta, *Class. Quantum Grav.* **27**, 245023 (2010), [arXiv:1008.2212 \[gr-qc\]](#).
- [92] D. Alic, W. Kastaun, and L. Rezzolla, *Phys. Rev. D* **88**, 064049 (2013), [arXiv:1307.7391 \[gr-qc\]](#).
- [93] S. Bernuzzi and D. Hilditch, *Phys. Rev. D* **81**, 084003 (2010), [arXiv:0912.2920 \[gr-qc\]](#).
- [94] A. Weyhausen, S. Bernuzzi, and D. Hilditch, *Phys. Rev. D* **85**, 024038 (2012), [arXiv:1107.5539 \[gr-qc\]](#).
- [95] Z. Cao and D. Hilditch, *Phys. Rev. D* **85**, 124032 (2012), [arXiv:1111.2177 \[gr-qc\]](#).
- [96] D. Hilditch, S. Bernuzzi, M. Thierfelder, Z. Cao, W. Tichy, and B. Brügmann, *Phys. Rev. D* **88**, 084057 (2013), [arXiv:1212.2901 \[gr-qc\]](#).
- [97] C. Bona, T. Ledvinka, C. Palenzuela, and M. Žáček, *Phys. Rev. D* **67**, 104005 (2003), [gr-qc/0302083](#).
- [98] C. Bona, C. Bona-Casas, and C. Palenzuela, *Phys. Rev. D* **82**, 124010 (2010), [arXiv:1008.0747 \[gr-qc\]](#).
- [99] C. Gundlach, J. M. Martin-Garcia, G. Calabrese, and I. Hinder, *Class. Quantum Grav.* **22**, 3767 (2005), [gr-qc/0504114](#).
- [100] C. Bona, T. Ledvinka, C. Palenzuela, and M. Žáček, *Phys. Rev. D* **69**, 064036 (2004), [gr-qc/0307067](#).
- [101] C. Bona and C. Palenzuela, *Phys. Rev. D* **69**, 104003 (2004), [gr-qc/0401019](#).
- [102] D. Alic, C. Bona, and C. Bona-Casas, *Phys. Rev. D* **79**, 044026 (2009), [arXiv:0811.1691 \[gr-qc\]](#).
- [103] F. Pretorius, *Class. Quantum Grav.* **22**, 425 (2005), [gr-qc/0407110](#).
- [104] D. Garfinkle, *Phys. Rev. D* **65**, 044029 (2002), [gr-qc/0110013](#).
- [105] L. Lindblom, M. A. Scheel, L. E. Kidder, R. Owen, and O. Rinne, *Class. Quantum Grav.* **23**, 447 (2006), [gr-qc/0512093](#).
- [106] B. Szilágyi, D. Pollney, L. Rezzolla, J. Thornburg, and J. Winicour, *Class. Quantum Grav.* **24**, S275 (2007), [gr-qc/0612150](#).
- [107] E. Sorkin and M. W. Choptuik, *General Relativity and Gravitation* **42**, 1239 (2010), [arXiv:0908.2500 \[gr-qc\]](#).
- [108] J. D. Brown, *Phys. Rev. D* **84**, 124012 (2011), [arXiv:1109.1707 \[gr-qc\]](#).
- [109] W. E. East, F. Pretorius, and B. C. Stephens, *Phys. Rev. D* **85**, 124010 (2012), [arXiv:1112.3094 \[gr-qc\]](#).
- [110] R. Haas, C. D. Ott, B. Szilágyi, J. D. Kaplan, J. Lippuner, M. A. Scheel, K. Barkett, C. D. Muhlberger, T. Dietrich, M. D. Duez, F. Foucart, H. P. Pfeiffer, L. E. Kidder, and S. A. Teukolsky, *ArXiv e-prints* (2016), [arXiv:1604.00782 \[gr-qc\]](#).
- [111] J. A. Isenberg, *International Journal of Modern Physics D* **17**, 265 (2008), [arXiv:gr-qc/0702113](#).
- [112] J. R. Wilson and G. J. Mathews, in *Frontiers in Numerical Relativity*, edited by C. R. Evans, L. S. Finn, and D. W. Hobill (1989) pp. 306–314.
- [113] J. M. Martí, J. M. Ibáñez, and J. A. Miralles, *Phys. Rev. D* **43**, 3794 (1991).
- [114] F. Banyuls, J. A. Font, J. M. Ibáñez, J. M. Martí, and J. A. Miralles, *Astrophys. J.* **476**, 221 (1997).
- [115] J. Ibáñez, M. Aloy, J. Font, J. Martí, J. Miralles, and J. Pons, in *Godunov methods: theory and applications*, edited by E. Toro (Kluwer Academic/Plenum Publishers, New York, 2001).
- [116] J. A. Font, *Living Rev. Relativ.* **6**, 4 (2003).
- [117] D. Radice, L. Rezzolla, and F. Galeazzi, *Class. Quantum Grav.* **31**, 075012 (2014), [arXiv:1312.5004 \[gr-qc\]](#).
- [118] C. Palenzuela, L. Lehner, O. Reula, and L. Rezzolla, *Mon. Not. R. Astron. Soc.* **394**, 1727 (2009), [arXiv:0810.1838](#).
- [119] K. Dionysopoulou, D. Alic, C. Palenzuela, L. Rezzolla, and B. Giacomazzo, *Phys. Rev. D* **88**, 044020 (2013), [arXiv:1208.3487 \[gr-qc\]](#).
- [120] C. Palenzuela, *Mon. Not. R. Astron. Soc.* **431**, 1853 (2013), [arXiv:1212.0130 \[astro-ph.HE\]](#).
- [121] L. Antón, O. Zanotti, J. A. Miralles, J. M. Martí, J. M. Ibáñez, J. A. Font, and J. A. Pons, *Astrophys. J.* **637**, 296 (2006), [astro-ph/0506063](#).
- [122] B. Giacomazzo and L. Rezzolla, *Class. Quantum Grav.* **24**, 235 (2007), [gr-qc/0701109](#).
- [123] M. D. Duez, Y. T. Liu, S. L. Shapiro, and B. C. Stephens, *Phys. Rev. D* **72**, 024028 (2005), [astro-ph/0503420](#).
- [124] L. Pareschi and G. Russo, *Journal of Scientific Computing* **25**, 129 (2005).

- [125] J. R. Wilson and G. J. Mathews, *Phys. Rev. Lett.* **75**, 4161 (1995).
- [126] S. Bonazzola, E. Gourgoulhon, and J.-A. Marck, *Phys. Rev. D* **56**, 7740 (1997), [gr-qc/9710031](#).
- [127] P. Marronetti, G. J. Mathews, and J. R. Wilson, *Phys. Rev. D* **58**, 107503 (1998).
- [128] T. W. Baumgarte, G. B. Cook, M. A. Scheel, S. L. Shapiro, and S. A. Teukolsky, *Phys. Rev. Lett.* **79**, 1182 (1997).
- [129] P. Marronetti, G. J. Mathews, and J. R. Wilson, *Phys. Rev. D* **60**, 087301 (1999).
- [130] S. Bonazzola, E. Gourgoulhon, and J. A. Marck, *Phys. Rev. Lett.* **82**, 892 (1999), [gr-qc/9810072](#).
- [131] K. Uryū and Y. Eriguchi, *Phys. Rev. D* **61**, 124023 (2000), [gr-qc/9908059](#).
- [132] K. Uryū, M. Shibata, and Y. Eriguchi, *Phys. Rev. D* **62**, 104015 (2000), [gr-qc/0007042](#).
- [133] F. Usui, K. Uryū, and Y. Eriguchi, *Phys. Rev. D* **61**, 024039 (2000), [gr-qc/9906102](#).
- [134] E. Gourgoulhon, P. Grandclément, K. Taniguchi, J.-A. Marck, and S. Bonazzola, *Phys. Rev. D* **63**, 064029 (2001), [gr-qc/0007028](#).
- [135] K. Taniguchi, E. Gourgoulhon, and S. Bonazzola, *Phys. Rev. D* **64**, 064012 (2001), [gr-qc/0103041](#).
- [136] K. Taniguchi and E. Gourgoulhon, *Phys. Rev. D* **66**, 104019 (2002), [gr-qc/0207098](#).
- [137] K. Taniguchi and E. Gourgoulhon, *Phys. Rev. D* **68**, 124025 (2003), [gr-qc/0309045](#).
- [138] M. Bejger, D. Gondek-Rosińska, E. Gourgoulhon, P. Haensel, K. Taniguchi, and J. L. Zdenek, *Astron. Astrophys.* **431**, 297 (2005).
- [139] A. A. Tsokaros and K. Uryū, *Phys. Rev. D* **75**, 044026 (2007).
- [140] K. Kiuchi, Y. Sekiguchi, M. Shibata, and K. Taniguchi, *Phys. Rev. D* **80**, 064037 (2009), [arXiv:0904.4551 \[gr-qc\]](#).
- [141] K. Taniguchi and M. Shibata, *Astrophys. J., Supp.* **188**, 187 (2010), [arXiv:1005.0958 \[astro-ph.SR\]](#).
- [142] A. Tsokaros and K. Uryū, *Journal of Engineering Mathematics* **82**, 133 (2012).
- [143] A. Tsokaros, K. Uryū, and L. Rezzolla, *Phys. Rev. D* **91**, 104030 (2015), [arXiv:1502.05674 \[gr-qc\]](#).
- [144] LORENE, Langage Objet pour la RELativité Numérique, [www.lorene.obspm.fr](#).
- [145] P. C. Peters and J. Mathews, *Phys. Rev.* **131**, 435 (1963).
- [146] M. Turner, *Astrophys. J.* **216**, 914 (1977).
- [147] M. Turner, *Astrophys. J.* **216**, 610 (1977).
- [148] W. E. East and F. Pretorius, *Astrophys. J.* **760**, L4 (2012), [arXiv:1208.5279 \[astro-ph.HE\]](#).
- [149] R. Gold, S. Bernuzzi, M. Thierfelder, B. Brügmann, and F. Pretorius, *Phys. Rev. D* **86**, 121501 (2012), [arXiv:1109.5128 \[gr-qc\]](#).
- [150] S. Rosswog, T. Piran, and E. Nakar, *Mon. Not. R. Astron. Soc.* **430**, 2585 (2013), [arXiv:1204.6240 \[astro-ph.HE\]](#).
- [151] P. Tsatsin and P. Marronetti, *Phys. Rev. D* **88**, 064060 (2013).
- [152] M. Miller, P. Gressman, and W.-M. Suen, *Phys. Rev. D* **69**, 064026 (2004), [gr-qc/0312030](#).
- [153] M. Miller, *Phys. Rev. D* **69**, 124013 (2004), [gr-qc/0305024](#).
- [154] L. Baiotti, T. Damour, B. Giacomazzo, A. Nagar, and L. Rezzolla, *Phys. Rev. D* **84**, 024017 (2011), [arXiv:1103.3874 \[gr-qc\]](#).
- [155] S. Bernuzzi, A. Nagar, M. Thierfelder, and B. Brügmann, *Phys. Rev. D* **86**, 044030 (2012), [arXiv:1205.3403 \[gr-qc\]](#).
- [156] K. Hotokezaka, K. Kyutoku, and M. Shibata, *Phys. Rev. D* **87**, 044001 (2013), [arXiv:1301.3555 \[gr-qc\]](#).
- [157] P. Ajith *et al.*, *Class. Quantum Grav.* **24**, S689 (2007), [arXiv:0704.3764](#).
- [158] P. Ajith, S. Babak, Y. Chen, M. Hewitson, B. Krishnan, J. T. Whelan, B. Brügmann, J. Gonzalez, M. Hannam, S. Husa, M. Koppitz, D. Pollney, L. Rezzolla, L. Santamaría, A. M. Sintes, U. Sperhake, and J. Thornburg, *Phys. Rev. D* **77**, 104017 (2008), [arXiv:0710.2335](#).
- [159] S. Bernuzzi, A. Nagar, T. Dietrich, and T. Damour, *Phys. Rev. Lett.* **114**, 161103 (2015), [arXiv:1412.4553 \[gr-qc\]](#).
- [160] J. S. Read, L. Baiotti, J. D. E. Creighton, J. L. Friedman, B. Giacomazzo, K. Kyutoku, C. Markakis, L. Rezzolla, M. Shibata, and K. Taniguchi, *Phys. Rev. D* **88**, 044042 (2013), [arXiv:1306.4065 \[gr-qc\]](#).
- [161] M. Favata, *Phys. Rev. Lett.* **112**, 101101 (2014), [arXiv:1310.8288 \[gr-qc\]](#).
- [162] K. Yagi, K. Kyutoku, G. Pappas, N. Yunes, and T. A. Apostolatos, *Phys. Rev. D* **89**, 124013 (2014), [arXiv:1403.6243 \[gr-qc\]](#).
- [163] L. Wade, J. D. E. Creighton, E. Ochsner, B. D. Lackey, B. F. Farr, T. B. Littenberg, and V. Raymond, *Phys. Rev. D* **89**, 103012 (2014), [arXiv:1402.5156 \[gr-qc\]](#).
- [164] K. Uryū, F. Limousin, J. L. Friedman, E. Gourgoulhon, and M. Shibata, *Phys. Rev. Lett.* **97**, 171101

- (2006), [gr-qc/0511136](#).
- [165] K. Uryū, F. Limousin, J. L. Friedman, E.ourgoulhon, and M. Shibata, *Phys. Rev. D* **80**, 124004 (2009), [arXiv:0908.0579 \[gr-qc\]](#).
- [166] J. A. Isenberg, *The Construction of Spacetimes from Initial Data*, Ph.D. thesis, University of Maryland (1979).
- [167] K. Uryū and A. Tsokaros, *Phys. Rev. D* **85**, 064014 (2012), [arXiv:1108.3065 \[gr-qc\]](#).
- [168] T. W. Baumgarte, G. B. Cook, M. A. Scheel, S. L. Shapiro, and S. A. Teukolsky, *Phys. Rev. D* **57**, 7299 (1998), [gr-qc/9709026](#).
- [169] L. Bildsten and C. Cutler, *Astrophys. J.* **400**, 175 (1992).
- [170] H. Asada, *Phys. Rev. D* **57**, 7292 (1998), [gr-qc/9804003](#).
- [171] S. A. Teukolsky, *Astrophys. J.* **504**, 442 (1998), [gr-qc/9803082](#).
- [172] M. Shibata, *Phys. Rev. D* **58**, 024012 (1998), [gr-qc/9803085](#).
- [173] K. Kyutoku, M. Shibata, and K. Taniguchi, *Phys. Rev. D* **90**, 064006 (2014), [arXiv:1405.6207 \[gr-qc\]](#).
- [174] H. P. Pfeiffer *et al.*, *Class. Quantum Grav.* **24**, S59 (2007), [arXiv:gr-qc/0702106](#).
- [175] I. Hinder and *et al.*, *Class. Quantum Grav.* **31**, 025012 (2013), [arXiv:1307.5307 \[gr-qc\]](#).
- [176] N. Moldenhauer, C. M. Markakis, N. K. Johnson-McDaniel, W. Tichy, and B. Brügmann, *Phys. Rev. D* **90**, 084043 (2014), [arXiv:1408.4136 \[gr-qc\]](#).
- [177] S. Osłowski, T. Bulik, D. Gondek-Rosińska, and K. Belczyński, *Mon. Not. R. Astron. Soc.* **413**, 461 (2011), [arXiv:0903.3538 \[astro-ph.GA\]](#).
- [178] P. D. Kiel, J. R. Hurley, and M. Bailes, *Mon. Not. R. Astron. Soc.* **406**, 656 (2010), [arXiv:1004.0131 \[astro-ph.GA\]](#).
- [179] W. Tichy, *Phys. Rev. D* **84**, 024041 (2011), [arXiv:1107.1440 \[gr-qc\]](#).
- [180] P. Marronetti and S. L. Shapiro, *Phys. Rev. D* **68**, 104024 (2003), [gr-qc/0306075](#).
- [181] T. W. Baumgarte and S. L. Shapiro, *Phys. Rev. D* **80**, 064009 (2009), [arXiv:0909.0952 \[gr-qc\]](#).
- [182] W. Tichy, *Phys. Rev. D* **86**, 064024 (2012), [arXiv:1209.5336 \[gr-qc\]](#).
- [183] W. E. East, F. M. Ramazanoğlu, and F. Pretorius, *Phys. Rev. D* **86**, 104053 (2012), [arXiv:1208.3473 \[gr-qc\]](#).
- [184] W. Kastaun, F. Galeazzi, D. Alic, L. Rezzolla, and J. A. Font, *Phys. Rev. D* **88**, 021501 (2013), [arXiv:1301.7348 \[gr-qc\]](#).
- [185] N. Tacik, F. Foucart, H. P. Pfeiffer, R. Haas, S. Ossokine, J. Kaplan, C. Muhlberger, M. D. Duez, L. E. Kidder, M. A. Scheel, and B. Szilágyi, *Phys. Rev. D* **92**, 124012 (2015), [arXiv:1508.06986 \[gr-qc\]](#).
- [186] H. P. Pfeiffer, L. E. Kidder, M. A. Scheel, and S. A. Teukolsky, *Comput. Phys. Commun.* **152**, 253 (2003), [gr-qc/0202096](#).
- [187] F. Foucart, L. E. Kidder, H. P. Pfeiffer, and S. A. Teukolsky, *Phys. Rev. D* **77**, 124051 (2008), [arXiv:0804.3787 \[gr-qc\]](#).
- [188] F. Foucart, M. D. Duez, L. E. Kidder, M. A. Scheel, B. Szilágyi, and S. A. Teukolsky, *Phys. Rev. D* **85**, 044015 (2012), [arXiv:1111.1677 \[gr-qc\]](#).
- [189] M. Boyle, D. A. Barrow, L. E. Kidder, A. H. Mroué, H. P. Pfeiffer, M. A. Scheel, G. B. Cook, and S. A. Teukolsky, *Phys. Rev. D* **76**, 124038 (2007), [arXiv:0710.0158 \[gr-qc\]](#).
- [190] A. Buonanno, L. E. Kidder, A. H. Mroué, H. P. Pfeiffer, and A. Taracchini, *Phys. Rev. D* **83**, 104034 (2011), [arXiv:1012.1549 \[gr-qc\]](#).
- [191] K. Taniguchi, M. Shibata, and A. Buonanno, *Phys. Rev. D* **91**, 024033 (2015), [arXiv:1410.0738 \[gr-qc\]](#).
- [192] A. Tsokaros, B. C. Mundim, F. Galeazzi, L. Rezzolla, and K. Uryū, [arXiv:1605.07205](#) (2016), [arXiv:1605.07205 \[gr-qc\]](#).
- [193] D. Radice, L. Rezzolla, and F. Galeazzi, *Mon. Not. R. Astron. Soc. L.* **437**, L46 (2014), [arXiv:1306.6052 \[gr-qc\]](#).
- [194] D. Radice, L. Rezzolla, and F. Galeazzi, *Numerical Modeling of Space Plasma Flows ASTRONUM-2014*, Astronomical Society of the Pacific Conference Series, **498**, 121 (2015), [arXiv:1502.00551 \[gr-qc\]](#).
- [195] T. Nakamura and K. Oohara, in *Numerical Astrophysics 1998 (NAP98) – Proceedings* (1998) [gr-qc/9812054](#).
- [196] K.-i. Oohara and T. Nakamura, *Black holes and gravitational waves: New eyes in the 21st century. Proceedings, 9th Yukawa International Seminar, Kyoto, Japan, June 28-July 2, 1999*, *Prog. Theor. Phys. Suppl.* **136**, 270 (1999), [arXiv:astro-ph/9912085 \[astro-ph\]](#).
- [197] M. Shibata, *Phys. Rev. D* **60**, 104052 (1999), [gr-qc/9908027](#).

- [198] M. Shibata and K. Uryū, *Progress of Theoretical Physics* **107**, 265 (2002), [gr-qc/0203037](#).
- [199] M. Shibata, K. Taniguchi, and K. Uryū, *Phys. Rev. D* **68**, 084020 (2003), [gr-qc/0310030](#).
- [200] N. Stergioulas, T. A. Apostolatos, and J. A. Font, *Mon. Not. R. Astron. Soc.* **352**, 1089 (2004), [arXiv:astro-ph/0312648](#).
- [201] H. Nagakura, K. Hotokezaka, Y. Sekiguchi, M. Shibata, and K. Ioka, *Astrophys. J.* **784**, L28 (2014), [arXiv:1403.0956 \[astro-ph.HE\]](#).
- [202] S. Chandrasekhar, *Hydrodynamic and hydromagnetic stability*, Chandrasekhar81 (Dover Edition, New York, USA, 1981).
- [203] G. Bodo, S. Massaglia, A. Ferrari, and E. Trussoni, *Astron. Astrophys.* **283**, 655 (1994).
- [204] D. J. Price and S. Rosswog, *Science* **312**, 719 (2006), [astro-ph/0603845](#).
- [205] B. Giacomazzo, L. Rezzolla, and L. Baiotti, *Phys. Rev. D* **83**, 044014 (2011), [arXiv:1009.2468 \[gr-qc\]](#).
- [206] D. W. Neilsen, S. L. Liebling, M. Anderson, L. Lehner, E. O'Connor, and C. Palenzuela, *Phys. Rev. D* **89**, 104029 (2014), [arXiv:1403.3680 \[gr-qc\]](#).
- [207] T. Rembiasz, J. Guilet, M. Obergaulinger, P. Cerdá-Durán, M. A. Aloy, and E. Müller, *Mon. Not. R. Astron. Soc.* **460**, 3316 (2016), [arXiv:1603.00466 \[astro-ph.SR\]](#).
- [208] N. Stergioulas, A. Bauswein, K. Zagkouris, and H.-T. Janka, *Mon. Not. R. Astron. Soc.* **418**, 427 (2011), [arXiv:1105.0368 \[gr-qc\]](#).
- [209] D. D. Doneva, K. D. Kokkotas, and P. Pnigouras, *Phys. Rev. D* **92**, 104040 (2015), [arXiv:1510.00673 \[gr-qc\]](#).
- [210] D. Shoemaker, *Advanced LIGO anticipated sensitivity curves*, Technical notes LIGO-T0900288-v2 (LIGO, 2009) note: the high-power detuned model used in this paper is given in the data file ZERO_DET_high_P.txt.
- [211] M. Punturo *et al.*, *Class. Quantum Grav.* **27**, 084007 (2010).
- [212] L. Santamaría, F. Ohme, P. Ajith, B. Brügmann, N. Dorband, M. Hannam, S. Husa, P. Mösta, D. Pollney, C. Reisswig, E. L. Robinson, J. Seiler, and B. Krishnan, *Phys. Rev. D* **82**, 064016 (2010), [arXiv:1005.3306 \[gr-qc\]](#).
- [213] C. Cutler and É. E. Flanagan, *Phys. Rev. D* **49**, 2658 (1994), [gr-qc/9402014](#).
- [214] W. Del Pozzo, T. G. F. Li, M. Agathos, C. Van Den Broeck, and S. Vitale, *Phys. Rev. Lett.* **111**, 071101 (2013), [arXiv:1307.8338 \[gr-qc\]](#).
- [215] B. D. Lackey and L. Wade, *Phys. Rev. D* **91**, 043002 (2015), [arXiv:1410.8866 \[gr-qc\]](#).
- [216] M. Agathos, J. Meidam, W. Del Pozzo, T. G. F. Li, M. Tompitak, J. Veitch, S. Vitale, and C. Van Den Broeck, *Phys. Rev. D* **92**, 023012 (2015), [arXiv:1503.05405 \[gr-qc\]](#).
- [217] J. S. Read, B. D. Lackey, B. J. Owen, and J. L. Friedman, *Phys. Rev. D* **79**, 124032 (2009), [arXiv:0812.2163](#).
- [218] S. Bernuzzi, A. Nagar, S. Balmelli, T. Dietrich, and M. Ujevic, *Phys. Rev. Lett.* **112**, 201101 (2014), [arXiv:1402.6244 \[gr-qc\]](#).
- [219] K. Takami, L. Rezzolla, and L. Baiotti, *Phys. Rev. D* **91**, 064001 (2015), [arXiv:1412.3240 \[gr-qc\]](#).
- [220] K. Hotokezaka, K. Kyutoku, Y.-i. Sekiguchi, and M. Shibata, [arXiv:1603.01286](#) (2016), [arXiv:1603.01286 \[gr-qc\]](#).
- [221] K. Hotokezaka, K. Kyutoku, H. Okawa, and M. Shibata, *Phys. Rev. D* **91**, 064060 (2015), [arXiv:1502.03457 \[gr-qc\]](#).
- [222] M. Thierfelder, S. Bernuzzi, and B. Brügmann, *Phys. Rev. D* **84**, 044012 (2011), [arXiv:1104.4751 \[gr-qc\]](#).
- [223] A. W. Steiner, M. Hempel, and T. Fischer, *Astrophys. J.* **774**, 17 (2013), [arXiv:1207.2184 \[astro-ph.SR\]](#).
- [224] S. Banik, M. Hempel, and D. Bandyopadhyay, *Astrophys. J. Suppl.* **214**, 22 (2014), [arXiv:1404.6173 \[astro-ph.HE\]](#).
- [225] M. Hempel, T. Fischer, J. Schaffner-Bielich, and M. Liebendörfer, *Astrophys. J.* **748**, 70 (2012), [arXiv:1108.0848 \[astro-ph.HE\]](#).
- [226] L. Blanchet, *Living Rev. Relativ.* **9**, 4 (2006).
- [227] E. Poisson and C. M. Will, *Gravity, by Eric Poisson, Clifford M. Will, Cambridge, UK: Cambridge University Press, 2014* (2014).
- [228] A. Buonanno and T. Damour, *Phys. Rev. D* **59**, 084006 (1999), [gr-qc/9811091](#).
- [229] A. Buonanno and T. Damour, *Phys. Rev. D* **62**, 064015 (2000), [gr-qc/0001013](#).
- [230] T. Damour, P. Jaranowski, and G. Schäfer, *Phys. Rev. D* **62**, 044024 (2000), [gr-qc/9912092](#).

- [231] T. Damour, *Phys. Rev. D* **64**, 124013 (2001), [gr-qc/0103018](#).
- [232] T. Hinderer, *Astrophys. J.* **677**, 1216 (2008), [arXiv:0711.2420](#).
- [233] T. Damour and A. Nagar, *Phys. Rev. D* **80**, 084035 (2009), [arXiv:0906.0096 \[gr-qc\]](#).
- [234] T. Binnington and E. Poisson, *Phys. Rev. D* **80**, 084018 (2009), [arXiv:0906.1366 \[gr-qc\]](#).
- [235] T. Hinderer, B. D. Lackey, R. N. Lang, and J. S. Read, *Phys. Rev. D* **81**, 123016 (2010), [arXiv:0911.3535 \[astro-ph.HE\]](#).
- [236] T. Damour, A. Nagar, and L. Villain, *Phys. Rev. D* **85**, 123007 (2012).
- [237] T. Damour and A. Nagar, *Phys. Rev. D* **81**, 084016 (2010), [arXiv:0911.5041 \[gr-qc\]](#).
- [238] D. Bini and T. Damour, *Phys. Rev. D* **90**, 124037 (2014), [arXiv:1409.6933 \[gr-qc\]](#).
- [239] D. Bini and T. Damour, *Phys. Rev. D* **89**, 064063 (2014), [arXiv:1312.2503 \[gr-qc\]](#).
- [240] S. R. Dolan, P. Nolan, A. C. Ottewill, N. Warburton, and B. Wardell, *Phys. Rev. D* **91**, 023009 (2015), [arXiv:1406.4890 \[gr-qc\]](#).
- [241] L. Baiotti, T. Damour, B. Giacomazzo, A. Nagar, and L. Rezzolla, *Phys. Rev. Lett.* **105**, 261101 (2010), [arXiv:1009.0521 \[gr-qc\]](#).
- [242] T. Hinderer, A. Taracchini, F. Foucart, A. Buonanno, J. Steinhoff, M. Duez, L. E. Kidder, H. P. Pfeiffer, M. A. Scheel, B. Szilágyi, K. Hotokezaka, K. Kyutoku, M. Shibata, and C. W. Carpenter, [arXiv:1602.00599 \(2016\)](#), [arXiv:1602.00599 \[gr-qc\]](#).
- [243] C. Messenger and J. Read, *Phys. Rev. Lett.* **108**, 091101 (2012), [arXiv:1107.5725 \[gr-qc\]](#).
- [244] C. Messenger, K. Takami, S. Gossan, L. Rezzolla, and B. S. Sathyaprakash, *Phys. Rev. X* **4**, 041004 (2014).
- [245] J. S. Read, C. Markakis, M. Shibata, K. Uryū, J. D. E. Creighton, and J. L. Friedman, *Phys. Rev. D* **79**, 124033 (2009), [arXiv:0901.3258 \[gr-qc\]](#).
- [246] K. Barkett, M. A. Scheel, R. Haas, C. D. Ott, S. Bernuzzi, D. A. Brown, B. Szilágyi, J. D. Kaplan, J. Lippuner, C. D. Muhlberger, F. Foucart, and M. D. Duez, *Phys. Rev. D* **93**, 044064 (2016), [arXiv:1509.05782 \[gr-qc\]](#).
- [247] M. Campanelli, C. O. Lousto, and Y. Zlochower, *Phys. Rev. D* **74**, 041501 (2006), [gr-qc/0604012](#).
- [248] D. Pollney, C. Reisswig, L. Rezzolla, B. Szilágyi, M. Ansorg, B. Deris, P. Diener, E. N. Dorband, M. Koppitz, A. Nagar, and E. Schnetter, *Phys. Rev. D* **76**, 124002 (2007), [arXiv:0707.2559 \[gr-qc\]](#).
- [249] M. Hannam, S. Husa, B. Bruegmann, and A. Gopakumar, *Phys. Rev. D* **78**, 104007 (2008), [arXiv:0712.3787 \[gr-qc\]](#).
- [250] S. Bernuzzi, T. Dietrich, W. Tichy, and B. Brügmann, *Phys. Rev. D* **89**, 104021 (2014), [arXiv:1311.4443 \[gr-qc\]](#).
- [251] S. Bernuzzi, D. Radice, C. D. Ott, L. F. Roberts, P. Moesta, and F. Galeazzi, [arXiv:1512.06397 \(2015\)](#), [arXiv:1512.06397 \[gr-qc\]](#).
- [252] M. Shibata, K. Taniguchi, and K. Uryū, *Phys. Rev. D* **71**, 084021 (2005), [gr-qc/0503119](#).
- [253] M. Shibata and K. Taniguchi, *Phys. Rev. D* **73**, 064027 (2006), [astro-ph/0603145](#).
- [254] T. Yamamoto, M. Shibata, and K. Taniguchi, *Phys. Rev. D* **78**, 064054 (2008), [arXiv:0806.4007 \[gr-qc\]](#).
- [255] J. D. Kaplan, C. D. Ott, E. P. O'Connor, K. Kiuchi, L. Roberts, and M. Duez, *Astrophys. J.* **790**, 19 (2014), [arXiv:1306.4034 \[astro-ph.HE\]](#).
- [256] J. M. Centrella, K. C. B. New, L. L. Lowe, and J. D. Brown, *Astrophys. J.* **550**, L193 (2001), [astro-ph/0010574](#).
- [257] A. L. Watts, N. Andersson, and D. I. Jones, *Astrophys. J.* **618**, L37 (2005), [astro-ph/0309554](#).
- [258] T. Dietrich, N. Moldenhauer, N. K. Johnson-McDaniel, S. Bernuzzi, C. M. Markakis, B. Brügmann, and W. Tichy, *Phys. Rev. D* **92**, 124007 (2015), [arXiv:1507.07100 \[gr-qc\]](#).
- [259] D. Radice, S. Bernuzzi, and C. D. Ott, [arXiv:1603.05726 \(2016\)](#), [arXiv:1603.05726 \[gr-qc\]](#).
- [260] K. D. Camarda, P. Anninos, P. C. Fragile, and J. A. Font, *Astrophys. J.* **707**, 1610 (2009), [arXiv:0911.0670 \[astro-ph.SR\]](#).
- [261] L. Franci, R. De Pietri, K. Dionysopoulou, and L. Rezzolla, *Phys. Rev. D* **88**, 104028 (2013), [arXiv:1308.3989 \[gr-qc\]](#).
- [262] C. D. Muhlberger, F. H. Nouri, M. D. Duez, F. Foucart, L. E. Kidder, C. D. Ott, M. A. Scheel, B. Szilágyi, and S. A. Teukolsky, *Phys. Rev. D* **90**, 104014 (2014), [arXiv:1405.2144 \[astro-ph.HE\]](#).
- [263] M. Saijo, T. W. Baumgarte, and S. L. Shapiro, *Astrophys. J.* **595**, 352 (2003), [astro-ph/0302436](#).
- [264] E. Balbinski, *Mon. Not. R. Astron. Soc.* **216**, 897 (1985).
- [265] P. J. Luyten, *Mon. Not. R. Astron. Soc.* **242**, 447 (1990).

- [266] A. Bauswein, N. Stergioulas, and H.-T. Janka, *Phys. Rev. D* **90**, 023002 (2014), arXiv:1403.5301 [astro-ph.SR].
- [267] K. Takami, L. Rezzolla, and L. Baiotti, *Phys. Rev. Lett.* **113**, 091104 (2014), arXiv:1403.5672 [gr-qc].
- [268] S. Bernuzzi, T. Dietrich, and A. Nagar, *Phys. Rev. Lett.* **115**, 091101 (2015), arXiv:1504.01764 [gr-qc].
- [269] F. Maione, R. De Pietri, A. Feo, and F. Löffler, arXiv:1605.03424 (2016), arXiv:1605.03424 [gr-qc].
- [270] N. Andersson, V. Ferrari, D. I. Jones, K. D. Kokkotas, B. Krishnan, J. S. Read, L. Rezzolla, and B. Zink, *General Relativity and Gravitation* **43**, 409 (2011), arXiv:0912.0384 [astro-ph.SR].
- [271] A. Akmal, V. R. Pandharipande, and D. G. Ravenhall, *Phys. Rev. C* **58**, 1804 (1998), arXiv:hep-ph/9804388.
- [272] G. Taranto, M. Baldo, and G. F. Burgio, *Phys. Rev. C* **87**, 045803 (2013), arXiv:1302.6882 [nucl-th].
- [273] K. Hotokezaka, K. Kyutoku, H. Okawa, M. Shibata, and K. Kiuchi, *Phys. Rev. D* **83**, 124008 (2011), arXiv:1105.4370 [astro-ph.HE].
- [274] E. Witten, *Phys. Rev. D* **30**, 272 (1984).
- [275] P. Haensel, J. L. Zdunik, and R. Schaefer, *Astron. Astrophys.* **160**, 121 (1986).
- [276] C. Alcock, E. Farhi, and A. Olinto, *Astrophys. J.* **310**, 261 (1986).
- [277] M. Alford, M. Braby, M. Paris, and S. Reddy, *Astrophys. J.* **629**, 969 (2005), nucl-th/0411016.
- [278] J. Rikowska-Stone, P. A. Guichon, H. H. Matevosyan, and A. W. Thomas, *Nucl.Phys. A* **792**, 341 (2007), arXiv:nucl-th/0611030 [nucl-th].
- [279] S. Weissenborn, I. Sagert, G. Pagliara, M. Hempel, and J. Schaffner-Bielich, *Astrophys.J.* **740**, L14 (2011), arXiv:1102.2869 [astro-ph.HE].
- [280] B. Bhowmick, M. Bhattacharya, A. Bhattacharyya, and G. Gangopadhyay, *Phys.Rev.* **C89**, 065806 (2014), arXiv:1403.0341 [nucl-th].
- [281] A. Bauswein, H.-T. Janka, R. Oechslin, G. Pagliara, I. Sagert, J. Schaffner-Bielich, M. M. Hohle, and R. Neuhäuser, *Phys. Rev. Lett.* **103**, 011101 (2009), arXiv:0812.4248.
- [282] A. Bauswein, R. Oechslin, and H.-T. Janka, *Phys. Rev. D* **81**, 024012 (2010), arXiv:0910.5169 [astro-ph.SR].
- [283] E. Farhi and R. L. Jaffe, *Phys. Rev. D* **30**, 2379 (1984).
- [284] Y. Sekiguchi, K. Kiuchi, K. Kyutoku, and M. Shibata, *Phys. Rev. Lett.* **107**, 211101 (2011), arXiv:1110.4442 [astro-ph.HE].
- [285] K. Kiuchi, Y. Sekiguchi, K. Kyutoku, and M. Shibata, *Class. Quantum Grav.* **29**, 124003 (2012), arXiv:1206.0509 [astro-ph.HE].
- [286] Y. Sekiguchi, K. Kiuchi, K. Kyutoku, and M. Shibata, *Progress of Theoretical and Experimental Physics* **2012**, 01A304 (2012), arXiv:1206.5927 [astro-ph.HE].
- [287] K. Kiuchi, Y. Sekiguchi, K. Kyutoku, and M. Shibata, in *Numerical Modeling of Space Plasma Slows (ASTRONUM 2011)*, Astronomical Society of the Pacific Conference Series, Vol. 459, edited by N. V. Pogorelov, J. A. Font, E. Audit, and G. P. Zank (2012) p. 85.
- [288] É. É. Flanagan and T. Hinderer, *Phys. Rev. D* **77**, 021502 (2008), arXiv:0709.1915.
- [289] K. Hotokezaka, K. Kiuchi, K. Kyutoku, T. Muranushi, Y.-i. Sekiguchi, M. Shibata, and K. Taniguchi, *Phys. Rev. D* **88**, 044026 (2013), arXiv:1307.5888 [astro-ph.HE].
- [290] Advanced LIGO anticipated sensitivity curves, LIGO Document No. T0900288-v3.
- [291] M. Punturo *et al.*, *Class. Quantum Grav.* **27**, 194002 (2010).
- [292] B. S. Sathyaprakash and B. F. Schutz, *Living Rev. Relativ.* **12**, 2 (2009), arXiv:0903.0338 [gr-qc].
- [293] K. Kokkotas and B. Schmidt, *Living Rev. Relativity* **2**, 2 (1999), gr-qc/9909058.
- [294] R. Oechslin and H.-T. Janka, *Phys. Rev. Lett.* **99**, 121102 (2007), astro-ph/0702228.
- [295] A. Bauswein and H.-T. Janka, *Phys. Rev. Lett.* **108**, 011101 (2012), arXiv:1106.1616 [astro-ph.SR].
- [296] A. Bauswein, H.-T. Janka, K. Hebeler, and A. Schwenk, *Phys. Rev. D* **86**, 063001 (2012), arXiv:1204.1888 [astro-ph.SR].
- [297] J. Clark, A. Bauswein, L. Cadonati, H.-T. Janka, C. Pankow, and N. Stergioulas, *Phys. Rev. D* **90**, 062004 (2014), arXiv:1406.5444 [astro-ph.HE].
- [298] A. Bauswein and N. Stergioulas, *Phys. Rev. D* **91**, 124056 (2015), arXiv:1502.03176 [astro-ph.SR].
- [299] T. Dietrich, S. Bernuzzi, M. Ujevic, and B. Brügmann, *Phys. Rev. D* **91**, 124041 (2015), arXiv:1504.01266 [gr-qc].
- [300] F. Foucart, R. Haas, M. D. Duez, E. O'Connor, C. D. Ott, L. Roberts, L. E. Kidder, J. Lippuner, H. P. Pfeiffer, and M. A. Scheel, *Phys. Rev. D* **93**, 044019 (2016), arXiv:1510.06398 [astro-ph.HE].

- [301] R. De Pietri, A. Feo, F. Maione, and F. Löffler, *Phys. Rev. D* **93**, 064047 (2016), arXiv:1509.08804 [gr-qc].
- [302] A. Bauswein, N. Stergioulas, and H.-T. Janka, *European Physical Journal A* **52**, 56 (2016), arXiv:1508.05493 [astro-ph.HE].
- [303] L. Rezzolla and K. Takami, *Phys. Rev. D* **93**, 124051 (2016), arXiv:1604.00246 [gr-qc].
- [304] A. Bauswein, T. W. Baumgarte, and H.-T. Janka, *Phys. Rev. Lett.* **111**, 131101 (2013), arXiv:1307.5191 [astro-ph.SR].
- [305] K. Takami, L. Rezzolla, and L. Baiotti, *Phys. Rev. Lett.* **113**, 091104 (2014), arXiv:1403.5672 [gr-qc].
- [306] A. Endrizzi, R. Ciolfi, B. Giacomazzo, W. Kastaun, and T. Kawamura, arXiv:1604.03445 (2016), arXiv:1604.03445 [astro-ph.HE].
- [307] M. Shibata, K. Taniguchi, H. Okawa, and A. Buonanno, *Phys. Rev. D* **89**, 084005 (2014), arXiv:1310.0627 [gr-qc].
- [308] J. A. Clark, A. Bauswein, N. Stergioulas, and D. Shoemaker, *Class. Quantum Grav.* **33**, 085003 (2016), arXiv:1509.08522 [astro-ph.HE].
- [309] E. Nakar, *Phys. Rep.* **442**, 166 (2007), arXiv:astro-ph/0701748.
- [310] W. H. Lee and E. Ramirez-Ruiz, *New J. Phys.* **9**, 17 (2007), arXiv:astro-ph/0701874.
- [311] J. M. Lattimer, *Annual Review of Nuclear and Particle Science* **62**, 485 (2012).
- [312] S. Rosswog, M. B. Davies, F.-K. Thielemann, and T. Piran, *Astron. Astrophys.* **360**, 171 (2000), astro-ph/0005550.
- [313] R. Oechslin and H.-T. Janka, *Mon. Not. R. Astron. Soc.* **368**, 1489 (2006), astro-ph/0507099.
- [314] K. Kiuchi, Y. Sekiguchi, M. Shibata, and K. Taniguchi, *Phys. Rev. Lett.* **104**, 141101 (2010), arXiv:1002.2689 [astro-ph.HE].
- [315] J. A. Gonzalez, U. Sperhake, B. Bruegmann, M. Hannam, and S. Husa, *Phys. Rev. Lett.* **98**, 091101 (2007), gr-qc/0610154.
- [316] M. Koppitz, D. Pollney, C. Reisswig, L. Rezzolla, J. Thornburg, P. Diener, and E. Schnetter, *Phys. Rev. Lett.* **99**, 041102 (2007), gr-qc/0701163.
- [317] J. Healy, C. O. Lousto, and Y. Zlochower, *Phys. Rev. D* **90**, 104004 (2014), arXiv:1406.7295 [gr-qc].
- [318] R. F. Webbink, in *Dynamics of Star Clusters*, IAU Symposium, Vol. 113, edited by J. Goodman & P. Hut (1985) pp. 541–577.
- [319] B. Giacomazzo, R. Perna, L. Rezzolla, E. Troja, and D. Lazzati, *Astrophys. J.* **762**, L18 (2013), arXiv:1210.8152 [astro-ph.HE].
- [320] L. Lehner, S. L. Liebling, C. Palenzuela, O. L. Caballero, E. O'Connor, M. Anderson, and D. Neilsen, arXiv:1603.00501 (2016), arXiv:1603.00501 [gr-qc].
- [321] Y. Sekiguchi, K. Kiuchi, K. Kyutoku, M. Shibata, and K. Taniguchi, ArXiv e-prints (2016), arXiv:1603.01918 [astro-ph.HE].
- [322] W. E. East, S. T. McWilliams, J. Levin, and F. Pretorius, *Phys. Rev. D* **87**, 043004 (2013), arXiv:1212.0837 [gr-qc].
- [323] A. K. Harding and D. Lai, *Reports on Progress in Physics* **69**, 2631 (2006), astro-ph/0606674.
- [324] K. Kiuchi, P. Cerdá-Durán, K. Kyutoku, Y. Sekiguchi, and M. Shibata, *Phys. Rev. D* **92**, 124034 (2015), arXiv:1509.09205 [astro-ph.HE].
- [325] E. P. Velikhov, *Sov. Phys. JETP* **9**, 995 (1959).
- [326] S. Chandrasekhar, *Proc. Natl. Acad. Sci.* **46**, 253 (1960).
- [327] S. A. Balbus and J. F. Hawley, *Astrophys. J.* **376**, 214 (1991).
- [328] S. A. Balbus and J. F. Hawley, *Rev. Mod. Phys.* **70**, 1 (1998).
- [329] S. S. Komissarov, *Mon. Not. R. Astron. Soc.* **303**, 343 (1999).
- [330] S. Koide, K. Shibata, and T. Kudoh, *Astrophys. J.* **495**, L63 (1998).
- [331] L. Del Zanna, N. Bucciantini, and P. Londrillo, *Astron. Astrophys.* **400**, 397 (2003), arXiv:astro-ph/0210618.
- [332] C. F. Gammie, J. C. McKinney, and G. Tóth, *Astrophys. J.* **589**, 458 (2003), astro-ph/0301509.
- [333] P. Anninos, P. C. Fragile, and J. D. Salmonson, *Astrophys. J.* **635**, 723 (2005).
- [334] L. Del Zanna, O. Zanotti, N. Bucciantini, and P. Londrillo, *Astron. Astrophys.* **473**, 11 (2007), arXiv:0704.3206.
- [335] B. Zink, ArXiv e-prints (2011), arXiv:1102.5202 [gr-qc].
- [336] M. Shibata and Y.-I. Sekiguchi, *Phys. Rev. D* **72**, 044014 (2005), astro-ph/0507383.

- [337] D. W. Neilsen, E. W. Hirschmann, and R. S. Millward, *Class. Quantum Grav.* **23**, S505 (2006).
- [338] B. D. Farris, T. K. Li, Y. T. Liu, and S. L. Shapiro, *Phys. Rev. D* **78**, 024023 (2008), arXiv:0802.3210.
- [339] P. Mösta, B. C. Mundim, J. A. Faber, R. Haas, S. C. Noble, T. Bode, F. Löffler, C. D. Ott, C. Reisswig, and E. Schnetter, *Classical and Quantum Gravity* **31**, 015005 (2014), arXiv:1304.5544 [gr-qc].
- [340] D. Biskamp, *Physics of Fluids* **29**, 1520 (1986).
- [341] S. S. Komissarov, *Mon. Not. R. Astron. Soc.* **382**, 995 (2007), arXiv:0708.0323.
- [342] M. Dumbser and O. Zanotti, *Journal of Computational Physics* **228**, 6991 (2009), arXiv:0903.4832.
- [343] S. Zenitani, M. Hesse, and A. Klimas, *Astrophys. J. Lett.* **716**, L214 (2010), arXiv:1005.4485 [astro-ph.HE].
- [344] M. Takamoto and T. Inoue, *Astrophys. J.* **735**, 113 (2011), arXiv:1105.5683 [astro-ph.HE].
- [345] O. Zanotti and M. Dumbser, *Mon. Not. R. Astron. Soc.* **418**, 1004 (2011), arXiv:1103.5924 [astro-ph.HE].
- [346] N. Bucciantini, B. D. Metzger, T. A. Thompson, and E. Quataert, *Mon. Not. R. Astron. Soc.* **419**, 1537 (2012), arXiv:1106.4668 [astro-ph.HE].
- [347] C. Palenzuela, L. Lehner, S. L. Liebling, M. Ponce, M. Anderson, D. Neilsen, and P. Motl, *Phys. Rev. D* **88**, 043011 (2013), arXiv:1307.7372 [gr-qc].
- [348] M. Ponce, C. Palenzuela, L. Lehner, and S. L. Liebling, *Phys. Rev. D* **90**, 044007 (2014), arXiv:1404.0692 [gr-qc].
- [349] D. Radice and L. Rezzolla, *Astron. Astrophys.* **547**, A26 (2012), arXiv:1206.6502 [astro-ph.IM].
- [350] K. Kiuchi, Y. Sekiguchi, K. Kyutoku, M. Shibata, K. Taniguchi, and T. Wada, arXiv:1506.06811 (2015), arXiv:1506.06811 [astro-ph.HE].
- [351] B. Giacomazzo, J. Zrake, P. C. Duffell, A. I. MacFadyen, and R. Perna, *Astrophys. J.* **809**, 39 (2015), arXiv:1410.0013 [astro-ph.HE].
- [352] C. Palenzuela, S. L. Liebling, D. Neilsen, L. Lehner, O. L. Caballero, E. O'Connor, and M. Anderson, *Phys. Rev. D* **92**, 044045 (2015), arXiv:1505.01607 [gr-qc].
- [353] M. Obergaulinger, M. A. Aloy, and E. Müller, *Astron. Astrophys.* **515**, A30 (2010), arXiv:1003.6031 [astro-ph.SR].
- [354] J. Zrake and A. MacFadyen (2011) pp. 102–105, arXiv:1109.6294.
- [355] J. Zrake and A. I. MacFadyen, *Astrophys. J.* **744**, 32 (2012), arXiv:1108.1991.
- [356] D. Radice and L. Rezzolla, *Astrophys. J.* **766**, L10 (2013), arXiv:1209.2936 [astro-ph.HE].
- [357] C. R. Evans and J. F. Hawley, *Astrophys. J.* **332**, 659 (1988).
- [358] D. S. Balsara and D. S. Spicer, *J. Comput. Phys.* **149**, 270 (1999).
- [359] G. Toth, *J. Comput. Phys.* **161**, 605 (2000).
- [360] D. Balsara, *Astrophysical Journal Suppl. Series* **132**, 83 (2001).
- [361] D. S. Balsara, T. Rumpf, M. Dumbser, and C.-D. Munz, *Journal of Computational Physics* **228**, 2480 (2009), arXiv:0811.2200 [physics.comp-ph].
- [362] A. Dedner, F. Kemm, D. Kröner, C. D. Munz, T. Schnitzer, and M. Wesenberg, *Journal of Computational Physics* **175**, 645 (2002).
- [363] Z. B. Etienne, Y. T. Liu, and S. L. Shapiro, *Phys. Rev. D* **82**, 084031 (2010), arXiv:1007.2848 [astro-ph.HE].
- [364] Z. B. Etienne, V. Paschalidis, Y. T. Liu, and S. L. Shapiro, *Phys. Rev. D* **85**, 024013 (2012), arXiv:1110.4633 [astro-ph.HE].
- [365] B. D. Farris, R. Gold, V. Paschalidis, Z. B. Etienne, and S. L. Shapiro, *Phys. Rev. Lett.* **109**, 221102 (2012), arXiv:1207.3354 [astro-ph.HE].
- [366] B. Giacomazzo, L. Rezzolla, and L. Baiotti, *Mon. Not. R. Astron. Soc.* **399**, L164 (2009), arXiv:0901.2722 [gr-qc].
- [367] K. Kiuchi, K. Kyutoku, and M. Shibata, *Phys. Rev. D* **86**, 064008 (2012), arXiv:1207.6444 [astro-ph.HE].
- [368] K. Kiuchi, K. Kyutoku, K. Hotokezaka, Y. Sekiguchi, and M. Shibata, in *Numerical Modeling of Space Plasma Flows (ASTRONUM2012)*, Astronomical Society of the Pacific Conference Series, Vol. 474, edited by N. V. Pogorelov, E. Audit, and G. P. Zank (2013) p. 84.
- [369] N. K. Glendinning and S. A. Moszkowski, *Phys. Rev. Lett.* **67**, 2414 (1991).
- [370] J. Zrake and A. I. MacFadyen, *Astrophys. J.* **769**, L29 (2013), arXiv:1303.1450 [astro-ph.HE].
- [371] P. Goldreich and D. Lynden-Bell, *Astrophys. J.* **156**, 59 (1969).

- [372] M. Ponce, C. Palenzuela, E. Barausse, and L. Lehner, *Phys. Rev. D* **91**, 084038 (2015), arXiv:1410.0638 [gr-qc].
- [373] M. A. Aloy, L. Rezzolla, B. Giacomazzo, and M. Obergaulinger, in *Numerical Modeling of Space Plasma Slows (ASTRONUM 2011)*, Astronomical Society of the Pacific Conference Series, Vol. 459, edited by N. V. Pogorelov, J. A. Font, E. Audit, and G. P. Zank (2012) p. 49.
- [374] Z. B. Etienne, V. Paschalidis, and S. L. Shapiro, *Phys. Rev. D* **86**, 084026 (2012), arXiv:1209.1632 [astro-ph.HE].
- [375] R. D. Blandford and R. L. Znajek, *Mon. Not. R. Astron. Soc.* **179**, 433 (1977).
- [376] M. A. Aloy and L. Rezzolla, *Astrophys. J.* **640**, L115 (2006).
- [377] D. A. Uzdensky, *Space Science Reviews* **160**, 45 (2011), arXiv:1101.2472 [astro-ph.HE].
- [378] N. Gehrels and et al., *Astrophys. J.* **611**, 1005 (2004).
- [379] A. Rowlinson, P. T. O'Brien, B. D. Metzger, N. R. Tanvir, and A. J. Levan, *Mon. Not. R. Astron. Soc.* **430**, 1061 (2013), arXiv:1301.0629 [astro-ph.HE].
- [380] B. P. Gompertz, P. T. O'Brien, and G. A. Wynn, *Mon. Not. R. Astron. Soc.* **438**, 240 (2014), arXiv:1311.1505 [astro-ph.HE].
- [381] K. Hotokezaka, K. Kiuchi, K. Kyutoku, H. Okawa, Y.-i. Sekiguchi, M. Shibata, and K. Taniguchi, *Phys. Rev. D* **87**, 024001 (2013), arXiv:1212.0905 [astro-ph.HE].
- [382] B. Zhang and P. Mészáros, *Astrophys. J.* **552**, L35 (2001), astro-ph/0011133.
- [383] W.-H. Gao and Y.-Z. Fan, *Chinese Journal of Astronomy and Astrophysics* **6**, 513 (2006), astro-ph/0512646.
- [384] Y.-Z. Fan and D. Xu, *Mon. Not. R. Astron. Soc.* **372**, L19 (2006), astro-ph/0605445.
- [385] B. D. Metzger, E. Quataert, and T. A. Thompson, *Mon. Not. R. Astron. Soc.* **385**, 1455 (2008), arXiv:0712.1233.
- [386] B. D. Metzger, D. Giannios, T. A. Thompson, N. Bucciantini, and E. Quataert, *Mon. Not. R. Astron. Soc.* **413**, 2031 (2011), arXiv:1012.0001 [astro-ph.HE].
- [387] B. Giacomazzo and R. Perna, *Astrophys. J.* **771**, L26 (2013), arXiv:1306.1608 [astro-ph.HE].
- [388] S. Dall'Osso, B. Giacomazzo, R. Perna, and L. Stella, *Astrophys. J.* **798**, 25 (2015), arXiv:1408.0013 [astro-ph.HE].
- [389] R. Ciolfi, V. Ferrari, and L. Gualtieri, *Mon. Not. R. Astron. Soc.* **406**, 2540 (2010), arXiv:1003.2148 [astro-ph.SR].
- [390] J. Friebe and L. Rezzolla, *Mon. Not. R. Astron. Soc.* **427**, 3406 (2012), arXiv:1207.4035 [gr-qc].
- [391] R. Ciolfi and L. Rezzolla, *Mon. Not. R. Astron. Soc.* **435**, L43 (2013), arXiv:1306.2803 [astro-ph.SR].
- [392] B. Giacomazzo, L. Rezzolla, and L. Baiotti, *Phys. Rev. D* **83**, 044014 (2011).
- [393] R. Ciolfi and D. M. Siegel, *Astrophys. J.* **798**, L36 (2015), arXiv:1411.2015 [astro-ph.HE].
- [394] D. M. Siegel, R. Ciolfi, and L. Rezzolla, *Astrophys. J.* **785**, L6 (2014), arXiv:1401.4544 [astro-ph.HE].
- [395] B. D. Metzger and R. Fernández, *Mon. Not. R. Astron. Soc.* **441**, 3444 (2014), arXiv:1402.4803 [astro-ph.HE].
- [396] A. Perego, S. Rosswog, R. M. Cabezón, O. Korobkin, R. Käppeli, A. Arcones, and M. Liebendörfer, *Mon. Not. R. Astron. Soc.* **443**, 3134 (2014), arXiv:1405.6730 [astro-ph.HE].
- [397] M. Ruffert and H.-T. Janka, *Astron. Astrophys.* **344**, 573 (1999), astro-ph/9809280.
- [398] M. A. Aloy, H. Janka, and E. Müller, *Astron. Astrophys.* **436**, 273 (2005), arXiv:astro-ph/0408291.
- [399] A. Murguia-Berthier, G. Montes, E. Ramirez-Ruiz, F. De Colle, and W. H. Lee, *Astrophys. J.* **788**, L8 (2014), arXiv:1404.0383 [astro-ph.HE].
- [400] E. Troja, S. Rosswog, and N. Gehrels, *Astrophys. J.* **723**, 1711 (2010), arXiv:1009.1385 [astro-ph.HE].
- [401] T. Piran, *Reviews of Modern Physics* **76**, 1143 (2005), astro-ph/0405503.
- [402] O. Just, M. Obergaulinger, H.-T. Janka, A. Bauswein, and N. Schwarz, *Astrophys. J. Lett.* **816**, L30 (2016), arXiv:1510.04288 [astro-ph.HE].
- [403] M. Shibata, H. Nagakura, Y. Sekiguchi, and S. Yamada, *Phys. Rev. D* **89**, 084073 (2014).
- [404] E. Abdikamalov, A. Burrows, C. D. Ott, F. Löffler, E. O'Connor, J. C. Dolence, and E. Schnetter, *Astrophys. J.* **755**, 111 (2012), arXiv:1203.2915 [astro-ph.SR].
- [405] K. A. van Riper and J. M. Lattimer, *Astrophys. J.* **249**, 270 (1981).
- [406] M. Ruffert, H.-T. Janka, and G. Schaefer, *Astron. Astrophys.* **311**, 532 (1996), astro-ph/9509006.
- [407] S. Rosswog and M. Liebendörfer, *Mon. Not. R. Astron. Soc.* **342**, 673 (2003), arXiv:astro-ph/0302301.
- [408] E. O'Connor and C. D. Ott, *Class. Quantum Grav.* **27**, 114103 (2010), arXiv:0912.2393 [astro-ph.HE].

- [409] F. Galeazzi, W. Kastaun, L. Rezzolla, and J. A. Font, *Phys. Rev. D* **88**, 064009 (2013), arXiv:1306.4953 [gr-qc].
- [410] K. S. Thorne, *Mon. Not. R. Astron. Soc.* **194**, 439 (1981).
- [411] L. Rezzolla and J. C. Miller, *Class. Quantum Grav.* **11**, 1815 (1994), arXiv:astro-ph/9406055.
- [412] M. Shibata, K. Kiuchi, Y. Sekiguchi, and Y. Suwa, *Progress of Theoretical Physics* **125**, 1255 (2011), arXiv:1104.3937 [astro-ph.HE].
- [413] M. Shibata and Y. Sekiguchi, *Progress of Theoretical Physics* **127**, 535 (2012), arXiv:1206.5911 [astro-ph.HE].
- [414] C. Y. Cardall, E. Endeve, and A. Mezzacappa, *Phys. Rev. D* **88**, 023011 (2013), arXiv:1305.0037 [astro-ph.HE].
- [415] H. R. Takahashi, K. Ohsuga, Y. Sekiguchi, T. Inoue, and K. Tomida, *Astrophys. J.* **764**, 122 (2013), arXiv:1212.4910 [astro-ph.HE].
- [416] K. Hotokezaka, K. Kyutoku, M. Tanaka, K. Kiuchi, Y. Sekiguchi, M. Shibata, and S. Wanajo, *Astrophys. J.* **778**, L16 (2013), arXiv:1310.1623 [astro-ph.HE].
- [417] S. Wanajo, Y. Sekiguchi, N. Nishimura, K. Kiuchi, K. Kyutoku, and M. Shibata, *Astrophys. J.* **789**, L39 (2014), arXiv:1402.7317 [astro-ph.SR].
- [418] Y. Sekiguchi, K. Kiuchi, K. Kyutoku, and M. Shibata, *Phys. Rev. D* **91**, 064059 (2015), arXiv:1502.06660 [astro-ph.HE].
- [419] Y. Sekiguchi, *Progress of Theoretical Physics* **124**, 331 (2010), arXiv:1009.3320 [astro-ph.HE].
- [420] Y. Sekiguchi and M. Shibata, *Astrophys. J.* **737**, 6 (2011), arXiv:1009.5303 [astro-ph.HE].
- [421] F. Foucart, E. O'Connor, L. Roberts, M. D. Duez, R. Haas, L. E. Kidder, C. D. Ott, H. P. Pfeiffer, M. A. Scheel, and B. Szilagyi, *Phys. Rev. D* **91**, 124021 (2015), arXiv:1502.04146 [astro-ph.HE].
- [422] R. G. McClarren and C. D. Hauck, *J. Comput. Phys.* **229**, 5597 (2010).
- [423] A. Mezzacappa and S. W. Bruenn, *Astrophys. J.* **405**, 637 (1993).
- [424] L. Scheck, K. Kifonidis, H.-T. Janka, and E. Müller, *Astron. Astrophys.* **457**, 963 (2006), arXiv:astro-ph/0601302.
- [425] C. D. Ott, A. Burrows, L. Dessart, and E. Livne, *Astrophys. J.* **685**, 1069 (2008), arXiv:0804.0239.
- [426] M. Liebendörfer, S. C. Whitehouse, and T. Fischer, *Astrophys. J.* **698**, 1174 (2009), arXiv:0711.2929.
- [427] K. Sumiyoshi and S. Yamada, *Astrophys. J., Supp.* **199**, 17 (2012), arXiv:1201.2244 [astro-ph.HE].
- [428] M. Ruffert, H.-T. Janka, K. Takahashi, and G. Schaefer, *Astron. Astrophys.* **319**, 122 (1997), astro-ph/9606181.
- [429] M. Ruffert and H.-T. Janka, *Astron. Astrophys.* **380**, 544 (2001), astro-ph/0106229.
- [430] S. Rosswog, E. Ramirez-Ruiz, and M. B. Davies, *Mon. Not. R. Astron. Soc.* **345**, 1077 (2003), arXiv:astro-ph/0110180.
- [431] Y. Sekiguchi, K. Kiuchi, K. Kyutoku, and M. Shibata, *Phys. Rev. Lett.* **107**, 051102 (2011), arXiv:1105.2125 [gr-qc].
- [432] O. Korobkin, S. Rosswog, A. Arcones, and C. Winteler, *Mon. Not. R. Astron. Soc.* **426**, 1940 (2012), arXiv:1206.2379 [astro-ph.SR].
- [433] S. Rosswog, O. Korobkin, A. Arcones, F.-K. Thielemann, and T. Piran, *Mon. Not. R. Astron. Soc.* **439**, 744 (2014), arXiv:1307.2939 [astro-ph.HE].
- [434] R. Oechslin, H.-T. Janka, and A. Marek, *Astron. Astrophys.* **467**, 395 (2007), astro-ph/0611047.
- [435] A. Bauswein, S. Goriely, and H.-T. Janka, *Astrophys. J.* **773**, 78 (2013), arXiv:1302.6530 [astro-ph.SR].
- [436] M. Arnould, S. Goriely, and K. Takahashi, *Physics Reports* **450**, 97 (2007), arXiv:0705.4512.
- [437] S. Rosswog, *Astrophys. J.* **634**, 1202 (2005), astro-ph/0508138.
- [438] L. F. Roberts, D. Kasen, W. H. Lee, and E. Ramirez-Ruiz, *Astrophys. J. Lett.* **736**, L21 (2011), arXiv:1104.5504 [astro-ph.HE].
- [439] S. Rosswog, *Royal Society of London Philosophical Transactions Series A* **371**, 20272 (2013), arXiv:1210.6549 [astro-ph.HE].
- [440] K. Kyutoku, K. Ioka, and M. Shibata, *Mon. Not. R. Astron. Soc.* **437**, L6 (2014), arXiv:1209.5747 [astro-ph.HE].
- [441] L. Dessart, C. D. Ott, A. Burrows, S. Rosswog, and E. Livne, *Astrophys. J.* **690**, 1681 (2009), arXiv:0806.4380.
- [442] O. Just, A. Bauswein, R. A. Pulpillo, S. Goriely, and H.-T. Janka, *Mon. Not. R. Astron. Soc.* **448**, 541 (2015), arXiv:1406.2687 [astro-ph.SR].

- [443] M. Shibata, Y. Suwa, K. Kiuchi, and K. Ioka, *Astrophys. J.* **734**, L36 (2011), arXiv:1105.3302 [astro-ph.HE].
- [444] S. Goriely, A. Bauswein, and H.-T. Janka, *Astrophys. J.* **738**, L32 (2011), arXiv:1107.0899 [astro-ph.SR].
- [445] T. Piran, E. Nakar, and S. Rosswog, *Mon. Not. R. Astron. Soc.* **430**, 2121 (2013), arXiv:1204.6242 [astro-ph.HE].
- [446] D. Grossman, O. Korobkin, S. Rosswog, and T. Piran, *Mon. Not. R. Astron. Soc.* **439**, 757 (2014), arXiv:1307.2943 [astro-ph.HE].
- [447] B. D. Metzger, A. Bauswein, S. Goriely, and D. Kasen, *Mon. Not. R. Astron. Soc.* **446**, 1115 (2015), arXiv:1409.0544 [astro-ph.HE].
- [448] S. Goriely, A. Bauswein, O. Just, E. Pllumbi, and H.-T. Janka, *Mon. Not. R. Astron. Soc.* **452**, 3894 (2015), arXiv:1504.04377 [astro-ph.SR].
- [449] K. Kyutoku, K. Ioka, H. Okawa, M. Shibata, and K. Taniguchi, *Phys. Rev. D* **92**, 044028 (2015), arXiv:1502.05402 [astro-ph.HE].
- [450] M. Tanaka and K. Hotokezaka, *Astrophys. J.* **775**, 113 (2013), arXiv:1306.3742 [astro-ph.HE].
- [451] B. D. Metzger and E. Berger, *Astrophys. J.* **746**, 48 (2012), arXiv:1108.6056 [astro-ph.HE].
- [452] S. Kisaka, K. Ioka, and T. Nakamura, *Astrophys. J. Lett.* **809**, L8 (2015), arXiv:1506.02030 [astro-ph.HE].
- [453] S. Rosswog and D. Price, *Mon. Not. R. Astron. Soc.* **379**, 915 (2007), arXiv:0705.1441.
- [454] K. Hotokezaka, S. Wanajo, M. Tanaka, A. Bamba, Y. Terada, and T. Piran, *Mon. Not. R. Astron. Soc.* **459**, 35 (2016), arXiv:1511.05580 [astro-ph.HE].
- [455] J. Barnes, D. Kasen, M.-R. Wu, and G. Mart'inez-Pinedo, ArXiv e-prints (2016), arXiv:1605.07218 [astro-ph.HE].
- [456] E. Nakar and T. Piran, *Nature* **478**, 82 (2011), arXiv:1102.1020 [astro-ph.HE].
- [457] K. Hotokezaka and T. Piran, *Mon. Not. R. Astron. Soc.* **450**, 1430 (2015), arXiv:1501.01986 [astro-ph.HE].
- [458] J. M. Stone, T. A. Gardiner, P. Teuben, J. F. Hawley, and J. B. Simon, *Astrophys. J.s* **178**, 137 (2008), arXiv:0804.0402.
- [459] C. J. White and J. M. Stone, ArXiv e-prints (2015), arXiv:1511.00943 [astro-ph.HE].
- [460] A. S. Almgren, V. E. Beckner, J. B. Bell, M. S. Day, L. H. Howell, C. C. Joggerst, M. J. Lijewski, A. Nonaka, M. Singer, and M. Zingale, *Astrophys. J.* **715**, 1221 (2010), arXiv:1005.0114 [astro-ph.IM].
- [461] D. C. Collins, H. Xu, M. L. Norman, H. Li, and S. Li, *Astrophys. J.s* **186**, 308 (2010), arXiv:0902.2594 [astro-ph.IM].
- [462] B. Fryxell, K. Olson, P. Ricker, F. X. Timmes, M. Zingale, D. Q. Lamb, P. MacNeice, R. Rosner, J. W. Truran, and H. Tufo, *Astrophys. J.s* **131**, 273 (2000).
- [463] M. Shibata, H. Okawa, and T. Yamamoto, *Phys. Rev. D* **78**, 101501 (2008), arXiv:0810.4735 [gr-qc].
- [464] F. Pannarale, E. Berti, K. Kyutoku, and M. Shibata, *Phys. Rev. D* **88**, 084011 (2013), arXiv:1307.5111 [gr-qc].
- [465] M. Shibata, *Progress of Theoretical Physics* **101**, 1199 (1999), gr-qc/9905058.
- [466] L. Baiotti, I. Hawke, P. J. Montero, F. Löffler, L. Rezzolla, N. Stergioulas, J. A. Font, and E. Seidel, *Phys. Rev. D* **71**, 024035 (2005), gr-qc/0403029.
- [467] C. Palenzuela, M. Anderson, L. Lehner, S. L. Liebling, and D. Neilsen, *Phys. Rev. Lett.* **103**, 081101 (2009), arXiv:0905.1121 [astro-ph.HE].
- [468] H.-J. Yo, T. W. Baumgarte, and S. L. Shapiro, *Phys. Rev. D* **66**, 084026 (2002).
- [469] M. D. Duez, P. Marronetti, S. L. Shapiro, and T. W. Baumgarte, *Phys. Rev. D* **67**, 024004 (2003), gr-qc/0209102.
- [470] J. A. Faber, T. W. Baumgarte, Z. B. Etienne, S. L. Shapiro, and K. Taniguchi, *Phys. Rev. D* **76**, 104021 (2007), arXiv:0708.2436 [gr-qc].
- [471] Z. B. Etienne, V. Paschalidis, R. Haas, P. Mösta, and S. L. Shapiro, *Class. Quantum Grav.* **32**, 175009 (2015), arXiv:1501.07276 [astro-ph.HE].
- [472] F. Löffler, J. Faber, E. Bentivegna, T. Bode, P. Diener, R. Haas, I. Hinder, B. C. Mundim, C. D. Ott, E. Schnetter, G. Allen, M. Campanelli, and P. Laguna, *Class. Quantum Grav.* **29**, 115001 (2012), arXiv:1111.3344 [gr-qc].
- [473] M. Zilhão and F. Löffler, *International Journal of Modern Physics A* **28**, 1340014 (2013),

- arXiv:1305.5299 [gr-qc].
- [474] The Einstein Toolkit Consortium: einstein toolkit.org.
- [475] Whisky, EU Network GR Hydrodynamics Code: www.whiskycode.org.
- [476] B. Brügmann, *International Journal of Modern Physics D* **8**, 85 (1999), gr-qc/9708035.
- [477] B. Brügmann, W. Tichy, and N. Jansen, *Phys. Rev. Lett.* **92**, 211101 (2004), gr-qc/0312112.
- [478] B. Brügmann, J. A. González, M. Hannam, S. Husa, U. Sperhake, and W. Tichy, *Phys. Rev. D* **77**, 024027 (2008), gr-qc/0610128, gr-qc/0610128.
- [479] W. E. East, F. Pretorius, and B. C. Stephens, *Phys. Rev. D* **85**, 124009 (2012), arXiv:1111.3055 [astro-ph.HE].
- [480] W. E. East, V. Paschalidis, and F. Pretorius, *Astrophys. J. Lett.* **807**, L3 (2015), arXiv:1503.07171 [astro-ph.HE].
- [481] M. D. Duez *et al.*, *Phys. Rev. D* **78**, 104015 (2008), arXiv:0809.0002 [gr-qc].
- [482] F. Foucart, M. D. Duez, L. E. Kidder, and S. A. Teukolsky, *Phys. Rev. D* **83**, 024005 (2011), arXiv:1007.4203 [astro-ph.HE].
- [483] F. Foucart, *Phys. Rev. D* **86**, 124007 (2012), arXiv:1207.6304 [astro-ph.HE].
- [484] F. Foucart, M. B. Deaton, M. D. Duez, L. E. Kidder, I. MacDonald, C. D. Ott, H. P. Pfeiffer, M. A. Scheel, B. Szilágyi, and S. A. Teukolsky, *Phys. Rev. D* **87**, 084006 (2013), arXiv:1212.4810 [gr-qc].
- [485] M. A. Scheel, M. Boyle, T. Chu, L. E. Kidder, K. D. Matthews, and H. P. Pfeiffer, *Phys. Rev. D* **79**, 024003 (2009), arXiv:0810.1767 [gr-qc].
- [486] G. Lovelace, M. A. Scheel, and B. Szilágyi, *Phys. Rev. D* **83**, 024010 (2011), arXiv:1010.2777 [gr-qc].
- [487] L. T. Buchman, H. P. Pfeiffer, M. A. Scheel, and B. Szilágyi, *Phys. Rev. D* **86**, 084033 (2012), arXiv:1206.3015 [gr-qc].
- [488] S. Ossokine, L. E. Kidder, and H. P. Pfeiffer, *Phys. Rev. D* **88**, 084031 (2013), arXiv:1304.3067 [gr-qc].
- [489] S. Rosswog, *Journal of Computational Physics* **229**, 8591 (2010), arXiv:0907.4890 [astro-ph.HE].
- [490] R. Oechslin, S. Rosswog, and F.-K. Thielemann, *Phys. Rev. D* **65**, 103005 (2002), gr-qc/0111005.
- [491] A. Bauswein, H. Janka, and R. Oechslin, *Phys. Rev. D* **82**, 084043 (2010), arXiv:1006.3315 [astro-ph.SR].
- [492] L. Baiotti, M. Shibata, and T. Yamamoto, *Phys. Rev. D* **82**, 064015 (2010), arXiv:1007.1754 [gr-qc].
- [493] J. Vines, E. E. Flanagan, and T. Hinderer, *Phys. Rev. D* **83**, 084051 (2011), arXiv:1101.1673 [gr-qc].
- [494] F. Pannarale, L. Rezzolla, F. Ohme, and J. S. Read, *Phys. Rev. D* **84**, 104017 (2011), arXiv:1103.3526 [astro-ph.HE].
- [495] A. Maselli, L. Gualtieri, F. Pannarale, and V. Ferrari, *Phys. Rev. D* **86**, 044032 (2012).
- [496] L. Baiotti, I. Hawke, P. Montero, and L. Rezzolla, in *Computational Astrophysics in Italy: Methods and Tools*, Vol. 1, edited by R. Capuzzo-Dolcetta (MSAIt, Trieste, 2003) p. 210.
- [497] A. Suresh and H. T. Huynh, *Journal of Computational Physics* **136**, 83 (1997).
- [498] McLachlan, a Public BSSN Code.
- [499] C. W. Shu, *Essentially non-oscillatory and weighted essentially non-oscillatory schemes for hyperbolic conservation laws*, Lecture notes ICASE Report 97-65; NASA CR-97-206253 (NASA Langley Research Center, 1997).
- [500] Y. Zlochower, M. Ponce, and C. O. Lousto, *Phys. Rev. D* **86**, 104056 (2012).
- [501] S. Bernuzzi and T. Dietrich, arXiv:1604.07999 (2016), arXiv:1604.07999 [gr-qc].
- [502] B. Cockburn and C. Shu, *Math. Comp.* **52**, 411 (1989).
- [503] B. Cockburn, S. How, and C. Shu, *Math. Comp.* **54**, 545 (1990).
- [504] B. Cockburn, *Journal of Computational Physics* **141**, 199 (1998).
- [505] D. Radice and L. Rezzolla, *Phys. Rev. D* **84**, 024010 (2011), arXiv:1103.2426 [gr-qc].
- [506] M. Bugner, T. Dietrich, S. Bernuzzi, A. Weyhausen, and B. Brügmann, *Phys. Rev. D* **94**, 084004 (2016), arXiv:1508.07147 [gr-qc].
- [507] O. Zanotti and M. Dumbser, *Computer Physics Communications* **188**, 110 (2015), arXiv:1312.7784 [astro-ph.HE].
- [508] O. Zanotti, F. Fambri, and M. Dumbser, *Mon. Not. R. Astron. Soc.* **452**, 3010 (2015), arXiv:1504.07458 [astro-ph.HE].
- [509] F. Galeazzi, *Modelling fluid interfaces in numerical relativistic hydrodynamics*, Master's thesis, Università degli studi di Padova (2008).
- [510] W. Kastaun, *Phys. Rev. D* **74**, 124024 (2006).

- [511] S. T. Millmore and I. Hawke, *Class. Quantum Grav.* **27**, 015007 (2010), arXiv:0909.4217 [gr-qc].
- [512] X. Y. Hu, N. A. Adams, and C.-W. Shu, *Journal of Computational Physics* **242**, 169 (2013), arXiv:1203.1540 [physics.flu-dyn].
- [513] M. J. Berger and P. Colella, *J. Comput. Phys.* **82**, 64 (1989).
- [514] C. Reisswig, R. Haas, C. D. Ott, E. Abdikamalov, P. Mösta, D. Pollney, and E. Schnetter, *Phys. Rev. D* **87**, 064023 (2013), arXiv:1212.1191 [astro-ph.HE].
- [515] N. T. Bishop and L. Rezzolla, *Living Rev. Relativity* (2016).
- [516] N. T. Bishop, R. Gómez, L. Lehner, M. Maharaj, and J. Winicour, *Phys. Rev. D* **56**, 6298 (1997), gr-qc/9708065.
- [517] D. M. Eardley, *Astrophys. J.* **196**, L59 (1975).
- [518] C. M. Will, *Theory and Experiment in Gravitational Physics*, by Clifford M. Will, pp. 396. ISBN 0521439736. Cambridge, UK: Cambridge University Press, March 1993. (1993).
- [519] J. Alsing, E. Berti, C. M. Will, and H. Zanglauer, *Phys. Rev. D* **85**, 064041 (2012), arXiv:1112.4903 [gr-qc].
- [520] S. Mirshekari and C. M. Will, *Phys. Rev. D* **87**, 084070 (2013), arXiv:1301.4680 [gr-qc].
- [521] E. Barausse, C. Palenzuela, M. Ponce, and L. Lehner, *Phys. Rev. D* **87**, 081506 (2013), arXiv:1212.5053 [gr-qc].
- [522] C. Palenzuela, E. Barausse, M. Ponce, and L. Lehner, *Phys. Rev. D* **89**, 044024 (2014), arXiv:1310.4481 [gr-qc].
- [523] L. Sampson, N. Yunes, N. Cornish, M. Ponce, E. Barausse, A. Klein, C. Palenzuela, and L. Lehner, *Phys. Rev. D* **90**, 124091 (2014), arXiv:1407.7038 [gr-qc].
- [524] R. V. Wagoner, *Phys. Rev. D* **1**, 3209 (1970).
- [525] K. Nordtvedt, Jr., *Astrophys. J.* **161**, 1059 (1970).
- [526] T. Damour and G. Esposito-Farese, *Class. Quantum Grav.* **9**, 2093 (1992).
- [527] M. Kramer and N. Wex, *Class. Quantum Grav.* **26**, 073001 (2009).
- [528] P. C. C. Freire, N. Wex, G. Esposito-Farèse, J. P. W. Verbiest, M. Bailes, B. A. Jacoby, M. Kramer, I. H. Stairs, J. Antoniadis, and G. H. Janssen, *Mon. Not. R. Astron. Soc.* **423**, 3328 (2012), arXiv:1205.1450 [astro-ph.GA].
- [529] D. Babusci, L. Baiotti, F. Fucito, and A. Nagar, *Phys. Rev. D* **64**, 062001 (2001), gr-qc/0105028.
- [530] T. Damour and G. Esposito-Farese, *Phys. Rev. Lett.* **70**, 2220 (1993).
- [531] F. M. Ramazanoğlu and F. Pretorius, *Phys. Rev. D* **93**, 064005 (2016), arXiv:1601.07475 [gr-qc].
- [532] N. Sennett and A. Buonanno, *Phys. Rev. D* **93**, 124004 (2016), arXiv:1603.03300 [gr-qc].
- [533] K. Thorne, in *Magic Without Magic: John Archibald Wheeler*, edited by J. Klauder (Freeman, San Francisco, 1972) p. 231.
- [534] D. M. Eardley and S. B. Giddings, *Phys. Rev. D* **66**, 044011 (2002), arXiv:gr-qc/0201034.
- [535] M. W. Choptuik and F. Pretorius, *Phys. Rev. Lett.* **104**, 111101 (2010), arXiv:0908.1780 [gr-qc].
- [536] I. Antoniadis, N. Arkani-Hamed, S. Dimopoulos, and G. Dvali, *Physics Letters B* **436**, 257 (1998), hep-ph/9804398.
- [537] P. C. Argyres, S. Dimopoulos, and J. March-Russell, *Physics Letters B* **441**, 96 (1998), arXiv:hep-th/9808138.
- [538] C.-M. Yoo, H. Ishihara, M. Kimura, and S. Tanzawa, *Phys. Rev. D* **81**, 024020 (2010), arXiv:0906.0689 [gr-qc].
- [539] H. Yoshino and Y. Nambu, *Phys. Rev. D* **67**, 024009 (2003), arXiv:gr-qc/0209003.
- [540] S. Dimopoulos and G. Landsberg, *Phys. Rev. Lett.* **87**, 161602 (2001), arXiv:hep-ph/0106295.
- [541] J. L. Feng and A. D. Shapere, *Phys. Rev. Lett.* **88**, 021303 (2002), hep-ph/0109106.
- [542] S. Chatrchyan, V. Khachatryan, A. M. Sirunyan, A. Tumasyan, W. Adam, T. Bergauer, M. Dragicevic, J. Erö, C. Fabjan, M. Friedl, and et al., *Journal of High Energy Physics* **7**, 178 (2013), arXiv:1303.5338 [hep-ex].
- [543] L. Rezzolla and K. Takami, *Class. Quantum Grav.* **30**, 012001 (2013), arXiv:1209.6138 [gr-qc].
- [544] W. E. East and F. Pretorius, *Phys. Rev. Lett.* **110**, 101101 (2013), arXiv:1210.0443 [gr-qc].
- [545] T. Kellerman, L. Baiotti, B. Giacomazzo, and L. Rezzolla, *Class. Quantum Grav.* **25**, 225007 (2008), arXiv:0811.0938.
- [546] T. Kellerman, L. Rezzolla, and D. Radice, *Class. Quantum Grav.* **27**, 235016 (2010), arXiv:1007.2797 [gr-qc].

- [547] D. Radice, L. Rezzolla, and T. Kellerman, *Class. Quantum Grav.* **27**, 235015 (2010), [arXiv:1007.2809 \[gr-qc\]](#).
- [548] S. C. Noble, *A Numerical Study of Relativistic Fluid Collapse*, *Ph.D. thesis*, University of Texas at Austin (2003), [gr-qc/0310116v1](#).
- [549] S. C. Noble and M. W. Choptuik, *Phys. Rev. D* **78**, 064059 (2008), [arXiv:0709.3527](#).
- [550] S. C. Noble and M. W. Choptuik, *Phys. Rev. D* **93**, 024015 (2016), [arXiv:1512.02999 \[gr-qc\]](#).
- [551] C. Gundlach, *Physics Reports* **376**, 339 (2003), [gr-qc/0210101](#).